SYNTHESIS, STABILITY AND CHARACTERIZATION OF INDIRECT CONVERSION MATERIALS FOR THE MEASUREMENT OF DOSE AT A SYNCHROTRON BIOMEDICAL IMAGING AND THERAPY BEAMLINE

A Thesis Submitted to the College of

Graduate Studies and Research

in Partial Fulfillment of the Requirements

for the Degree of Master of Science

in the Division of Biomedical Engineering

University of Saskatchewan

Saskatoon

By

Edward Anthony Muzar

PERMISSION TO USE

In presenting this thesis/dissertation in partial fulfillment of the requirements for a Postgraduate degree from the University of Saskatchewan, I agree that the Libraries of this University may make it freely available for inspection. I further agree that permission for copying of this thesis/dissertation in any manner, in whole or in part, for scholarly purposes may be granted by the professor or professors who supervised my thesis/dissertation work or, in their absence, by the Head of the Department or the Dean of the College in which my thesis work was done. It is understood that any copying or publication or use of this thesis/dissertation or parts thereof for financial gain shall not be allowed without my written permission. It is also understood that due recognition shall be given to me and to the University of Saskatchewan in any scholarly use which may be made of any material in my thesis/dissertation.

DISCLAIMER

The names of companies, corporations, brand names and websites were exclusively created to meet the thesis and/or exhibition requirements for the degree of Master of Science at the University of Saskatchewan. Reference in this thesis/dissertation to any specific commercial products, process, or service by trade name, trademark, manufacturer, or otherwise, does not constitute or imply its endorsement, recommendation, or favouring by the University of Saskatchewan. The views and opinions of the author expressed herein do not state or reflect those of the University of Saskatchewan, and shall not be used for advertising or product endorsement purposes.

Requests for permission to copy or to make other uses of materials in this thesis/dissertation in whole or part should be addressed to:

Head of the Division of Biomedical Engineering
University of Saskatchewan
Saskatoon, Saskatchewan S7N 5A9
Canada

OR

Dean
College of Graduate Studies and Research
University of Saskatchewan
107 Administration Place
Saskatoon, Saskatchewan S7N 5A2
Canada

ABSTRACT

Novel dosimetric materials to ensure properly calibrated x-ray beam profiles are required to facilitate the implementation of Microbeam Radiation Therapy in cancer treatment. Indirect conversion dosimetric materials are explored for possible future applications in Microbeam Radiation Therapy devices. The indirect conversion materials barium borophosphates, barium fluorophosphates with sodium ion modifier, and barium aluminosilicates were synthesized and studied. Each synthesized compound was also doped (or additionally co-doped) with a rare-earth compound. The rare-earth compounds used for doping included samarium (III) oxide, and samarium (III) fluoride. Codoping was explored with the compound erbium (III) chloride. Synthesized samples were x-ray irradiated at the Biomedical Imaging and Therapy beamline of the Canadian Light Source and also at the University of Saskatchewan. Experimental characterization methods of dosimetric material samples included x-ray luminescence, photoluminescence, electron spin resonance, Raman spectroscopy, absorbance spectroscopy, x-ray diffraction, differential scanning calorimetry, and modulated differential scanning calorimetry. The materials are experimentally characterized and determined for their merit in further research and development. All materials were found to scintillate, and some were found to function as x-ray storage phosphors as well. The barium borophosphates and also the barium fluorophosphates with sodium ion modifier possessed x-ray storage functionality according to photoluminescence spectra. An absorbance peak was observed after x-ray irradiation for barium fluorophosphates. Electron spin resonance data suggest that x-ray irradiation forms two similar types of paramagnetic defects for barium borophosphates. It appears that these defects are oxygen hole centres, which form during the indirect conversion process of samarium dopant cations. Indirect conversion involves samarium cation valency change from the 3+ to 2+ oxidation state, occurring when an electron is captured by the cation. Thermal analysis of the barium fluorophosphates by differential scanning calorimetry and modulated scanning calorimetry indicate preferential properties and moderate glass forming ability for manufacturing processes. It is concluded that barium fluorophosphates are best suited for dosimetric detectors, and secondly, barium borophosphates. Finally, future studies on materials for dosimetry in Microbeam Radiation Therapy are recommended.

ACKNOWLEDGEMENTS

Thank you to my supervisor, Dr. S. O. Kasap, and co-supervisor, Dr. L. D. Chapman, for providing me with the opportunity to attend graduate school under their leadership at the University of Saskatchewan and providing financial support through a Research Assistantship and by nominating me for the University of Saskatchewan Graduate Scholarship. Their support, guidance, instruction and dedication are important. I thank Dr. D. Tonchev, Dr. R. Sammynaiken, Dr. K. Kougiya, Dr. R. Johanson, Mr. J. Maley, Dr. G. Belev, Dr. I. Oguocha, Dr. Q. Yang and Dr. A. Moewes for their professional guidance and instruction. Furthermore, I thank my colleagues and the personnel at the University of Saskatchewan and at the Canadian Light Source. From IT4U services, I am grateful to the staff including Ms. J. Baier for help in the electronic formatting of this thesis.

Also, thank you to my parents, family, and friends.

TABLE OF CONTENTS

LIST OF TABLES

LIST OF FIGURES

LIST OF ABBREVIATIONS

Al	Aluminum
Al_2O_3	Aluminum (III) Oxide
As	Arsenic
A.U.	Arbitrary Units
B	Boron
B_2O_3	Boric Oxide
Ba	Barium
$BaBPO_5$	Barium Borophosphate
BaF_2	Barium Fluoride
BaO	Barium Oxide
BMIT	BioMedical Imaging and Therapy Synchrotron Beamline
Cl	Chlorine
CLS	Canadian Light Source
DSC	Differential Scanning Calorimetry
Er	Erbium
$ErCl_3$	Erbium (III) Chloride
ESR/EPR	Electron Spin Resonance/Electron Paramagnetic Resonance
F	Fluorine
FWHM	Full Width at Half Maximum
IR	Infrared
kVp	Peak Kilovoltage
La	Lanthanum
$LaCl_3$	Lanthanum Chloride
MDSC	Modulated Differential Scanning Calorimetry
MOSFET	Metal Oxide Semiconductor Field Effect Transistor
MRI	Magnetic Resonance Imaging
MRT	Microbeam Radiation Therapy
Na	Sodium
$NaCO_3$	Sodium Carbonate
$Na_4P_2O_7$	Sodium Pyrophosphate
O	Oxygen
PL	Photoluminescence
Si	Silicon
SiO_2	Silica
Sm	Samarium
SmF_3	Samarium Fluoride
Sm_2O_3	Samarium (III) Oxide
UV	Ultraviolet
Vis	Visible
w.r.t.	With respect to
XL, XRF	X-ray Luminescence/Fluorescence
XRD	X-ray Diffraction

1 INTRODUCTION

Microbeam Radiation Therapy (MRT) is a novel radiotherapy and radiosurgery technique utilizing a special x-ray radiation treatment method for the eradication of cancerous tissue in patients [1]. Radiotherapy, in general, has been proven effective and provides the benefits of cancer treatment, with benefits outweighing the negative impact on healthy tissue [2]. MRT, specifically, has been shown to destroy cancerous tissue, while largely sparing healthy tissue [2]. Effectual MRT treatment requires the design of dose detecting apparatus (dosimetric devices) with high spatial resolution or quantifiable temporal dose profile (dynamic range of dose) [3] to determine the quality of an x-ray source, viz. the BioMedical Imaging and Therapy Synchrotron Beamline (BMIT) at the Canadian Light Source (CLS). Furthermore, the dose detecting apparatus must be stable for multiple readouts and ongoing reliability. Current dosimetric devices are currently limited with regards to spatial resolution and high dose uncertainty, making these dosimeters unsuitable for MRT. Examples of current state of the art dosimeters are ion chambers with low spatial resolution and Gafchromic films with high dose uncertainty [3]. With high dose uncertainty, dose temporal profiling and dynamic range readings are difficult. Another issue found in currently available dosimetric devices which would otherwise fulfill the aforementioned material and device requirements is the lack of quick and practical read-out times of dose; a setback found in some dosimetric technologies such as Metal Oxide Semiconductor Field Effect Transistor (MOSFET) devices, Magnetic Resonance Imaging (MRI) gel dosimetry, and fluorescent nuclear track detectors [3].

This device limit stems fundamentally from inadequate materials at present. In order to build a dosimetric device capable of accurate dose quality assay and read-out to enable this new therapeutic technology, novel materials with associated material production processes are required. Thus, various select synthesized dosimetric materials will be examined, and pertinent material properties will be determined, corroborated by experimental data. Each material and associated method of synthesis will be concluded with respect to its potential applicability in the development of novel materials for an effective dosimetric device design. Furthermore,

suggestions will be made for future study to obtain materials for the design of dosimetric detectors with adequate spatial resolution, accurate temporal dose profile, and stability.

In this introductory section, each major topic will be established. These topics include: MRT, Synchrotron Radiation for Cancer Therapy, Material Requirements, X-ray Detection, Material Synthesis, Characterization, and Thermodynamic Stability. Finally, a subsection of objectives and research scope pertinent to this project will be introduced to further acquaint the reader to the purpose of this specific research in relation to the development of MRT and synchrotron radiation for therapy. This research will be shown to be a necessary initial step in the development of a practical MRT dosimetric detector.

1.1 MRT for Cancer Treatment

MRT has the potential to be a viable treatment option for cancer in brain tumours [1]. The process of a patient undergoing a cancer treatment is illustrated in Figure 1.1.

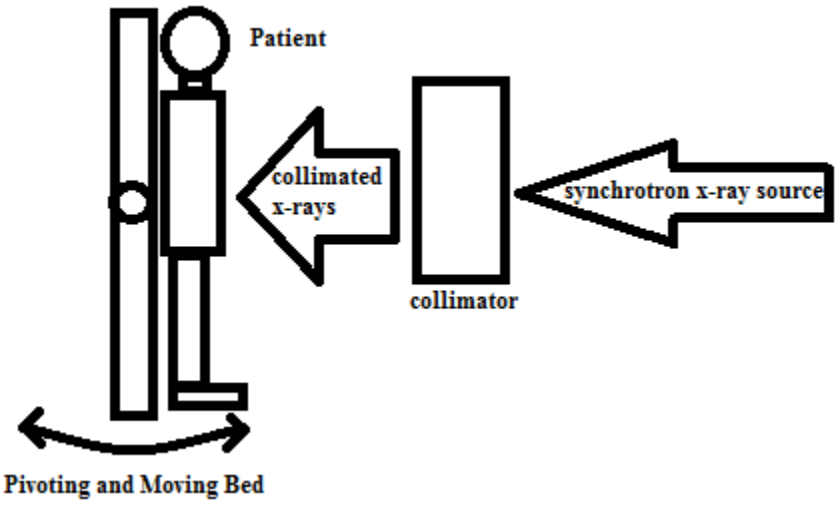

Figure 1.1 Illustration of MRT in a clinical setting.

As is illustrated in Figure 1.1, the patient lies on a moving bed platform, allowing positioning of the cancerous tissue in the path of the beam. The moving bed allows varying spatial positioning of the patient and hence facilitating additive x-ray treatment of the cancer affected tissue, whilst sparing any non-cancerous tissue from continuous irradiation, which would cause higher dose as a repercussion. Thus, the MRT patterned beam exposure of the tumour at the isocentric target is the highest of all affected tissues in the body [1].Thus, with such oblique beam angles, in addition to a normal beam as illustrated above, the patient would receive adequate dose in the cancerous areas and minimal x-ray dose in non-cancerous tissues that are along the beam path.

An important aspect of MRT and which distinguishes this therapy from conventional cancer therapies is the unique type of collimated beam utilized. The beam is a composite of narrow spatial width high dose rate regions that are spaced by low dose regions of much larger spatial width. In Figure 1.2, below, an idealized conceptualizing graph is shown, not to demonstrate the dose scale, but to emphasize important features of the beam. As is seen in Figure 1.2, the high dose peaks are of smaller width, with much longer periodic low dose spacing, called the valley, which is of relatively large width with respect to the peak widths. The combination of narrow but high dose peaks, and also the low dose, but wide valleys, is the essence of MRT and its unique beam properties [1].

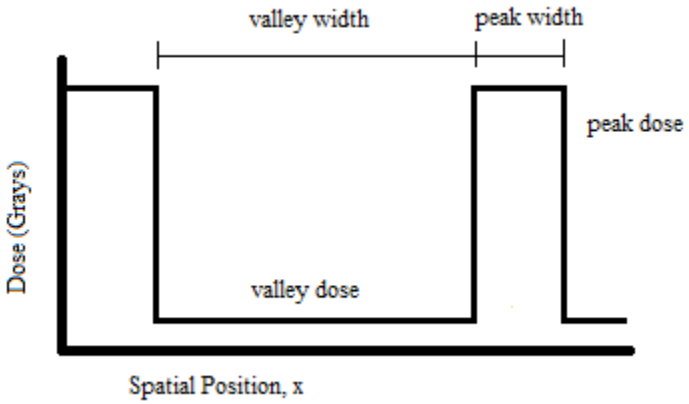

Figure 1.2 An idealized microbeam, showing two peaks spaced by a low dose valley.

In practice, the idealized nature of the Figure 1.2 is not attained. In reality, the infinite slope (as shown) transition between the valley and peak doses is finite; there is a steep dose slope, yet it is

still a gradual transition [2]. Peak doses are usually at least in the 100's of Gy and applied with high dose rates [4]. Valley doses are usually 10 to 100 times less than the peak doses [2]. MRT utilizes x-rays with energies which range typically from 10 to 100 keV [2]. The valley width is 200 μm wide and peaks have widths around 25 μm for the BMIT beamline at the Canadian Light Source. The two adjacent dimension lines, one for the valley width and the other for the peak width, form one single period in the spatial dose modulation of high and low doses. Figure 1.2 demonstrates the spatial dose modulation; one whole valley and one whole peak comprise one full period of spatial dose modulation.

1.2 Synchrotron Beamline X-ray Sources

The development of therapeutic synchrotron beamlines is contingent on the development of specific cancer treatment methods that are more effective than analogous traditional treatment methods, according to [2]. Synchrotron radiation is indispensable for the application of MRT. The x-ray beam generated by use of synchrotron radiation is composed of low divergence x-rays, which is necessary in MRT to minimize fanning and eventual blurring of the beam further along the path [2].Thus, by the development of MRT for specific cancer treatments, and utilizing the exceptional advantages of synchrotron radiation which are uniquely suited for delivering MRT, therapeutic beamlines have the potential to become viable alternatives to traditional methods of radiotherapy.

1.3 Materials Requirements for MRT

Such a complex of microbeams separated spatially with low dose spacing creates a unique problem for dose detection and profiling in MRT systems. The proper calibration and testing of such a system would be difficult (if not impossible practically) with the aforementioned current state of the art technologies. The absence of a calibration and beam testing system would add unacceptable risk unnecessarily to the patient undergoing such treatment. In order to lower the

risks of MRT and ensure quality treatment, the beamline must be calibrated prior to treating patients, and thus, novel dosimetric materials are necessary to facilitate calibration and testing.

1.4 Detection of X-ray Radiation

The indirect conversion type of x-ray detectors are studied in this work. Direct detectors are also explained in this section in order to show the contrasting mechanisms of dose signal generation. In general, detector materials must be responsive, sensitive, and produce a relatively large amplitude signal relative to noise to facilitate dose detection [5]. The method that each detector type accomplishes dose detection differs. In Figure 1.3, the dosimetric material serving as a model for a general detector is shown to be irradiated by collimated synchrotron x-ray radiation. These distinctions between detector types is explained and illustrated below in Subsections 1.4.1 and in 1.4.2.

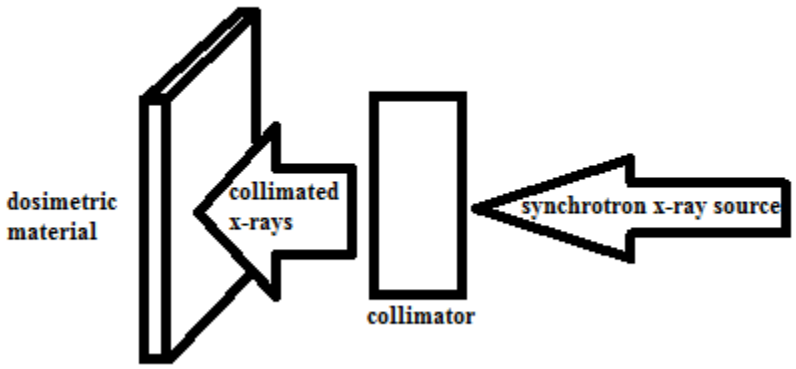

Figure 1.3 X-ray dose detection using a pixel of dosimetric material.

1.4.1 Indirect Conversion Detectors

Indirect Detection is the phenomenon in which an x-ray photon is converted into a light photon. For light generated immediately during x-ray irradiation, this is termed scintillation [6]; hence,

scintillation is a form of x-ray luminescence/fluorescence (XL/XRF) but with light emission. When x-ray irradiation occurs, colour centres are also formed in materials. These electronic defects in the converted material are subsequently excited with a laser to produce photoluminescence (PL). An x-ray storage phosphor retains x-ray induced defects which can afterwards be excited [7]. Thus, x-ray dose read-out via PL has potential for x-ray storage phosphor function.

Thus, indirect detection is shown to rely on x-rays generating light for dose determination. Figure 1.4 shows one unit of detector material, a pixel, which is probed for x-ray dose. In this illustration, XL assay relies on concurrently x-ray irradiating the indirect conversion material, in order for the material to scintillate light, which is captured by a spectrometer. The light captured by a spectrometer may be recorded as counts or intensity versus wavelength. This emission spectrum is effectively a fingerprint of x-ray dose deposited in the irradiated indirect conversion material.

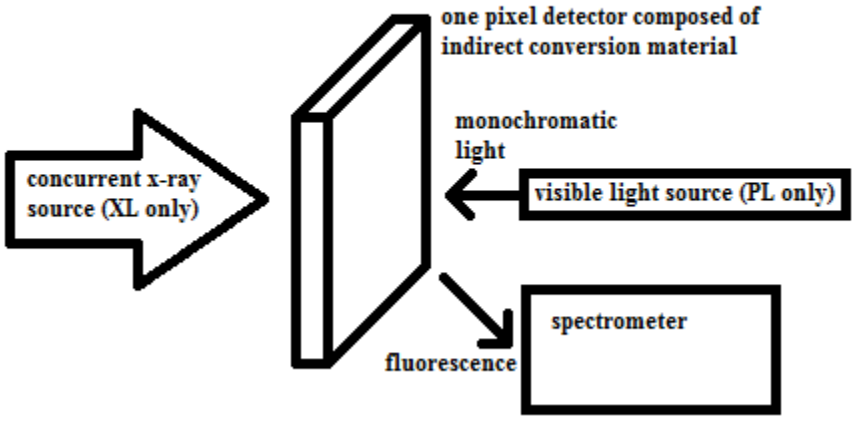

Figure 1.4 A setup for indirect dose detection.

The PL spectroscopic assay method operates under similar principles as XL in terms of dosimetric material fluorescence registered by a spectrometer; however, the excitation source is not from x-rays. The excitation source in PL is a light source. This excitation light source can be laser light. In both XL and PL, the radiation source excites electrons to higher energy states.

These excited electrons eventually return to their ground state and emit light with a wavelength characteristic of those transitions, and thus information on x-ray dose.

1.4.2 Direct Conversion Detectors

Direct Detection on the other hand, requires no separate apparatus to generate an electric signal; x-ray energy and consequently dose can be directly converted into an electric signal. The deposition of dose in the direct conversion material causes a current in Figure 1.5 to increase, which can then be interpreted, in this setup, by an ammeter. This setup, relative to the indirect detection setup from Figure 1.4, is simpler in the number of steps necessary between x-ray dose deposition and an electric signal; x-ray deposition automatically generates an electric signal in the form of a current with no intermediate excitation and detection via a spectrometer steps.

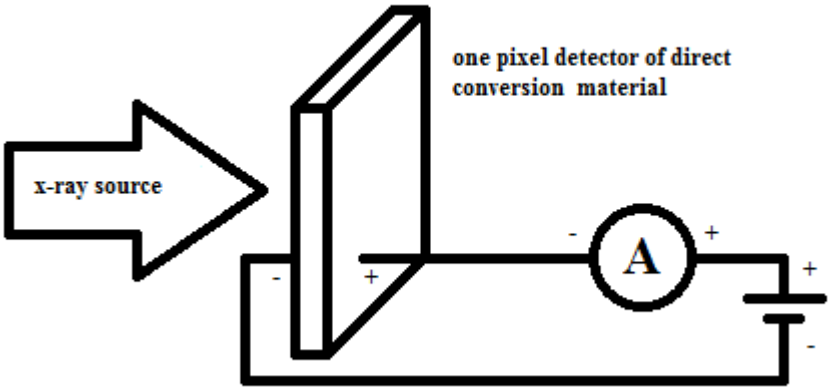

Figure 1.5 A setup for direct dose detection.

X-rays create electron-hole pairs in the material, which in turn can be driven as a current by an electric field [6]. Figure 1.5 illustrates a setup that can enable determination of total x-ray dose deposited, by following the electron-hole pair production. A cell used as a voltage source drives an electric current in the circuit that includes the direct detector pixel and ammeter A. As the x-ray energy is absorbed by the material, the energy excites electrons to the conduction band, effectively lowering the resistance of the material. With a lower effective resistance from

additional electrons in the conduction band and concomitantly formed holes in the valence band, the circuit drives more current, with the ammeter registering a higher current. Thus, x-rays can be immediately converted into an electric signal of dose, contrasting indirect conversion detectors which require intermediate steps to generate an electric signal of dose.

1.5 Characterization of Materials

The testing methods as shown in Section 1.4 also serve as characterization techniques for materials. The methods introduced include XL and PL for indirect detector materials, and electric current measurement for direct detector materials. These characterization methods form the preliminary study of any dosimetric materials. The measurement of dose relies on these aforementioned techniques, and thus is required to demonstrate the dosimetric functionality of the materials.

Other experimental techniques will explore the mechanisms of dosimetric function in the candidate materials and also the thermal properties for stability. These techniques include electron spin resonance (ESR), absorption spectroscopy, Raman spectroscopy, x-ray diffraction (XRD), differential scanning calorimetry (DSC), and modulated DSC (MDSC).

1.6 Thermal Stability of Materials

To ensure the quality of the dosimetric materials in the beamline therapy service environment, and also for its processing characteristics, the candidate materials undergo thermal analysis. For instance, the quality of a dosimetric material such as glass relies on its homogeneity and also stability from undergoing crystallization and compositional breakdown [8]. The stability of glass against crystallization is termed devitrifcation [5]. Thermal analysis techniques probe for alterations in material properties due to controlled temperature variation [9]. In this study, thermal analysis consists of testing materials via DSC and MDSC experimental methods for thermodynamic data. DSC and MDSC methods enable the determination of thermal properties

by controlling the temperature of material samples which follow specific temperature versus time curves [9]. For x-ray storage phosphor functionality, a material must have room temperature electronic defects retained after x-ray irradiation [7]. Thus, ESR [7], absorption spectroscopy [10], will be utilized to detect electronic defects, and PL will be utilized to determine actual x-ray storage phosphor function. The thermodynamic information in turn allows accurate prediction of material thermal stability. With the thermodynamic stability determined, the material is evaluated on its merit for use as a dosimetric material in device designs. Device designs include manufacturing processes which have thermal property constraints and tolerances which may preclude the candidate material with unsatisfactory thermal properties.

1.7 Objectives and Scope of Research

The aim of this study is to develop dosimetric materials and their applicability in MRT at BMIT. This entails the synthesis and processing of various materials, followed by material testing for dose measurement and experimental characterization of other material properties. Dosimetric testing consists of x-ray irradiating candidate material samples at BMIT with synchrotron radiation and also irradiating conventionally with an x-ray tube source. The material properties include optical, paramagnetic, structural and thermal properties of select synthesized materials. Some material properties are assayed before and after when radiation effects were thought to be crucial to the material development. These initial steps in development are necessary in realizing a material with specific properties applicable to MRT dosimetry at a synchrotron beamline.

The scope of the work will cover the synthesis, characterization of properties and study of the potential of specific dosimetric materials. These materials include the following indirect conversion materials: barium borophosphates, barium fluorophosphates, and barium aluminosilicates, all doped with Sm compounds, and a barium borophosphate with additional Er compound codoping. Each candidate material's testing and characterization routine will include at least PL and XL experimental work. The aforementioned materials and the experimental study of these materials constitute the body of this work.

2 BACKGROUND THEORY AND PRIOR STUDIES

In this chapter, the pertinent theory is reviewed, as well as current knowledge in the topics associated with this study. The theory will include study of the experimental techniques utilized and also the relation between experimental techniques and properties that can be determined thereof on the candidate materials. Also, a review of materials and the potential to be applied to dosimetric devices will be presented.

2.1 Theoretical Fundamentals and Experimental Techniques

In this section, XL and PL theory will first be reviewed. These two experimental techniques form the basis for which each candidate indirect conversion material can be tested on its dosimetric properties and merit. XL and PL will be reviewed first; followed subsequently by Raman spectroscopy, absorption spectroscopy, XRD, ESR, DSC and MDSC. The experimental techniques other than XL/PL will provide complementary information on the chemical and electronic structure of materials and be shown to elucidate the process of depositing dose in a dosimetric material, the stability of the material and reveal possible methods for successful dosimeter development.

2.1.1 XL and PL, and Determining Dosimetric Functionality

XL and PL both rely on an external excitation source. The excitation source is an x-ray source and an ultraviolet/visible/infrared radiation source, respectively. Electromagnetic energy from the source is absorbed by a material and excites its electrons from lower to higher electron energy levels. It is possible for such electrons in their higher energy levels to dissipate energy by emitting electromagnetic radiation. By dissipating electromagnetic energy, electrons can occupy lower energy orbitals. The energy change absorbed or emitted electromagnetically by each

electron is a photon. The emitted photon may contribute to the luminescence intensity observed by a spectrometer. Since photons from the excitation source can alternatively be scattered by the material, a spectrometer can also observe a usually high intensity peak centred on the excitation frequency.

There are two types of electron energy transitions which occur: allowed and forbidden. An electronic transition between energy levels is allowed when the following selection rules are satisfied [11]:

$$\Delta l = \pm 1 \quad (2.1)$$

$$\Delta s = 0 \quad (2.2)$$

$$\Delta j = \pm 1, \text{or } \Delta j = 0 \text{ with } j \neq 0 \quad (2.3)$$

where l is the orbital angular momentum, s is the intrinsic electron spin angular momentum, j is the total angular momentum, and Δ indicates the change in the aforementioned quantities due to transition in quantum states. Forbidden transitions violate these selection rules. According to these selection rules, forbidden transitions do not occur; however, in the case of rare earth ions used as dopants, forbidden transitions do occur [12]. Although both types of transitions could occur, forbidden transitions are markedly different. The qualitative comparison of forbidden and allowed peaks is given in Table 2.1. Forbidden transitions occur due to the nephelauxetic effect [12]; large ions like rare earth ions are outer electron shielded from the host material and external effects. Thus, rare earth ions have fine structure spectral peaks which are very narrow.

Table 2.1 Qualitative Features of Forbidden and Allowed Transitions [12].

Transition	Peak Intensity	Fine Structure Peak Width
Forbidden	Low	Narrow
Allowed	High	Broad

2.1.2 Raman Spectroscopy

When a beam from a monochromatic light source such as laser is directed on a material, there is a possibility that light will be scattered by the material with a wavelength unlike that of the source, in addition to the scattered monochromatic wavelength [13]. This inelastic scattering

with dissimilar wavelengths is called Raman scattering and for wavelengths of light scattered which are greater than the source wavelength, are each termed a Stokes' Shift [14]. This phenomenon arises from the incoming light interaction, which alters the polarizability of the material [15]. Specifically, the Stokes' Shift occurs by loss of energy of the photon, to the thermal vibrations of the material [15].

2.1.3 Absorption Spectroscopy

Absorption of electromagnetic radiation in materials follows the Beer-Lambert Law [16]:

$$I(\lambda) = I_o \mathrm{e}^{-\mu(\lambda)\rho\delta} \tag{2.4}$$

where μ is the mass absorption coefficient, ρ is the density and δ is the thickness of the material, normal to the direction of x-ray irradiation. The mass absorption coefficient and density are then material dependent. Equation (2.4) is in the form that is useful for x-ray absorbance. For light absorption spectroscopy, the following equation [10] is more suitable:

$$I(\lambda) = I_o \mathrm{e}^{-\alpha(\lambda)\delta} \tag{2.5}$$

Also, the transmitted intensity I shows wavelength dependence since the material's mass absorption coefficient and absorption coefficient are light wavelength dependent. With light wavelength dependence, materials exhibit wavelength dependent spectra. In fraction of light intensity transmitted form, Equation (2.5) becomes,

$$T = \frac{I}{I_o} = \mathrm{e}^{-\alpha(\lambda)\delta} \tag{2.6}$$

This ratio between transmitted intensity and incoming intensity, T, is the transmittance.

When a material is x-ray irradiated, colour centres rise to excited states and the material consequently has an altered light absorption spectrum [10]. Thus, the absorption coefficient changes due to x-ray irradiation. The difference in absorption spectrum can be determined by measuring the percent of light transmitted before and after x-ray irradiation. Light excitation can remove colour centres from materials, whereby the colour centre electron is removed and

transferred to a dopant ion [10]. Therefore, the energy range of photon absorption will elucidate the electron energy associated with the colour centre.

2.1.4 X-ray Diffraction

Diffraction in crystalline materials occurs when the atomic planes interact with x-ray radiation in the form of diffraction gratings, which in turn produce certain in-phase, diffracted x-ray beams, characteristic of the crystalline planar spacing [17]. The relation between the x-ray wavelength, λ, and the interatomic layer spacing, d, satisfies Bragg's Law [17]:

$$n\lambda = 2d \sin\theta \tag{2.7}$$

where θ is the angle of incline the x-ray beam creates with the interatomic layer plane and n is taken to be unity for first order reflections. Thus, with n equalling 1,

$$\lambda = 2d \sin\theta \tag{2.8}$$

With isolation of the sinusoidal factor on the left hand side, the constraint on wavelength for its maximum is demonstrated mathematically [17],

$$\frac{\lambda}{2d} = \sin\theta$$
$$\sin\theta \leq 1$$
$$\frac{\lambda}{2d} \leq 1$$
$$\lambda \leq 2d \tag{2.9}$$

Thus, XRD can occur in crystalline materials when x-ray wavelengths are sufficiently small according to Equation (2.9); however, the angle of incline of the x-ray beam θ must be such that it will generate a sufficient diffracted beam intensity that can be measured.

The crystal grain size can determined using XRD by examining peak widths arising from intensity versus double angle plots [18]. The grain size L can be calculated by the Scherrer formula [18]:

$$L = \frac{0.9\lambda}{\cos\theta}\frac{1}{\Delta(2\theta)} \tag{2.10}$$

where the FWHM peak width Δ(2θ) is calculated by the equation [18]:

$$\Delta(2\theta) = \sqrt[2]{[\Delta(2\theta)]^2_{\text{sample}} - [\Delta(2\theta)]^2_{\text{reference}}} \tag{2.11}$$

where the sample peak width squared, $[\Delta(2\theta)]^2_{\text{sample}}$ has the large crystal limit peak width reference squared, $[\Delta(2\theta)]^2_{\text{reference}}$, subtracted. If the reference width is taken to be approximately zero, Equation (2.11) simplifies to

$$\Delta(2\theta) = \sqrt[2]{[\Delta(2\theta)]^2_{\text{sample}} - 0} = [\Delta(2\theta)]_{\text{sample}} \tag{2.12}$$

Thus from XRD, the grain size determination and crystalline structure associated with the diffraction crystalline atomic planes.

2.1.5 ESR and its use in Determining Electronic Structure

In general, magnetic resonance techniques, which include ESR, are very useful for probing matter containing magnetic ions [19]. ESR is the spectroscopy wherein a sample material is exposed to a magnetic field which in turn causes absorption of impinging electromagnetic radiation by the material [20]. The radiation energy is absorbed via valence electrons and is due to the magnetic dipole moments arising from electron angular momentum (intrinsic spin and orbital contributions) and its interactions [21]. The valence electrons are promoted from a lower paramagnetic energy state to a higher paramagnetic energy state, with the difference in these energy levels being resonant with the quanta of radiation energy absorbed [20]. Thus, for unpaired electrons, the magnetic field causes the degenerate magnetic energy states to become non-degenerate and consequently sensitive to resonant radiation energy absorbance. An algebraic explanation can also be used to elucidate the fundamental phenomenon of ESR [20]. The energy of a quantum of light, a photon, is:

$$E = h\,\nu \tag{2.13}$$

where E is the energy of the photon, h is unreduced Planck's constant and ν is the electromagnetic frequency. An external magnetic field **B**, a vector with a magnitude B, is applied to the material, so that **B** is oriented in the direction relative to the magnetic moment $\boldsymbol{\mu}$, which is also a vector, but with magnitude $g\mu_B$ where g is the g-value constant and μ_B is the Bohr Magneton (as defined in Equation (2.15) below) [21]. Thus, the direction of the applied magnetic field is oriented in the direction that is opposite to the magnetic moment; hence, $-\boldsymbol{\mu}\cdot\boldsymbol{B} > 0$. The difference in paramagnetic energy between the lower energy state E_1 and higher energy state E_2 is $(E_2 - E_1)$ and this difference can be related to the potential arising from the magnetic field interacting with the magnetic moment by the following equation [20]:

$$E_2 - E_1 = -\boldsymbol{\mu} \cdot \mathbf{B} = g\,\mu_B\,B \tag{2.14}$$

$$\mu_B = \frac{e\,h}{4\,\pi\,m_e c} \tag{2.15}$$

where g is again the g-value constant and μ_B is the Bohr Magneton which is shown below the equation to be composed of constants including electron charge e, unreduced Planck's constant h, electron mass m_e, and speed of light in a vacuum c. The resonance condition for paramagnetic resonance is when the photon energy matches the difference in energy between states [20]:

$$E_2 - E_1 = h\,\nu \tag{2.16}$$

By replacing the difference in energy $(E_2 - E_1)$ between states with its relation to the B field, the resonance equation becomes:

$$h\,\nu = g\,\mu_B\,B \tag{2.17}$$

Equation (2.17) relates the photon energy in terms of its electromagnetic frequency to the magnetic field. With this equation rearranged, observed peaks in intensity versus applied magnetic field allow the g-value to be computed, characterizing the resonance:

$$g = \frac{h\,\nu}{\mu_B\,B} \tag{2.18}$$

The photon energy term corresponds to the radiation frequency used to excite the electron and the applied magnetic field refers to the applied magnetic field at the moment its peak occurs.

The Heisenberg Uncertainty Principle limits the peaks observed in experimental work from possessing infinitesimal peak widths in energy and high energy state lifetime; the peaks are of

finite, non-zero widths and are characterized with the FWHM method [20]. As a consequence, peaks are also of finite width for intensity versus applied magnetic field, and mathematically the relation of lifetime and applied magnetic field peak widths can be seen from the equation [20]:

$$\text{FWHM} = \Delta B = \frac{2\,\hbar}{g\,\mu_B\,T_{lifetime}} \tag{2.19}$$

where $\hbar$ is the reduced Planck`s Constant, g is the g-value, μ_B is the Bohr Magneton, T_{lifetime} is the lifetime, and these quantities are related to the ΔB calculated from the FWHM method. From this equation, the inverse mathematical relation between peak width and lifetime is established for spin-spin interactions, which characterizes interactions between magnetic ions in concentration usually more than 0.1% [20]. By substituting for the g-value in Equation (2.19) with the relation from Equation (2.18), and isolating for the lifetime, the following equation is obtained,

$$T_{lifetime} = \frac{B}{\nu(\Delta B)\pi} \tag{2.20}$$

Equation (2.20) is useful in determining the lifetime of a transition with experimentally determinable parameters of frequency ν, applied field B and half width ΔB which is from the FWHM of a Lorentzian curve.

Curve fitting such a broadened peak is done by modelling the peak either as a Lorentzian function, or a Gaussian function, given by the following equations [20]:

$$Intensity_{Lorentzian} = I_L = I_o\,(1 + a^2(B - B_o)^2)^{-1} \tag{2.21}$$

$$Intensity_{Gaussian} = I_G = I_o\,e^{-b^2(B-B_o)^2} \tag{2.22}$$

$Intensity_{Lorentzian}$ and I_L refer to the Lorentzian intensity, which is a function of the applied magnetic field B. $Intensity_{Gaussian}$ and I_G refer to the Gaussian intensity, which is also a function of applied magnetic field B. Each curve has its peak centred at B_o, which allows by its inspection and concomitant use of Equation (2.18) the determination of the g-value associated with that peak. The constant I_o in both Equation (2.21) and Equation (2.22) is the peak intensity; the remaining factors in each equation form an envelope less than to unity or equalling unity at the peak. Both the former and latter have a constant that controls curve width, viz. a and b,

respectively, and these can be related mathematically to the FWHM by the definition of FWHM. For the Lorentzian function, half intensity is when

$$I_L = \frac{1}{2} I_o \tag{2.23}$$

Then, by applying the FWHM definition to Equation (2.21), and followed by algebraic reorganization,

$$\begin{gathered} \frac{1}{2} I_o = \frac{I_o}{1 + a^2 (B - B_o)^2} \\ 1 + a^2 (B - B_o)^2 = 2 \\ a^2 (B - B_o)^2 - 1 = 0 \\ (a(B - B_o) + 1)(a(B - B_o) - 1) = 0 \end{gathered} \tag{2.24}$$

At this point, the Lorentzian equation at half intensity is rearranged in the form as seen in Equation (2.24) which shows the difference of squares and the *B* field from each of the root is isolated:

$$(a(B_{root\,1} - B_o) \pm 1) = 0 \tag{2.25}$$

$$B_{root\,1} = -\frac{1}{a} + B_o, \quad and \quad B_{root\,2} = +\frac{1}{a} + B_o \tag{2.26}$$

According to the FWHM method, the width is the distance between roots one and two, thus,

$$\Delta B = B_{root\,2} - B_{root\,1} = (\tfrac{1}{a} + B_o) - (-\tfrac{1}{a} + B_o)$$

$$\Delta B = \tfrac{2}{a} \qquad \text{or,} \qquad a = \tfrac{2}{\Delta B} \tag{2.27}$$

The result shown in Equation (2.27) in its latter form can then be substituted into Equation (2.21) for constant *a* and explicitly show the mathematical connection between peak width and Lorentzian function:

$$\begin{gathered} I_L = I_o \left(1 + \frac{2^2 (B - B_o)^2}{(\Delta B)^2}\right)^{-1} \\ I_L = I_o \left(1 + \frac{4(B - B_o)^2}{(\Delta B)^2}\right)^{-1} \end{gathered} \tag{2.28}$$

A similar methodology can be applied to the Gaussian function. Starting from the definition of FWHM, the intensity at half maximum is

$$I_G = \frac{1}{2} I_o \tag{2.29}$$

Applying this definition to Equation (2.22), and then followed by algebraic reorganization,

$$\frac{1}{2} I_o = I_o \, \mathrm{e}^{-b^2 (B - B_o)^2}$$

$$\mathrm{e}^{b^2 (B - B_o)^2} = 2$$

$$\ln 2 = b^2 (B - B_o)^2$$

$$b^2 (B - B_o)^2 - \ln 2 = 0$$

$$(b(B - B_o) + \sqrt{\ln 2})(b(B - B_o) - \sqrt{\ln 2}) = 0 \tag{2.30}$$

In this algebraic form, the equation is now a difference of squares. The two roots from this equation are separated and the B field from each root isolated,

$$\left(b(B - B_o) \pm \sqrt{\ln 2}\right) = 0$$

$$B_{root\,1} = -\frac{\sqrt{\ln 2}}{b} + B_o \tag{2.31}$$

$$B_{root\,2} = +\frac{\sqrt{\ln 2}}{b} + B_o \tag{2.32}$$

According to the FWHM method, the width is the distance between roots one and two, thus,

$$\Delta B_{half} = B_{root\,2} - B_{root\,1} = \left(\frac{\sqrt{\ln 2}}{b} + B_o\right) - \left(-\frac{\sqrt{\ln 2}}{b} + B_o\right)$$

$$\Delta B = 2\frac{\sqrt{\ln 2}}{b} \tag{2.33}$$

$$b = 2\frac{\sqrt{\ln 2}}{\Delta B} \tag{2.34}$$

Substituting the equivalent form of b from Equation (2.34) into Equation (2.22), yields

$$I_G = I_o \, e^{-\frac{2^2 \left(\sqrt{\ln 2}\right)^2 (B - B_o)^2}{(\Delta B)^2}}$$

$$I_G = I_o \, e^{-\frac{4 \ ln\, 2 \ (B - B_o)^2}{(\Delta B)^2}} \tag{2.35}$$

Equation (2.28) and Equation (2.35) show mathematically the relation between the Intensity function and FWHM peak width. Equation (2.28) and Equation (2.35) can now be used to fit experimental data as they have parameters that are relatable the intensity versus applied field data.

2.1.6 DSC, MDSC and Thermal Analysis

Differential Scanning Calorimetry (DSC) and its relevant device, the Differential Scanning Calorimeter (also referred to as DSC) will be explained and discussed as an analytical tool for the study of a material's thermodynamic and kinetic properties. Examples will be introduced from literature and methods of analysis of data. Modulated DSC (MDSC) will also be discussed.

DSC is a material testing tool which is utilized to gather data that is used in thermal analysis of materials [9]. Thermal Analysis is the process of discerning differences in material properties caused by varying the material temperature in experiments [9]. It can be used to identify a material, based on measured properties of a known sample [9]. The DSC experiment is conducted by increasing the temperature of a material sample at a rate (constant for DSC, but non-linear for MDSC), and by measuring and comparing the power heat flow to that of an empty sample module. The sample and empty module are intended to always be at nearly the same temperature [9]. The material sample is also contained in a sample module, like the empty sample module, and these containers are typically metal sealed pans with lids. The pans with lids can be made of aluminium.

Modulated DSC (MDSC) is a variant of DSC involving heating rates that has modulation with time [22]. DSC will usually have a temperature as function time in the form [22]:

$$T(t) = T_o + \beta t \qquad (2.36)$$

where T_o = initial temperature, $\beta = (dT/dt)$ is linear, t = time. MDSC will have this temperature function but with an added term for modulation with an angular frequency $\omega = 2\,\pi / P$ with P as the period in time of modulation [22]:

$$T(t) = T_o + \beta\, t + B \sin(\omega t) \qquad (2.37)$$

where B is the modulation amplitude. Its derivative w.r.t. t is then [22]:

$$dT/dt = \beta + \omega B\cos(\omega t) \tag{2.38}$$

With $dQ/dt = \beta C_p$, the heat flow would hence be [22]:

$$dQ/dt = C_p(\beta + \omega B\cos(\omega t)) \tag{2.39}$$

There are two heat flow components in DSC and MDSC: reversible and irreversible. DSC cannot separate these two heat rate components but MDSC can due to the modulation in heat rate [23]. The reversible component of heat can be due to crystal melting and glass transition, while the non-reversible component is due kinetic processes, such as crystallization and structural relaxation [23]. The reversing and non-reversible heat flow components are separated computationally using Fourier transforms [9].

The heat supplied, Q, to the sample is related to internal energy U, temperature T, pressure p, volume V, and number of moles n [24]. Those latter parameters are related to the change in heat by the first law of thermodynamics [24]:

$$dQ \;=\; dU \;+\; pdV \tag{2.40}$$

with

$$dU \;=\; \left(\frac{dU}{dT}\right)_{V,n} dT \;+\; \left(\frac{dU}{dV}\right)_{T,n} dV \;+ \left(\frac{dU}{dn}\right)_{T,n} dn \tag{2.41}$$

hence,

$$dQ \;=\; \left(\frac{dU}{dT}\right)_{V,n} dT \;+\; \left(\frac{dU}{dV}\right)_{T,n} dV \;+ \left(\frac{dU}{dn}\right)_{T,n} dn + pdV \tag{2.42}$$

Therefore, with a temperature rate dT/dt (where t = *time*) a time dependent heat flow is:

$$\frac{dQ}{dt} = \left(\frac{dU}{dT}\right)_{V,n} \frac{dT}{dt} + \left(\frac{dU}{dV}\right)_{T,n} \frac{dV}{dt} + \left(\frac{dU}{dn}\right)_{T,n} \frac{dn}{dt} + p\frac{dV}{dt} \tag{2.43}$$

A sample is usually hermetically sealed in a container; and hence, a closed system. Assuming the material loses no material and the volume of the system remains the same, then the following terms in Equation (2.43) become zero:

$$dV/dt \;=\; dn/dt \;=\; 0$$

And therefore,

$$\frac{dQ}{dt} = \left(\frac{dU}{dT}\right)_{V,n} \frac{dT}{dt} \tag{2.44}$$

Enthalpy, which accounts for work done with increasing the volume due to pressure, is defined as [24]:

$$H = U + pV \tag{2.45}$$

Hence, in differential form, and assuming no work done due to volume expansion,

$$dH = dU + d(pV) = dU$$

Therefore,

$$\frac{dQ}{dt} = \left(\frac{dH}{dT}\right)_{V,n} \frac{dT}{dt} \tag{2.46}$$

The heating rate *dT/dt* is determined by the user and the DSC will register the power *dQ/dt*. Thus, with this information, enthalpy over a temperature range can be determined by rearranging the equation and integrating with respect to variable temperature T from T_1 to T_2:

$$H(T_2) - H(T_1) = \int dH = \int_{T_1}^{T_2} \frac{(dQ/dt)}{(dT/dt)}\, dT \tag{2.47}$$

With this information, a peak arising from the thermogram can be integrated with respect to temperature and establish the enthalpy of transition.

Another important thermodynamic parameter is specific heat capacity C_p, which is a function of temperature T, which can be related to dQ by [24]:

$$dQ = V\rho C_p dT = mC_p dT \tag{2.48}$$

where ρ = density = (mass, m)/(volume, V) and hence with time,

$$\frac{dQ}{dt} = V\rho C_p \frac{dT}{dt} = mC_p \frac{dT}{dt} \tag{2.49}$$

This equation can be related to the *dQ/dt* from Equation (2.46):

$$\left(\frac{dH}{dT}\right)_{V,n} \frac{dT}{dt} = V\rho C_p \frac{dT}{dt} = mC_p \frac{dT}{dt}$$

$$\left(\frac{dH}{dT}\right)_{V,n} = V\rho C_p = mC_p \tag{2.50}$$

Then, this new equation can be used to isolate C_p:

$$C_p = \frac{\left(\frac{dH}{dT}\right)_{V,n}}{V\rho} = \frac{\left(\frac{dH}{dT}\right)_{V,n}}{m} \tag{2.51}$$

The relation of specific heat capacity shows the thermodynamic relation to the infinitesimal change of enthalpy with an infinitesimal increase in temperature. Constant volume and no increase in material are assumed. Heat capacity can also be calculated with the use of the heat rate and heat flow [22]. Thus, with rearrangement of Equation (2.49), the heat capacity can be calculated using the heat rate and heat flow from a thermogram:

$$C_p = \frac{\left(\frac{dQ}{dt}\right)}{\left(\frac{dT}{dt}\right)} V\rho = \frac{\left(\frac{dQ}{dt}\right)}{\left(\frac{dT}{dt}\right)} m \tag{2.52}$$

The DSC used in this research is a heat flux type. A heat flux type DSC operates by measuring the heat flux associated between a sample and a reference, due to a temperature difference [25]:

$$q = \frac{\Delta T}{R} \tag{2.53}$$

where $\Delta T = T_s - T_r$ and R is the thermal resistance. A more complicated expression is used to model the calorimeter cavity geometry of specific the DSC model [25]:

$$q = -\frac{\Delta T}{R_r} + \Delta T_0 \frac{R_r - R_s}{R_r R_s} + (C_r - C_s)\frac{dT_s}{dt} - C_r \frac{d\Delta T}{dt} \tag{2.54}$$

wherein Equation (2.54) the subscript r refers to the reference and s refers to the sample. The thermal resistance R and heat capacity C in Equation (2.54) are for the respective sensor, and ΔT_o is difference in temperature from the control to the sample. Equation (2.53) however, shows the fundamental principle; that a temperature difference between the sample temperature T_s and reference temperature T_r causes a heat flow through the thermoelectric disk with thermal resistance R.

Equation (2.53) contains the heat flow, but this equation can be in an equivalent form demonstrating the relationship between heat rate *dT/dt*, sample heat capacity $C_{p,s}$ and reference heat capacity $C_{p,r}$ to the temperature difference ΔT and thermal resistance R [9]:

$$\frac{dT}{dt}(C_{p,s} - C_{p,r}) = \frac{\Delta T}{R} \tag{2.55}$$

Equation (2.55) can be used to determine the heat capacity of the sample. The heating rate, temperature difference, and thermal resistance are known, only the two heat capacities are unknown. Thus, two DSC runs are required at different heating rates to determine the sample heat capacity; two equations in two unknowns. For MDSC, two experimental runs would be superfluous since the cyclical addition to the linear heating rate allows the sample's heat capacity to be determined with Fourier analysis and one experimental run. Thus, MDSC experiments can be reported by heat capacity versus temperature for a single experimental run.

Choosing a linear heating rate *dT/dt* for DSC experiments requires a compromise between competing considerations. These considerations include resolution, thermal lag and accuracy. A DSC machine has a finite sampling rate for heat flows. Thus a faster heat ramp will scan a temperature range with fewer samples; and hence, with lower resolution. Furthermore, a faster heat ramp will cause steeper temperature gradients within a sample, resulting in a higher temperature than in the overall sample; thermal lag in the sample. A slower heat ramp will be more favourable to avoid these deleterious effects; however, a slow heat ramp will lower accuracy. With a slow heat ramp, the sample material is effectively annealed, causing an evolution of structure with different concomitant thermal properties. Therefore, a balancing of the heat ramp to accommodate the favourability of a slow heat ramp for resolution and thermal lag, yet a fast enough heat ramp for accuracy is required.

MDSC experiments do not rely on high linear heating ramp rates. The heating rate *dT/dt* as is seen in Equation (2.38) is the sum of the linear heating rate and the cosine term. The cosine term is multiplied by the amplitude and angular frequency, allowing for periodically high heating rates. The overall heating rate is slow; however, thermally reversible properties such as the glass transition temperature are largely independent of heating rates in MDSC [26]. Thus, MDSC accuracy for glass transition temperatures is much less dependent on high heating rates that DSC requires.

2.2 Materials for Dosimetry

Each material type is reviewed in this subsection, as well as each individual sample material for potential applicability to dosimetry. Doping with rare-earth compounds will also be covered in 2.2.2. The material types include glass and crystalline compounds for use in indirect x-ray detection and material types also include semiconductor alloys for direct x-ray detection. Glass is a non-crystalline solid that possesses the property of continuous volume as a function of temperature, including when it undergoes the solid to liquid phase transformation [27]. Glass is formed by quenching a liquid to below its melting temperature at a temperature rate sufficient to disallow kinetically favourable formation of crystalline material [27]. Glass lacks long range atomic ordering; there are no discernable lattice features such as symmetry groups and resulting lattice parameters [28]. Glass properties and composition are also uniform, allowing for isotropy and complex compositions to remain as a single homogeneous phase [28].

Compounds with chemical stoichiometry are susceptible to crystallization, and glasses derived from such compounds are resultantly less stable [28]. Another cause lowering the stability of glass compounds are the metallic nature of certain elements, wherein delocalized electrons characteristic of metals impede the strength of covalent bonding [28]. Overall, the glass stability, including at elevated annealing temperatures, can be characterized by the Hruby coefficient k defined as [27]:

$$k = \frac{T_x - T_g}{T_m - T_x} \tag{2.56}$$

where T_m is the melting onset temperature, T_x is the crystallization onset temperature, and T_g is the glass transition temperature. A glass with a Hruby coefficient of at least 0.7 can be considered stable [27].

2.2.1 Indirect Detection Materials: Bulk Constituents

Glass, crystalline materials, and glass-crystalline materials will be explored in this study to detect x-ray dose indirectly. Oxide glasses of the form A_mO_n where A is the cation and O is the oxygen anion generally follow Zachariasen's four rules [27]:

1. O^{2-} bonds to one or two other atoms only.
2. O^{2-} bonding coordination is either three or four.
3. O^{2-} anions form polyhedral groups about a cation and only one such anion can be shared between two cations.
4. Cation polyhedra have three or more O^{2-} anions shared at corners with surrounding cations.

Oxide glasses have only short range atomic order where local bonding configurations matter most; hence, application of Zachariasen's principles for the ability of forming glass in multi-component glasses is a possible method of describing the structure of oxide glasses. Thus, such material systems which follow the four aforementioned rules should be more capable of forming a glass, and less likely to crystallize. According to [15], such a multi component glass can be formed through crosslinked P_2O_5 and B_2O_5. The BO_4 and PO_4 tetrahedral units link at the oxygen corners to produce such a structure [29].

Another method of determining of capability of a material system to forming is by "Sun's Single Bond Strength Criterion" [27]. The cation-anion bond strength is considered and its strength determines the capability to form glass. Single bond strengths of important cations in oxide compounds and their glass forming ability for this study are summarized in Table 2.2. Glass forming cations most easily form glass, intermediates less so, and glass modifiers usually impede glass formation.

Table 2.2 Single bond strengths of glass forming, intermediate, and glass modifying cations in oxide compounds. (Data is after [27])

Cation	Single Bond Strength (kJ)	Cation Type
Al, four-fold coordination	331 to 423	Glass Former
Al, six-fold coordination	222 to 280	Intermediate

B	498	Glass Former
Ba	138	Glass Modifier
Na	84	Glass Modifier
P	368 to 464	Glass Former
Sn	192	Glass Modifier
Si	444	Glass Former

Glass modifiers act in a phosphate glass material by way of inhibiting glass chain polymerization with non-bridging oxygen [30]. These extra oxygen anions terminate polymer chains by acting as chain ends. For borate glass, an opposite effect occurs where modifier oxides increase crosslinking with BO_3 structural units becoming BO_4 units instead [30]. Thus, in a material containing modifier oxides, the addition of B_2O_3 of up to about 30 mol% in lieu of P_2O_5 will increase the glass transition temperature and thermal stability [30], which indicates greater cross linking and polymerization of the glass structure.

2.2.2 Rare Earth Doping of Materials

In this work, the effect of rare earth doping is explored. Rare earth doping in ceramic compounds allow the material to become capable of light absorption and fluorescence [31]. Forbidden transitions occur in rare earth dopants due to the mixing of 5d and 4f states [12]. Rare earth ions in turn can be used in electron charge transfer and probed using f-d transitions [32]. Charge transferred to an ion reduces it. This is an electronic process which can be harnessed for indirect conversion detectors. The energy levels associated with trivalent rare earth ions doped in $LaCl_3$ are given in [31]. The energy quanta of transitions of Sm^{3+} in $LaCl_3$ were used to estimate the corresponding photon wavelengths that will be fluoresced or absorb light in Sm doped materials. Below in Table 2.3, the important PL and XL transitions associated with each ion are summarized. Vacuum UV and 400 nm light have been shown to produce PL emission spectra associated with Sm ions in $SrBPO_5$ materials [33]. The excitation spectrum for the Sm^{2+} state in $BaBPO_5$ has been shown to demonstrate considerable luminescence for the ^5D_o to ^7F_o transition [29]. Thus, Sm3+ reduction to Sm2+ may potentially enable indirect conversion detectors

through changes in the relative populations of the two Sm ion valences. As Sm cations are reduced from the 3+ to 2+ oxidation state, the doped material exhibits changed luminescence spectra, indicating indirect conversion has occurred.

Table 2.3 Energies associated with important transitions.

Ion	Ground State	Excited State	Approximate photon wavelengths associated with the energy of transition (cm^{-1}, nm)		Comments
Sm^{3+}	$^6H_{5/2}$	$^4G_{5/2}$	17700	564	Estimated using [31]
Sm^{3+}	$^6H_{7/2}$	$^4G_{5/2}$	16700	600	Estimated using [31]
Sm^{3+}	$^6H_{9/2}$	$^4G_{5/2}$	15500	645	Estimated using [31]
Sm^{3+}	$^6H_{11/2}$	$^4G_{5/2}$	14100	710	Estimated using [31]
Sm^{2+}	^7F_o	^5D_o	14600	683	Corresponds to 680nm peak in [29]

Different cationic sites in a host material can influence the energies associated with the forbidden transitions of Sm cations. Sm^{2+} doping can cause a $BaBPO_5$ material to have Ba^{2+} to be substituted with the dopant cation, revealed in low temperature studies by the ^7F_o to ^5D_o transition [29].

2.2.3 X-ray Irradiation of Glass and Ceramic Materials

When a glass or ceramic material is x-ray irradiated, different electronic processes may occur, altering the material. The dopant Sm can convert in materials from Sm^{3+} valency to Sm^{2+} state with x-ray irradiation when doped in some materials [29]. The chemical equation for samarium valency conversion is thus: $Sm^{3+} + e^- \rightarrow Sm^{2+}$. The Sm^{2+} state in $BaBPO_5$ is metastable up to a certain temperature between 250 °C and 450 °C [29]. Thus, room temperature stability of the Sm^{2+} is at least present in doped $BaBPO_5$ materials, thereby enabling the material to act as an x-ray storage phosphor [29]. Another x-ray irradiation effect that is important in this work is photodarkening; the PL and XL intensities may diminish with irradiation time.

3 EXPERIMENTAL APPARATUS, METHODOLOGY AND PROCEDURES

The processing steps, materials, equipment and methods in this study will be established in this chapter. Material synthesis is first covered. The materials included in this study are: $BaBPO_5$:Sm_2O_3, $BaBPO_5$:(Sm_2O_3,$ErCl_3$), $BaBPO_5$:SmF_3, SiO_2-Al_2O_3-B_2O_3-Na_2O-SnO_2:Sm_2O_3, BaF_2-B_2O_3-$Na_4P_2O_7$:SmF_3, and BaF_2-B_2O_3-$Na_4P_2O_7$:Sm_2O_3. Characterization techniques are covered next, followed by thermal analysis techniques.

3.1 Synthesis of Samples

The synthesis of samples and subsequent processing steps are explained for each material below. All sample reagents were measured on a Mettler BasBal model BB600 scale. Generally, all material processing involved melt quenching to produce glass or glass-ceramics. All hot quenched samples were quenched on a steel block estimated at 250 °C. This temperature was initially thought to be between 150 °C and 180 °C according to Omega 871A Digital Thermometer. The steel block temperature was maintained on top a Thermolyne type 1900 hot plate. Room temperature quenched samples were quenched on a room temperature steel surface. For all samples, the melt was produced by heating reagents in a high form alumina crucible from Coorstek and by heating in a Hot Spot 110 Furnace from Zircar Zirconia, Inc. The temperature was brought gradually to the reported temperatures by ramping. From room temperature, the furnace was brought to 50 °C below the target temperature in 30 minutes. Then, for the remaining 50 °C from the target temperature, the temperature was ramped to the target temperature in 10 minutes. The actual temperature measured by the temperature controller varied usually up to 30 °C to 50 °C above the target temperature. Subsequent annealing was carried out in this furnace and also in a CMF1100 furnace from MTI Corp. Both furnaces were kept within a ventilated fume hood.

The Zircar Hot Spot 110 furnace is shown in Figure 3.1. The furnace had two temperature controllers: a heat program controller and an over temperature protection controller. Another furnace was used additionally for annealing only. The alternative furnace for annealing was the CMF1100 furnace from MTI Corporation, pictured in Figure 3.2. For annealing with the CMF 1100 furnace, the temperature was set directly to the desired temperature with the sample placed inside at room temperature prior to furnace operation. The exception to these annealing furnaces is for samples annealed at 250 °C which was completed on the 250 °C steel block.

The general step-by-step process of solid state reaction, melt quenching or annealing in the furnace was,

1. Insert ground and mixed chemical reagents. Leave crucible partially or completely uncovered by lid. Close securely furnace door.
2. Set program temperature controller. The temperature programs were,
    a. For the Hot Spot 110 furnace: Heat sample from room temperature to a temperature 50 °C less than the target temperature. The time interval of this step is 30 minutes. Then, for the last 50 °C: heat crucible to target temperature over 10 minutes.
    b. For the CMF 1100 furnace: Set to target temperature directly.
3. Keep furnace at target temperature for a duration in hours.
4. Then,
    a. If solid state reaction or annealing, close furnace at end of the duration of Step 3. Let sample material slowly cool in the furnace.
    b. If melt quenching, maintain furnace temperature and remove lid if applicable with tongs. Use metal tongs to remove crucible from furnace and over turn crucible and empty melt contents on metal surface. For hot quenching, pour melt on hot steel block. If room temperature cold quenching, use room temperature steel surface.

Select synthesized materials were photographed to show visually features. Some of these materials include the annealed samples.

Figure 3.1 The Zircar Hot Spot 110 Furnace used for melt-quenching synthesis.

Figure 3.2 The CMF1100 Furnace by MTI Corp.

3.1.1 $BaBPO_5$ doped with 1mol% Sm_2O_3

This material synthesis steps were similar to that found in [29]. The Ba^{2+} cations in this material act as modifiers. The tetrahedral Borate and Phosphate units would be increase the tendency towards glass formation. Samarium oxide would contribute Sm^{3+} cations to the material. The structure of the material due to the addition of Ba cations would allow Sm cations to occupy vacant Ba sites [29].

The masses were added stoichiometrically with a 3 mol% excess for H_3BO_3 and 5 mol% excess for $(NH_4)_2HPO_4$. The masses of reagents were as follows:

Mass ($BaCO_3$) = 10.2 g

Mass (H_3BO_3) = 3.3 g

Mass ($(NH_4)_2HPO_4$ = 7.0 g

Mass (Total) = 20.5 g

The crucible was placed with a partially closed lid into a furnace initially at room temperature. The furnace was ramped from room temperature to 550 °C in 30 minutes and then ramped from 550 °C to 600 °C in 10 minutes. These chemicals were kept at 600 °C for 2 hours to evaporate carbon dioxide, water vapour and ammonia according to the solid reaction formula:

$$BaCO_{3\,(s)} + H_3BO_{3\,(s)} + (NH_4)_2HPO_{4\,(s)} \rightarrow BaBPO_{5\,(s)} + CO_{2\,(g)} + 3\,H_2O_{\,(g)} + 2\,NH_{3\,(g)}$$

After the two hour duration, the powder material was allowed to cool to room temperature. The crucible was removed after it cooled and the dopant was added. The dopant Sm_2O_3 was used to dope. The mass of dopant was,

Mass (Sm_2O_3) = 0.2 g

Using a mortar and pestle, the precursor host material was ground. The precursor host material appeared as in Figure 3.3. Again, with a mortar and pestle, the dopant was mixed with the $BaBPO_5$ and subsequently melted at 975 °C. It was removed after 6 hours at 975 °C and the melt was quenched. The crucible lid was removed while in the furnace, and the crucible was then

removed from the furnace and overturned onto the steel block. The melt did not appear to flow and was likely still solid. It solidified in the crucible.

The following calculations of moles are for the chemical reagents,

Moles (Sm_2O_3) = 0.2 g / 348.8 g/mol = 5.734e-4 mol

Moles ($BaCO_3$) = 10.2 g / 197.34 g/mol = 5.169e-2 mol

Moles ($BaBPO_5$) = Moles ($BaCO_3$) = 5.169e-2 mol

Thus, the doping concentration which was,

= 5.734e-4 mol Sm_2O_3/ (5.734e-4 mol Sm_2O_3 + 5.169e-2 mol $BaBPO_5$)

≈ 1 mol% Sm_2O_3

Figure 3.3 Photograph of $BaBPO_5$ powder in crucible, after solid state reaction, and regrinding, but prior to the addition of dopant.

This sample was not subsequently annealed. It had already appeared partially crystallized. One side of this sample was translucent and deemed likely to be composed predominantly of glass. This side was in contact with the sides of crucible. The other side appeared opaque without surface lustre and was probably composed predominantly of crystals. The opaque side was on the open top surface of the crucible.

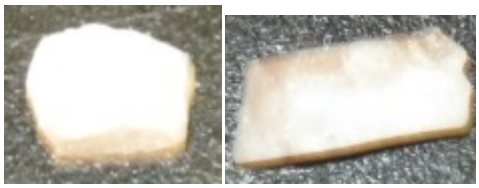

Figure 3.4 Photograph of non-irradiated $BaBPO_5:Sm_2O_3$ on left and irradiated $BaBPO_5:Sm_2O_3$ on right.

The synthesized sample before and after x-ray irradiation is shown in Figure 3.4. Both samples are shown to have contained two visually distinct phase regions. One of these regions was translucent, indicating predominantly a glass phase was present. It is seen as the light purple lower portion in the non-irradiated sample. For the irradiated sample, the glass phase appeared slightly darkened as seen on the top region of that sample. For opaque region, the sample was likely composed mostly of crystals. It appears white in the photographic images, with the irradiated sample slightly darkened visually.

3.1.2 $BaBPO_5$ doped with 1 mol% Sm_2O_3 and $ErCl_3$

This sample is similar to the preceding sample, except for the addition of co-dopant $ErCl_3$. Sm_2O_3 was used to dope and $ErCl_3$ was a co-dopant. The intention is to determine if Er ion codoping improves Sm conversion. The solid-state reaction was done at 500 °C for 5 hours instead of 2 hours at 600 °C. Furthermore, the melting procedure was first at 975 °C for 5 hours, producing crystals and then, to produce glass, was heated to 1300 °C for 30 minutes and then quenched on a hot plate. The dopant mass was,

$Mass(Sm_2O_3) = 0.2$ g

The codopant mass was,

Mass($ErCl_3$) = 0.3 g

The moles were calculated,

Moles (Sm_2O_3) = 0.2 g / 348.8 g/mol = 5.734e-4 mol

Moles ($ErCl_3$) = 0.3 g / 273.62 g/mol = 1.0964e-3 mol

Moles ($BaBPO_5$) = Moles ($BaCO_3$) = 5.169e-2 mol

The doping and codoping levels were therefore:

Co-doping level in mol% = 1.0964e-3 mol / (1.0964e-3 mol + 5.734e-4 mol + 5.169e-2 mol)

= 2.0552e-2 ≈ 2 mol% $ErCl_3$

Doping level in mol% = 5.734e-4 mol / (1.0964e-3 mol + 5.734e-4 mol + 5.169e-2 mol)

= 1.0746e-2 ≈ 1 mol% Sm_2O_3

This material was not subsequently annealed. Its bulk appeared glass-like and homogeneous when visually inspected. The atmosphere exposed surface side was slightly translucent. The bulk appeared to be mostly transparent with some translucence in the middle wedge as seen in Figure 3.5.

Figure 3.5 Photograph of $BaBPO_5$:(Sm_2O_3,$ErCl_3$), non-annealed, non-irradiated.

3.1.3 SiO_2-Al_2O_3-B_2O_3-Na_2O-SnO_2 doped with 1wt% Sm_2O_3

The composition and synthesis method for the Sm_2O_3 doped SiO_2-Al_2O_3-B_2O_3-Na_2O-SnO_2 material was similar to that which was reported in [34]. The furnace was initially heated to 500 °C for 5 hours. Then, the sample was heated to 1500 °C for 14 hours. The sample was taken out with tongs at 1500 °C but pouring on the hot plate for quenching was not possible due to the high viscosity of the melt. The sample was extracted manually from the crucible and then annealed at 600 °C for the removal of thermal stresses.

The host material was composed of approximately equal molar ratios of SiO_2, Al_2O_3, B_2O_3, Na_2O, SnO_2 reagents. The masses of reagents are as follows:

Mass (SiO_2) = 23.7 g

Mass (Al_2O_3) = 2.6 g

Mass (B_2O_3) = 7.3 g

Mass (Na_2CO_3) = 5.2 g

Mass (SnO_2) = 1.8 g

Mass (Total) = 40.6 g

After heating, Na_2CO_3 should decompose with the carbon dioxide being sublimated and removed. The chemical equation would be then

$$Na_2CO_{3(s)} \rightarrow Na_2O_{(s)} + CO_{3(g)}$$

The resulting masses are:

Mass (SiO_2) = 23.7 g unchanged

Mass (Al_2O_3) = 2.6 g unchanged

Mass (B_2O_3) = 7.3 g unchanged

Mass (Na_2O) = [(5.2 g)/(106 g/mol)]*(62 g/mol) = 3.04 g calculated

Mass (SnO_2) = 1.8 g

Mass (Total, after carbon dioxide removal) = 38.44 g calculated

Sm_2O_3 was used to dope. Mass(Sm_2O_3) = 0.4 g

The doping concentration was = 0.4 g Sm_2O_3 / (0.4 g Sm_2O_3 + 38.44 g total)

= 0.0103 ≈ 1 wt% Sm_2O_3

The weight percent for the bulk components are then,

Wt% SiO_2 = 23.7g/(0.4g Sm_2O_3 + 38.44g total) = 61 wt%

Wt% Al_2O_3 = 2.6g/(0.4g Sm_2O_3 + 38.44g total) = 6.7 wt%

Wt% B_2O_3 = 7.3g/(0.4g Sm_2O_3 + 38.44g total) = 18.8 wt%

Wt% Na_2O = 3.04g/(0.4g Sm_2O_3 + 38.44g total) = 7.8 wt%

Wt% SnO_2 = 1.8g/(0.4g Sm_2O_3 + 38.44g total) = 4.6 wt%

Wt% total ≈ 100 wt%

Figure 3.6 A photographic image of the non-annealed, non-irradiated SiO_2-Al_2O_3-B_2O_3-Na_2O-SnO_2:Sm_2O_3 material.

This sample was not annealed. The non-annealed material was assayed for experimental analysis. In Figure 3.6 the material is pictured. There were visible air bubbles within the glass material. The top-left corner of material is seen to be transparent, but progressively translucent to the lower-left corner. This translucent corner was thicker, perhaps accounting for the decreased transparency.

3.1.4 BaF_2-B_2O_3-$Na_4P_2O_7$ doped with 0.33wt% SmF_3

This sample is similar to the $BaBPO_5$ materials with only Sm doping. The significance of this material is in its addition of F and Na ions. Fluoride anions would add ionic character to the material, and Na cations would act as glass modifiers. Also, the reagents were directly heated to 950 °C, since there were no gases that would evolve during reaction. The furnace temperature controller displayed the temperature to be close to 1000 °C. Some sample was annealed for 5 hours at 600 °C. The masses of reagents were as follows,

Mass (B_2O_3) = 4.1 g

Mass (BaF_2) = 10.3 g

Mass ($Na_4P_2O_7$) = 15.7 g

Mass (Total) = 30.1 g

The mass of dopant was,

Mass (SmF_3) = 0.1 g

Thus, the dopant weight percent was calculated to be:

Dopant wt% SmF_3 = 0.1 g SmF_3 / (0.1 g SmF_3 + 30.1 g total)

= 3.31e-3 ≈ 0.33 wt% SmF_3

The melt quenched material produced on the hot steel block appeared as mostly glass. The surface was partially covered in opaque crystals. Some hot quenched material was annealed on the hot steel block. This material was annealed over 24 hours and is seen in Figure 3.7. A glass-ceramic mixed phase material is evident from visual inspection on the atmosphere exposed surface during quenching. The crystals were formed during melt quenching. Some other hot quenched material was annealed at 600 °C for 20 hours. This 600 °C annealed material is compared to the non-annealed material in Figure 3.8.

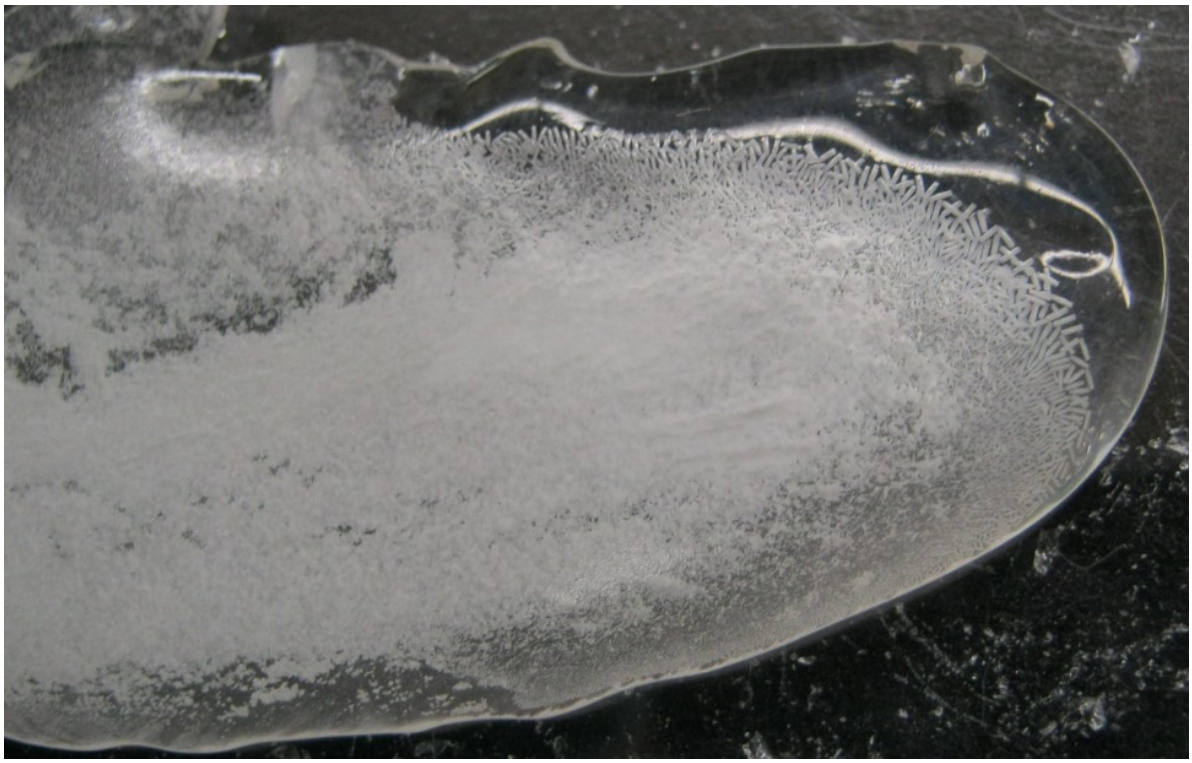

Figure 3.7 BaF_2-B_2O_3-$Na_4P_2O_7$:SmF_3 annealed on the hot plate for 24 hours.


(a)

(b)

Figure 3.8 BaF_2-B_2O_3-$Na_4P_2O_7$:SmF_3 a) annealed in furnace at 600 °C for 20 hours from hot quenched precursor material. b) non-annealed, hot quenched material.

3.1.5 BaF_2-B_2O_3-$Na_4P_2O_7$ doped with 0.33wt% Sm_2O_3

This material was similar to the previous material; however, instead of SmF_3, the dopant was Sm_2O_3. The furnace was kept at a temperature close to 1000 °C. The oxide dopant would add a slightly larger amount of O atoms, relative to F atoms. The reagents were weighed on a Mettler scale. The masses were,

Mass (B_2O_3) = 4.1 g

Mass (BaF_2) = 10.3 g

Mass ($Na_4P_2O_7$) = 15.7 g

Mass (Total) = 30.1 g

The mass of dopant added was 0.1 g. The doping level was calculated in weight percent:

Dopant wt% Sm_2O_3 = 0.1 g Sm_2O_3 / (0.1 g Sm_2O_3 + 30.1 g total) = 0.33 wt% Sm_2O_3

The doped sample material was quenched on the hot steel block or the room temperature steel surface. Then some hot quenched material was subsequently annealed at 600 °C for 6 or 12 hours.

3.2 Characterization of Materials

The spectroscopic methods and equipment on the synthesized materials are covered in this subsection. The spectroscopic techniques employed in this study are: XL and PL, absorption spectroscopy, ESR Spectra, Raman Spectroscopy, and XRD. X-ray irradiation of samples is explained jointly with XL and PL as these methods required and x-ray source to determine spectral changes in the dosimetric materials due to irradiation.

3.2.1 XL, PL and X-ray Irradiation Effects

X-ray irradiation of the dosimetric materials was conducted at the Canadian Light Source Synchrotron for the XL and PL spectra. The x-ray beam profile was: 5 mm in height and 8mm in width. The peak x-ray intensity was approximately 45 keV. The beam was filtered by three copper plates, totalling 0.938 mm in thickness. The samples were located 26 m from the beam entrance into the hutch. The dose rate was estimated at 2 Gy/s. Samples were held by Kapton brand tape. The spectrometer was model EPP2000 from StellarNet Inc. and is shown in Figure 3.9. A fibre optic cable was attached to the spectrometer and threaded into a box containing the sample. The box minimized stray light from external sources. The excitation source for PL assay was a 405 nm laser diode. In front of the fibre optic cable lead within the box was placed a 550 nm long pass filter to further decrease stray light and also scattered 405 nm laser light.

XL spectra were obtained while material samples were irradiated. XL spectra were obtained at about 60 s and 240 s; and for one sample, at 100 s and 200 s. PL spectra were obtained before and after x-ray irradiation. The spectral intensities of the wavelength range of interest were recorded at 0 s and after 300 s irradiation time. The integration time of the spectrometer was set to at least 1000 ms and no greater than 30000 ms, in order to obtain appreciable spectral intensities.

The samples ranged in geometries and were left in pristine state for x-ray irradiation. The purpose of these samples was to determine scintillation and x-ray storage phosphor function with XL and PL respectively. X-ray irradiation effects were assumed to be roughly sample geometry independent. Since the sample was not repositioned before and after x-ray irradiation, and since glass scatters light, PL light captured and counted by the spectrometer was assumed to show accurately the evolution of peaks with x-ray irradiation. Consequently, since XL was recorded in the same wavelength range as PL, the XL spectrum from the sample geometry was also assumed to be sufficient to determine scintillation function.

The XL and PL spectra obtained were analyzed using Microsoft Excel 2007. The baseline was subtracted from each spectrum using the minimum intensity value in the range from 535 nm to 800 nm wavelength. The maximum intensity in the region of the broad 645 nm peak was used to

normalize all other intensities for that spectrum. These two steps were repeated for each spectrum. Normalization of the spectral data was required to remove photodarkening effects. Photodarkening due to irradiation required increasing integration times and also normalizing spectra to allow commensurate PL and XL spectra with irradiation time.

Figure 3.9 The spectrometer that acquired spectral data before, during and after synchrotron x-ray irradiation. It is model EPP2000 from StellarNet Inc.

3.2.2 Absorption Spectral Acquisition

A BaF_2-B_2O_3-$Na_4P_2O_7$ doped with 0.33 wt% Sm_2O_3 sample was cut to a thin, less than 1 mm slice using an Imptech precision cutter with ethylene glycol coolant. A Mastercraft digital calliper measured the thickness to vary between 0.55 mm and 0.58 mm. The sample was then sanded with Silicon Carbide (600 grade) and alumina (0.05 μm), and polished with a Minimet 1000 polisher/grinder by Buehler. Three successively smoother sand papers were used in conjunction with the Minimet 1000 machine and alumina. X-ray irradiation of the sample was performed at the Electronic Materials Research Laboratories, located at the University of Saskatchewan with a Faxitron x-ray cabinet. The x-ray cabinet can be seen in Figure 3.10. Within the x-ray cabinet, a PL/XL reading setup was in place. A 405 nm laser diode was used, which was powered by a model 25-20 power supply from Anatek Electronics, Ltd. The sample was initially assayed for its absorption spectrum prior to x-ray irradiation. The sample was

subsequently irradiated for 1 hour at about 30 kVp and low intensity. Then, it was assayed again for its absorption spectrum. Irradiation took place for an additional hour at about 100 kVp for an hour. The total irradiation time was 2 hours. At that completion of the last hour of irradiation, the absorption spectrum was recorded. The absorption spectrum was recorded using a Lambda 900 UV/VIS/NIR by Perkin Elmer Instruments machine, which was controlled with UV WINLAB computer software. Figure 3.11 shows the inside of the Lambda 900 machine. This figure shows on the top left the reference slit used, and the bottom right slit is where the sample would be assayed from.

Figure 3.10 The X-ray cabinet from Faxitron X-ray Corp.

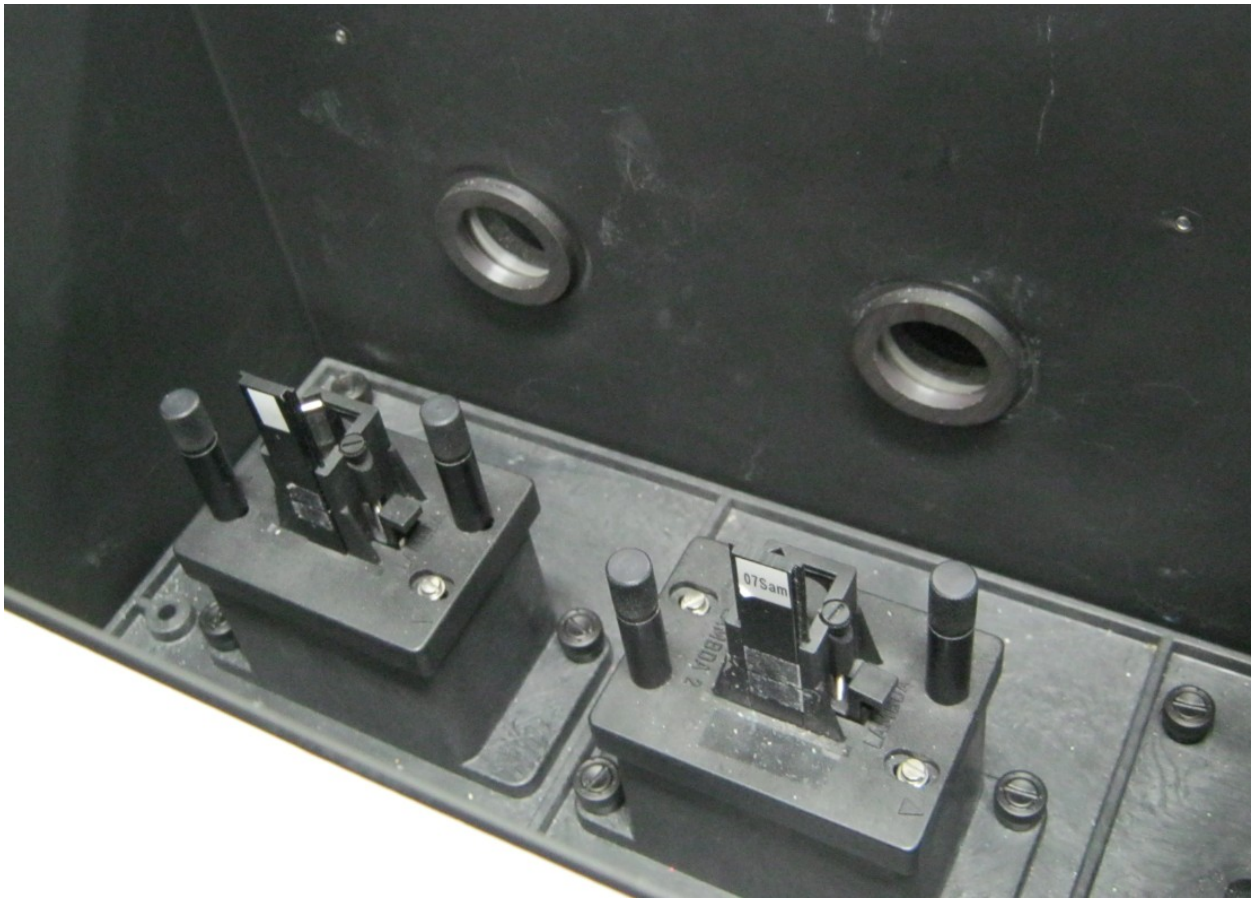

Figure 3.11 Inside the Perkin Elmer Instruments Lambda 900 machine showing the sample and reference slits that are each on a podium. The two holes in the above panel allow incoming light to arrive at the sample slits with focal points on the slit centres.

3.2.3 ESR Spectra

ESR spectra were obtained with a Bruker EMX EPR system. The excitation source was microwave radiation between 9.6 GHz and 9.7 GHz in frequency. The attenuation of the microwave source was 20 dB. The microwave power was at 2.007 W. The resolution was 4096 points over an applied B field range of 3345 G to 3495 G. A quartz tube held the sample material in the ESR cavity. Spectra were obtained of the $BaBPO_5$ doped with 1 mol% Sm_2O_3 sample in the quartz tube and of the quartz tube alone for a control. Both an irradiated sample and non-irradiated sample were assayed. The irradiated sample was exposed to synchrotron x-rays for 20 minutes at 120 Gy per minute; a total x-ray dose of 2400 Gy. Figure 3.12 is a photograph of the

ESR system that was utilized for acquiring ESR spectra. The two large grey cylinders are electromagnets producing the applied B field. The top left unit (shelved over the electromagnets) is the microwave frequency generator with a waveguide flange attached between it and the microwave cavity. The microwave cavity is located between the electromagnets. In front of the ESR system is a temperature controlling device which was not utilized; the experiments were conducted at room temperature. The ESR system was controlled by the computer to the right.

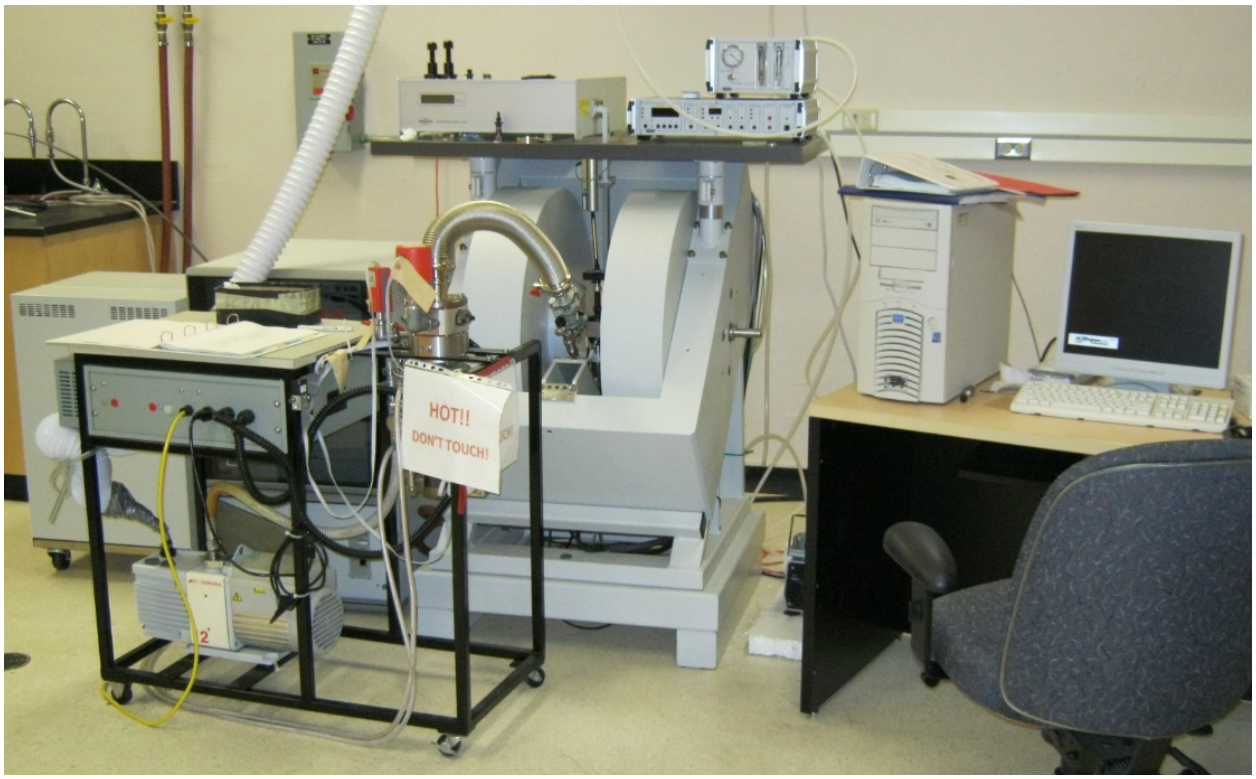

Figure 3.12 A photograph of the Bruker EMX EPR system.

For processing and analysis of ESR spectra, Microsoft Excel 2007 and Renishaw WiRe version 3.3 software programs were utilized. The g-values for peaks were determined with Excel. The quartz tube spectrum was renormalized from resonant frequency 9.660128 GHz to 9.657721 GHz by multiplying abscissa values (applied field B) by ratio of the latter to the former. Renormalization was for peak comparison of the quartz tube spectrum to its signal in the sample data. The ESR data acquired was the first derivative of the intensity, w.r.t. of the applied B field. Thus, the sample spectrum first derivative intensity was numerically integrated. The numerical integration was performed on Excel with the following algorithm,

1. Set intensity at first point to zero, which was at applied B field = 3345 G. $I_{B=3345G}=0$
2. Next point: Take first derivative of intensity at previous point and multiply it by the difference in B field between this point and the previous point. The intensity at this point is this algebraic product summed with the previous point intensity.
3. Repeat step 2 until last point intensity is calculated (B field = 3495 G).

WiRe software automatically curve fit Gaussian and Lorentzian curves to the numerically integrated ESR data. Two Lorentzian peaks were used, corresponding roughly to each of the two distinguishable peaks. In addition, four Gaussian peaks were utilized. The software was run over a hundred iterations for a close curve fit.

The peak values were taken as the nodes of the derivative spectrum. The B field values just prior and just following the node were averaged for the centre peak B field. The peak g-values were calculated using Equation (2.18) and with values for Bohr Magneton and Planck's constant from [35]. The frequency was taken to be 9.657721 GHz for the ESR spectrum of the $BaBPO_5$ sample.

3.2.4 Raman Spectral Acquisition, Processing and Analysis

Raman Spectroscopy was completed with a Renishaw inVia system. The excitation source was a 785nm laser. The attenuation of the laser beam was varied from 1 % to 100 % transmitted in order to obtain a high signal to noise spectrum, yet avoiding spectrometer saturation. The light scattered was collected by a 20x objective lens using non-confocal microscopy. The microscopy setup also was set to record an optical image of each sample. The diffraction grating was 1200 lines per mm. The inVia Raman Microscope system is shown in Figure 3.13. The laser excitation source is located behind the machine. The large compartment on the right contained optics and mechanical components. The sample was placed inside the rotund compartment to the left. The microscope used is partially seen to the top left of the system.

Figure 3.13 A photograph of the Renishaw inVia system used for Raman Spectroscopy and conventional microscopic images.

3.2.5 XRD

XRD experiments were conducted with a TUR M62 diffractometer. The x-ray source was copper K_α radiation with an x-ray wavelength of 0.15405 nm. The 2θ range was from 10° to 60° with a step size of 0.04° each 2.8 s interval. The XRD patterns were analyzed with Powder Cell and Atom software. Structure factors and cell parameter refinement was completed with the Le Bail method using the General Structure Analysis Software. The $BaBPO_5$ sample was not prepared as the aforementioned material above. This doped $BaBPO_5$ material sample, with XRD data, and unit cell are after D. Tonchev, E. Muzar, G. Okada, I. Kostova, Z. Stoeva, G. Patronov, B. Morrell and S.O. Kasap [36]. The Scherrer formula was employed by the author to determine the grain size using the formula as seen in Equation (2.10) with the assumption of infinitesimal

polycrystalline width as mathematically stated in Equation (2.12). Grain size calculations with five labelled peaks were averaged. The standard deviation from the average grain size was also calculated.

3.3 Thermal Analysis

Both DSC and MDSC were utilized for thermal analysis. DSC and MDSC experiments were conducted on a Q100 machine from TA Instruments, Inc. The complete DSC machine is photographed and presented in Figure 3.14. The refrigerator unit was not attached and was not part of the DSC experiments for this study. The top-right of the machine is a touch screen to control the onboard DSC computer. The machine was also able to be controlled from an independent computer system that is not pictured. Also not pictured were the compressed nitrogen gas tank and its regulator that provided nitrogen purge gas. Figure 3.15 is an enlarged view of the swinging robotic arm with the DSC cavity uncovered. The DSC cavity has two aluminium pans visible; one reference and one sample pan. Each pan rests on a podium from which heat is conducted during experimental heating and cooling.

The samples were hermetically sealed in aluminium pans with lids using a mechanical press. The mechanical press and aluminium pans were also from TA instruments. The reference used for the Q100 machine was also a hermetically sealed aluminium pan with a lid. The reference contained no material. The reference and sample aluminium pans were placed in the machine pan-side up. A nitrogen purge gas was pumped at 50 mL/s into the calorimeter cavity. The samples were weighed on a vibration damped concrete table using a Denver Instrument model DI-100 scale. Universal Analysis 2000 software from TA Instruments was utilized in the thermal analysis of data. DSC experiments were run at a ramp rate of 10 °C/min. MDSC experiments were run at a linear ramp of 2 °C/min and a sinusoidal ramp with 60 s period and amplitude of ±1 °C. The upper temperature limit was up to 590 °C for the DSC system due to aluminium pan usage. As such, the temperature scanning limit was kept up to a limit of 590 °C. Sample masses ranged 20 to 25 mg for DSC experiments and 22 to 28 mg for MDSC experiments.

For the materials $BaBPO_5$:Sm_2O_3, and SiO_2-Al_2O_3-B_2O_3-Na_2O-SnO_2:Sm_2O_3, no useful data was to be obtained in the temperature scanning range limit of 590 °C. BaF_2-B_2O_3-$Na_4P_2O_7$:SmF_3, and BaF_2-B_2O_3-$Na_4P_2O_7$:Sm_2O_3 on the other hand were able to be assayed for some important thermodynamic quantities.

Figure 3.14 A photograph of the DSC machine for DSC and MDSC experiments, model DSC Q100 by TA Instruments, Inc.

The Hruby coefficient as seen in Equation (2.56) was utilized to calculated glass stability. The melting points or solidus temperatures were not known for these multi-component glass-ceramics due to limitations from these DSC experiments. Thus, the furnace temperature in the melt quenching procedure replaced the T_m terms for the calculation, which was 950 °C. For dual crystalline phases, the Hruby coefficient was calculated for the lowest crystallization onset temperature phase only. Since only BaF_2-B_2O_3-$Na_4P_2O_7$:SmF_3, and BaF_2-B_2O_3-$Na_4P_2O_7$:Sm_2O_3 were able to be assayed for glass transition temperatures and the first phase crystallization onset temperatures, only these materials had Hruby coefficients calculated.

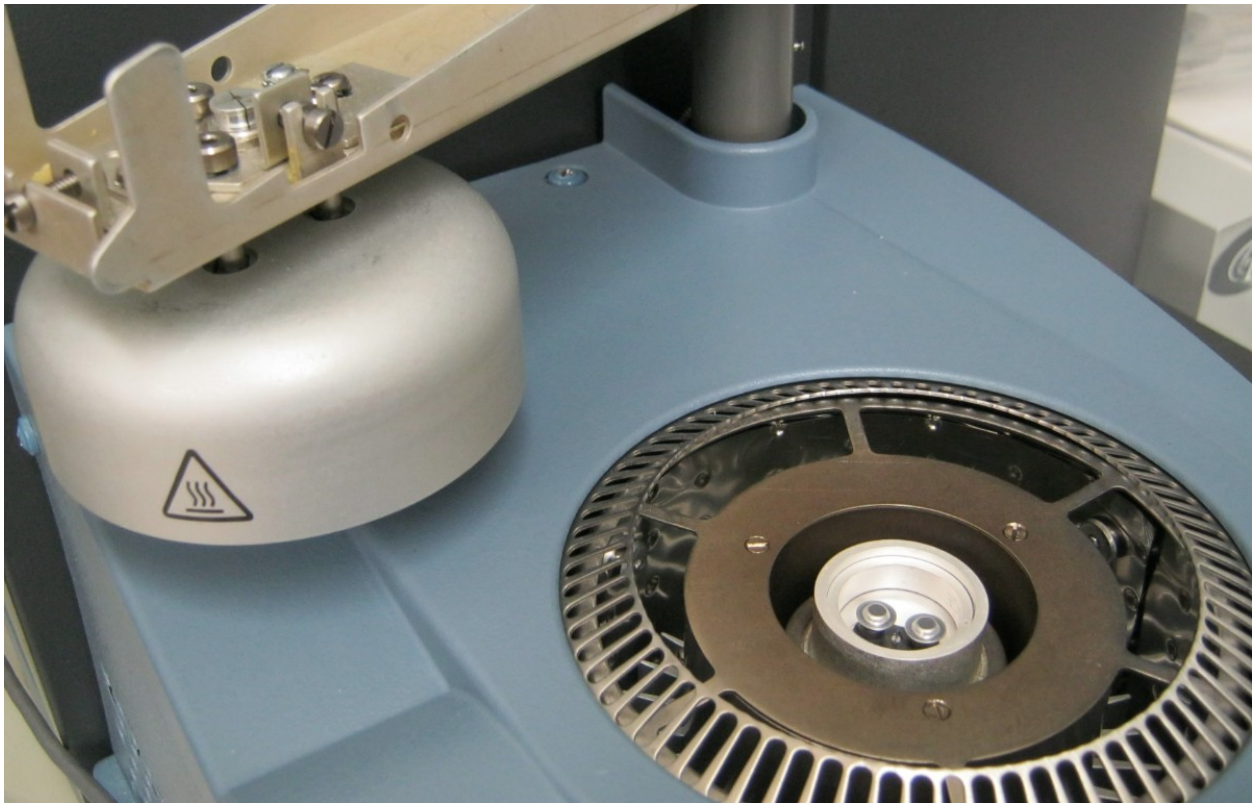

Figure 3.15 The DSC Q100 cavity with top removed, revealing the reference and sample pans.

4 RESULTS AND DISCUSSION

The XL and PL spectra are introduced first for each material. The subsequent sections in order are: absorption spectra, ESR spectra, Raman spectra, XRD and thermal analysis.

4.1 XL and PL spectra of Candidate Materials

The following spectra have been determined for materials before (PL), during (XL), and after (PL) synchrotron x-ray irradiation for 300 seconds. At 2 Gy/s, the total x-ray dose was 600 Gy.

4.1.1 $BaBPO_5$ doped with 1mol% Sm_2O_3

The barium borophosphate material doped with 1 mol% Sm_2O_3 sample exhibits XL and also PL spectra, before and after x-ray irradiation. The XL and PL spectra are shown in Figure 4.1 for the glassy side of the sample and in Figure 4.2 for the crystalline side. For each figure, the graphs on the top-right are a magnification of 670 nm to 730 nm wavelength range from the main graph. Fine structure luminescence features are nearly indiscernible before x-ray irradiation, and appear only after x-ray irradiation. Both crystalline and glass regions of the sample appear to convert Sm^{3+} to Sm^{2+} as is evident from XL peak at 683 nm. Furthermore, PL spectra at the 683 nm peak indicate a large change in intensity after x-ray irradiation. This large PL intensity change shows Sm^{2+} exists in the material after irradiation and that it is likely to be at least metastable in the material with 2+ valency.

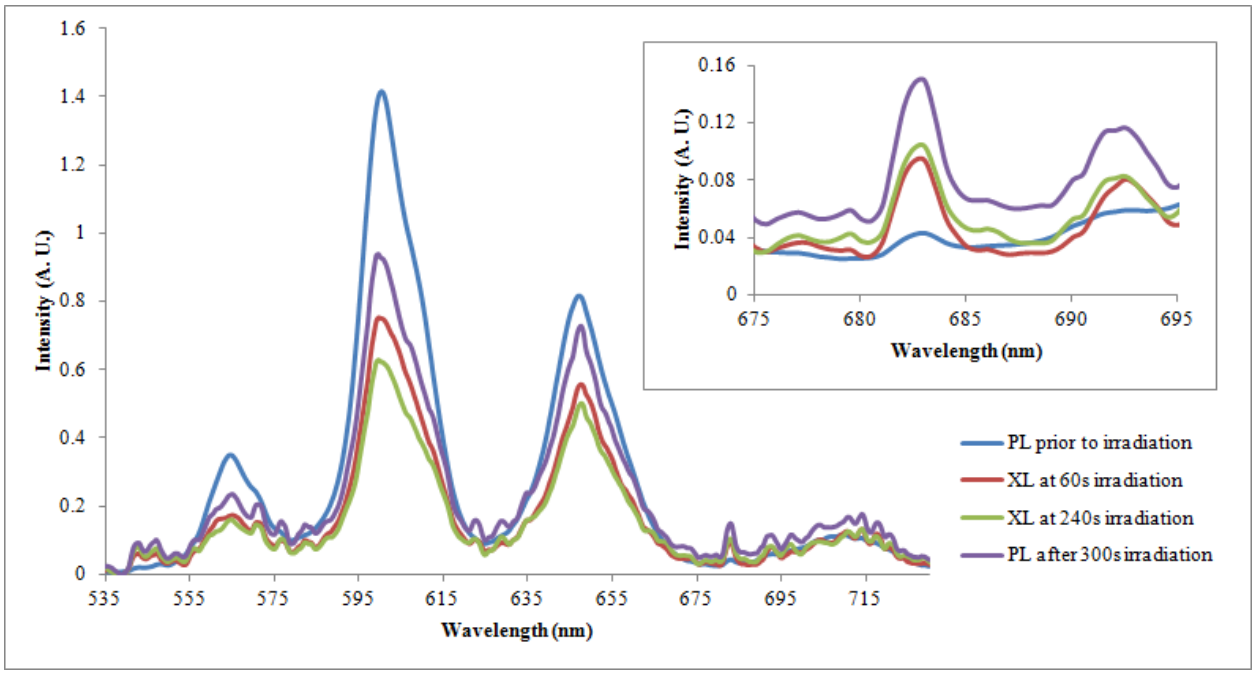

Figure 4.1 PL and XL spectra of Barium Borophospate, 1 mol% Samarium Oxide doped, glass sample side.

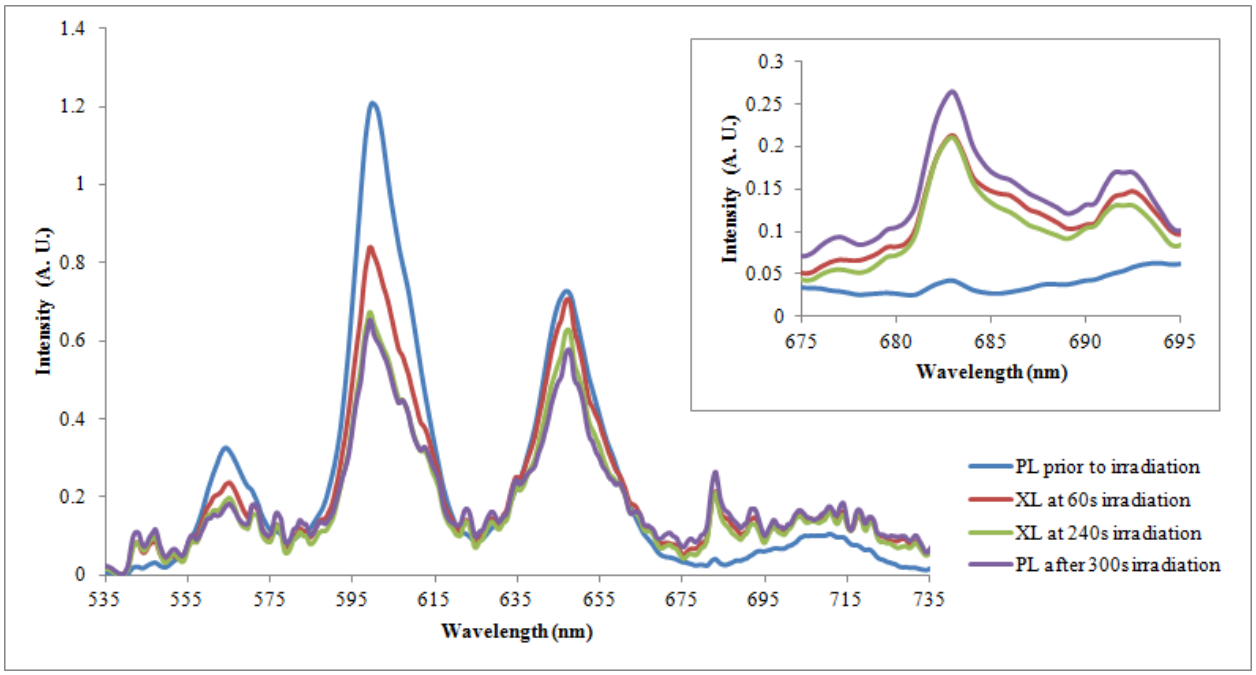

Figure 4.2 PL and XL spectra of Barium Borophospate, 1 mol% Samarium Oxide doped, crystalline sample side.

4.1.2 $BaBPO_5$ doped with 1mol% Sm_2O_3 and codoped with 2mol% $ErCl_3$

The XL and PL spectra of $BaBPO_5$ sample doped with Sm_2O_3 and codoped with $ErCl_3$ are presented in Figure 4.3. From both the PL and XL spectra, it appears that Sm converts to its +2 state and remains in this metastable state. The XL spectra at the 683 nm peak show only a small change in the peak intensity at 683 nm between 60 s and 240 s. The peak at 683 nm indicates a transition involving Sm^{2+} cations. The PL spectra demonstrate a high degree of conversion that persists after x-ray irradiation since the peak located at 683 nm greatly increased after 300 s x-ray irradiation time. The PL before irradiation at 683 nm is less than that without codoping. Also, the PL after irradiation with codoping slightly improved, as well as the XL.

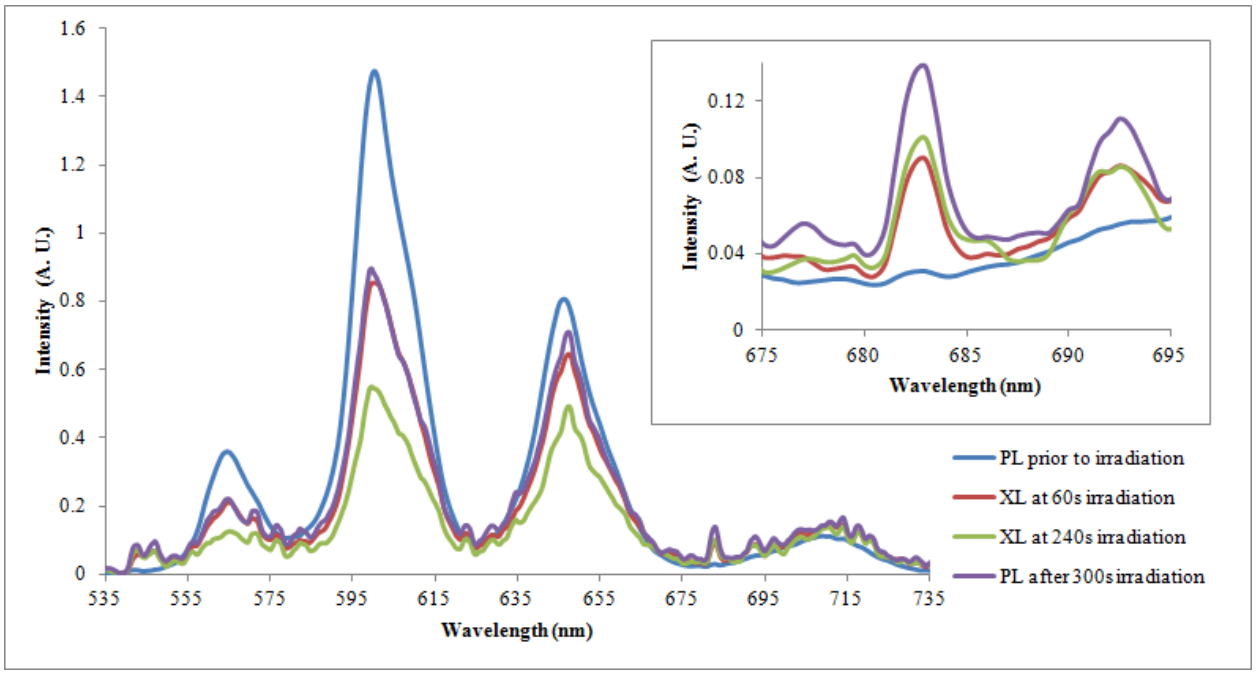

Figure 4.3 PL and XL spectra of $BaBPO_5$ glass-ceramic, doped with 1 mol% Sm_2O_3 and 2 mol% $ErCl_3$.

4.1.3 SiO_2-Al_2O_3-B_2O_3-Na_2O-SnO_2 doped with 1wt% Sm_2O_3

This aluminosilicate glass-ceramic demonstrated XL spectra, but PL spectra to a much lesser intensity at 683 nm. There is considerable XL, but no appreciable PL intensity at 683 nm. The

PL intensity of the 683 nm peak before and after x-ray irradiation is nearly constant. The lack of high PL intensity at 683 nm indicates that Sm^{2+} does not persist in the material after x-ray irradiation. This result is similar to that of sol-gel derived aluminosilicates. In [37], the sol-gel derived aluminosilicate glass showed that Sm^{2+} valency was unstable when generated from electrons captured by Sm^{3+} during x-ray irradiation. Thus, with Sm^{2+} valency induced by x-ray irradiation in such a host material, PL would not occur to a useful extent. The Sm^{2+} cations would be short lived and would revert to the original Sm^{3+} valency. This is further supported by the high intensity XL peak at 683 nm, indicating Sm^{2+} generation during x-ray irradiation. The XL peak remains similar in intensity, which may mean that since Sm^{2+} reverts back to Sm^{3+}, there is near constant population of Sm^{3+} ions that can capture electrons.

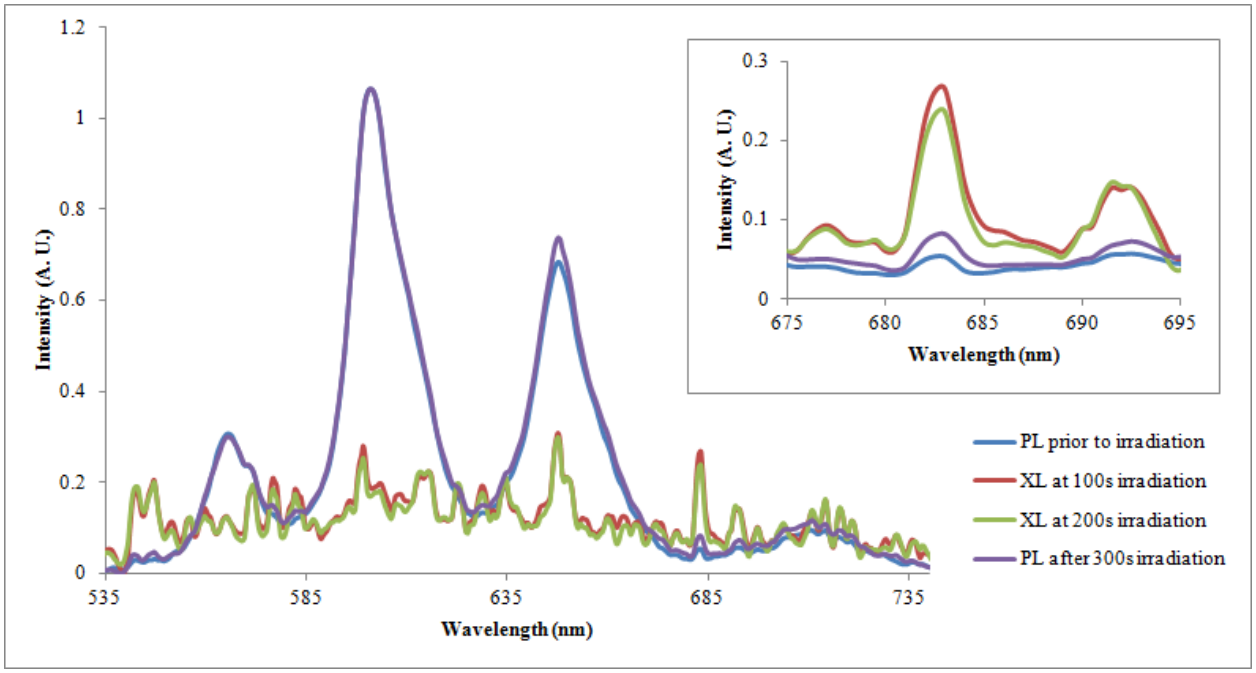

Figure 4.4 PL and XL spectra of SiO_2-Al_2O_3-B_2O_3-$NaCO_3$-SnO_2 doped with 1 wt% Sm_2O_3

4.1.4 BaF_2-B_2O_3-$Na_4P_2O_7$ doped with 0.33wt% SmF_3

The XL and PL spectra of the BaF_2-B_2O_3-$Na_4P_2O_7$ material, doped with 0.33 wt% SmF_3 are shown in Figures 4.5 to 4.8 below. In Figure 4.5, the non-annealed glass-ceramic XL intensity at 683 nm is less than in Figure 4.6 for the non-annealed glass sample. This may mean that the

ceramic crystals may be obscuring luminescence due to opacity. The annealed samples also show a decreased amount of XL intensity at 683 nm, as compared to the non-annealed glass sample. These annealed samples are shown in Figure 4.6 and Figure 4.7. Also, the PL intensity for the 683 nm peak decreased for samples that were annealed. The PL for the 24 hour annealed sample at 300 ºC was lower in intensity for the 683 nm peak after x-ray irradiation than the other samples. Thus, annealing at high temperature, 600 ºC, or no annealing would produce the most effective x-ray storage phosphor. As for scintillation functionality, the non-annealed glass sample was most effective since it possessed the highest intensity for the 683 nm peak associated with Sm^{2+}. A feature of the non-annealed samples was the initial PL intensity at 683 nm was existent. This would imply that a Sm^{2+} existed prior to x-ray irradiation; an ionic state which persisted from the melt after quenching. For the annealed samples however, the peak was negligible with near background intensity. Then, annealing would remove the prior Sm^{2+} population, reconverting the ions to Sm^{3+}. This would mean that the 2+ state is metastable. It is possible that both Sm^{3+} and Sm^{2+} valencies are closer in stability for this host material, relative to the aforementioned host materials. Therefore, these phenomena indicate an excellent host material for samarium conversion scintillators and x-ray storage phosphors.

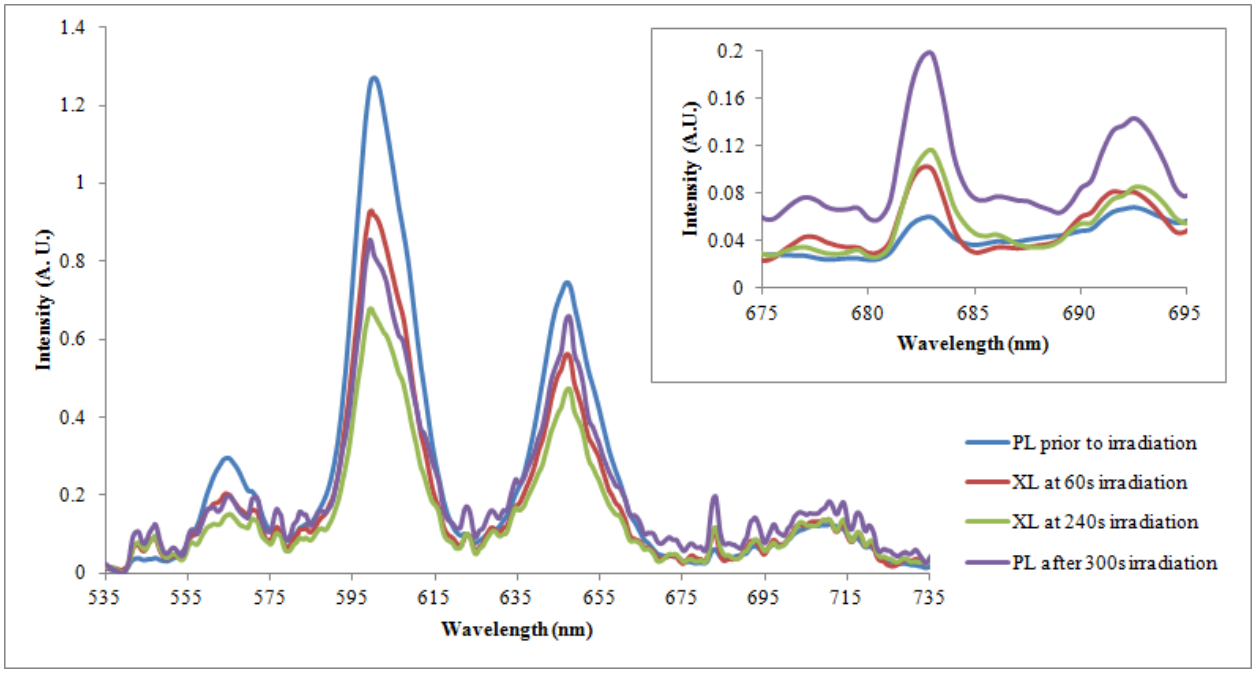

Figure 4.5 PL and XL spectra of BaF_2-B_2O_3-$Na_4P_2O_7$ doped with 0.33 wt% SmF_3, non-annealed glass-ceramic sample

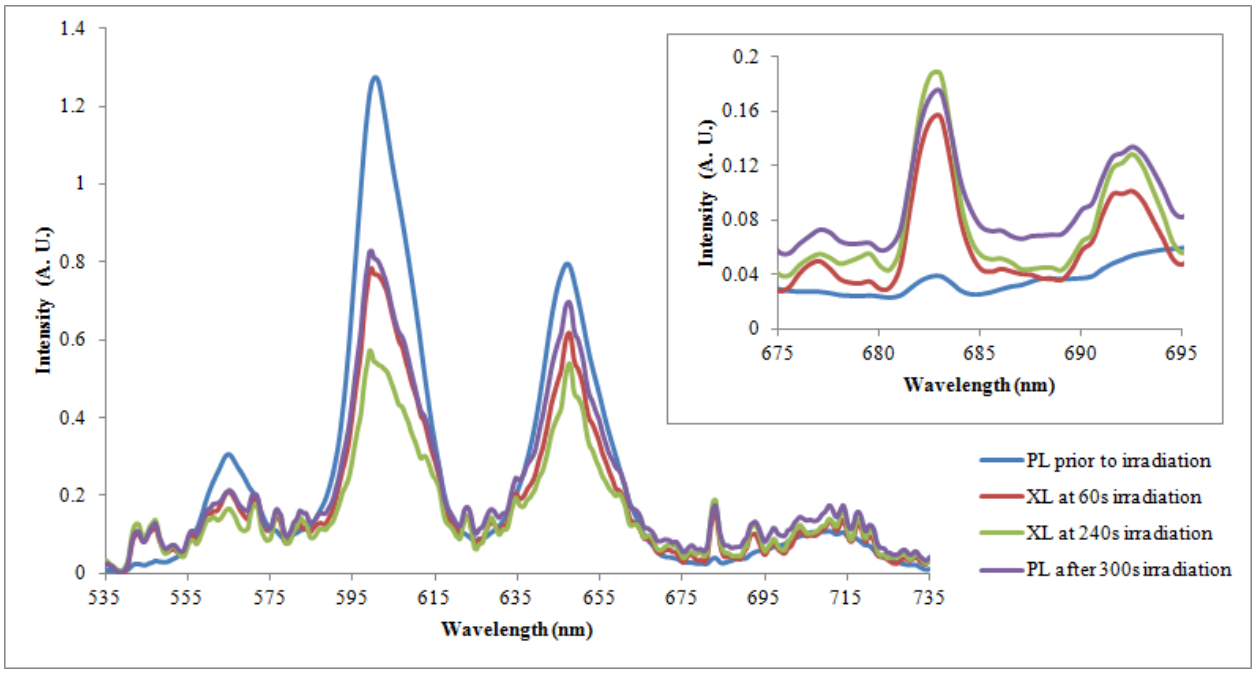

Figure 4.6 PL and XL spectra of BaF_2-B_2O_3-$Na_4P_2O_7$ doped with 0.33 wt% SmF_3, non-annealed glass sample

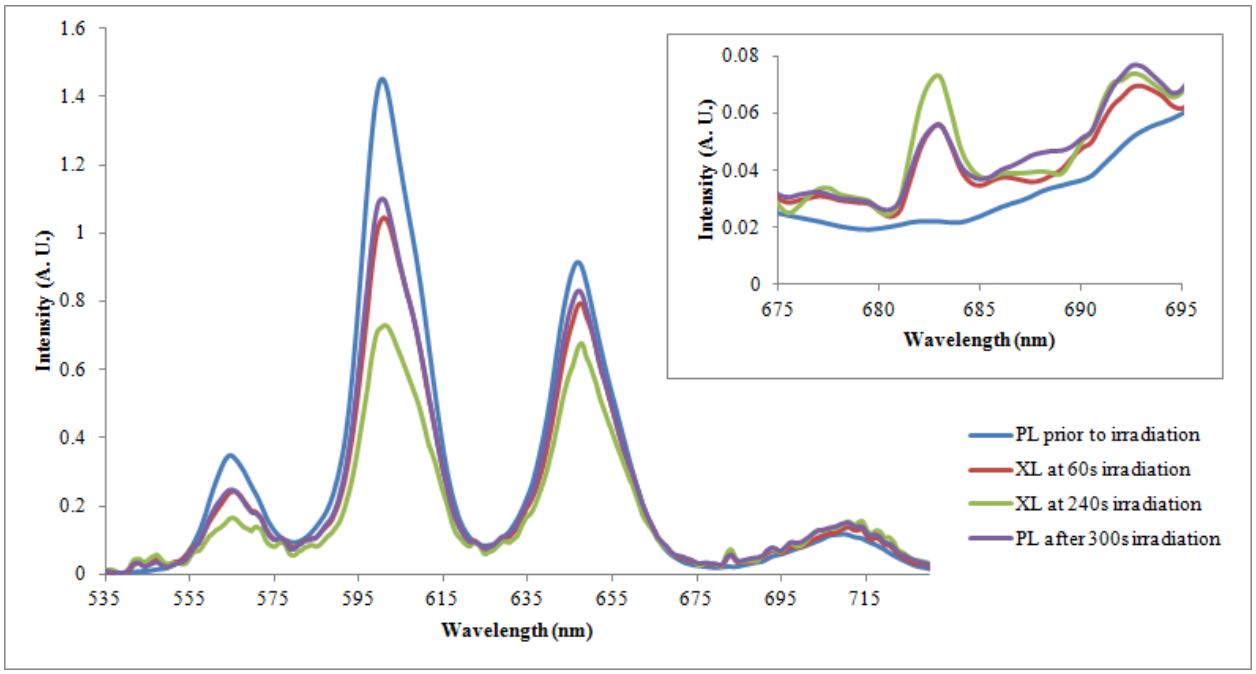

Figure 4.7 PL and XL spectra of BaF_2-B_2O_3-$Na_4P_2O_7$ doped with 0.33 wt% SmF_3 quenched and annealed for 24 h at 250 °C

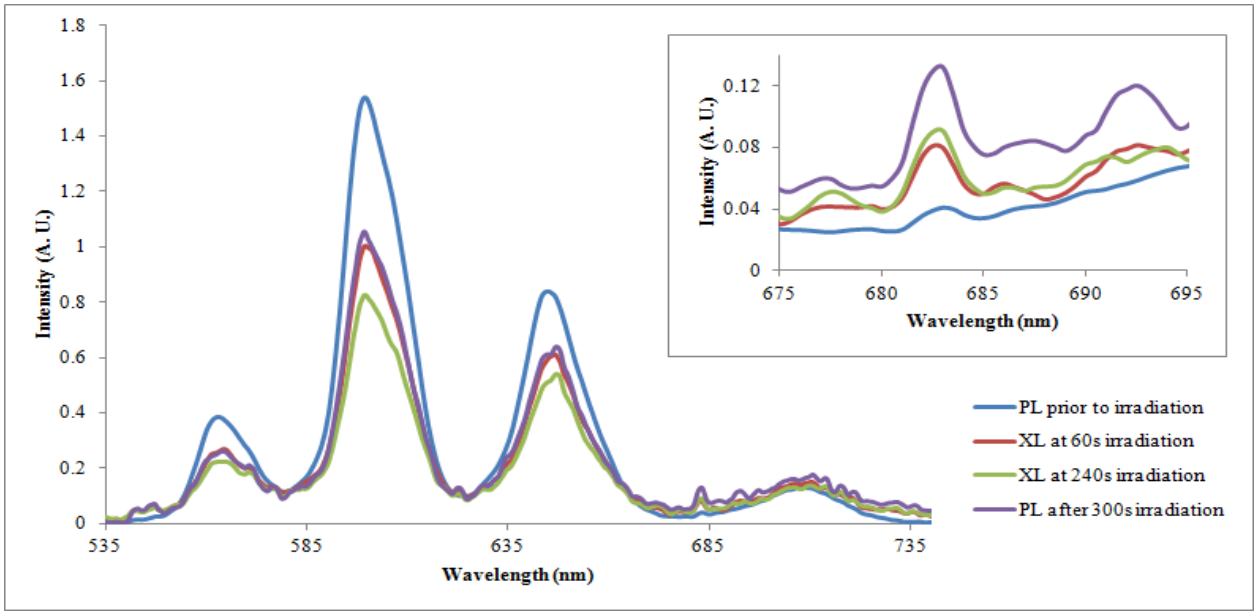

Figure 4.8 PL and XL spectra of BaF_2-B_2O_3-$Na_4P_2O_7$ doped with 0.33 wt% SmF_3 annealed for 20 h at 600 °C

4.1.5 BaF_2-B_2O_3-$Na_4P_2O_7$ doped with 0.33wt% Sm_2O_3

The materials from the BaF_2-B_2O_3-$Na_4P_2O_7$ system doped with 0.33wt% Sm_2O_3 are shown Figures 4.9 to 4.12 below. This material had the greatest intensity for the Sm^{2+} peak at 683 nm when annealed for 12 hours at 600 ºC and least intensity for the non-annealed sample which was hot quenched. These two samples are seen in Figure 4.12 and Figure 4.10, respectively. An intermediate intensity was observed for the 6 hour annealed sample at 600 ºC which is graphed in Figure 4.11. Since these two annealed samples were obtained from the hot quenched sample, it shows an increasing intensity trend with annealing time. Since the 12 hour annealed sample turned from transparent to opaque, it was likely the crystalline phase fraction increased considerably with annealing. Thus, annealing the hot quenched sample improved samarium conversion via the crystalline material more favourably.

Ironically, the non-annealed cold quenched material produced PL intensity comparable to the annealed sample for 12 hours. The cold quenched sample spectra are seen in Figure 4.9 below. A non-annealed sample as seen in Figure 4.9 can, in this case, be an x-ray storage phosphor with high yield, yet maintaining glass-like properties. Although working and forming this glass in a

commercial process at 400 ºC could be possible, it may potentially alter properties. There may be two different factors that may contribute to the cold quenched favourable PL. One, the thermal stresses contribute the PL intensity, in which case annealing would then be not applicable to improving luminescence. The second case is a special high temperature structure permitting a more stable environment for Sm^{2+} ions which remains with the more rapid cold quenching, thereby allowing for improved PL intensity. This second argument is supported by the larger intensity PL peak prior to x-ray irradiation at 683 nm.

XL was observed for all samples during both recorded times during x-ray irradiation. The fine structure for XL and PL after irradiation was very pronounced, especially for the cold quenched, non annealed sample. This was also true but to a slightly less degree for the 12 hour annealed sample. These two samples were also producing the highest PL intensity at 683 nm. Thus, for some reason, the emergence of Sm^{2+} was concomitant with the more pronounced fine structure. This could be that the spin-orbit coupling is altered by the emergence of the Sm^{2+} ion, in contrast to the predominantly Sm^{3+} environment initially.

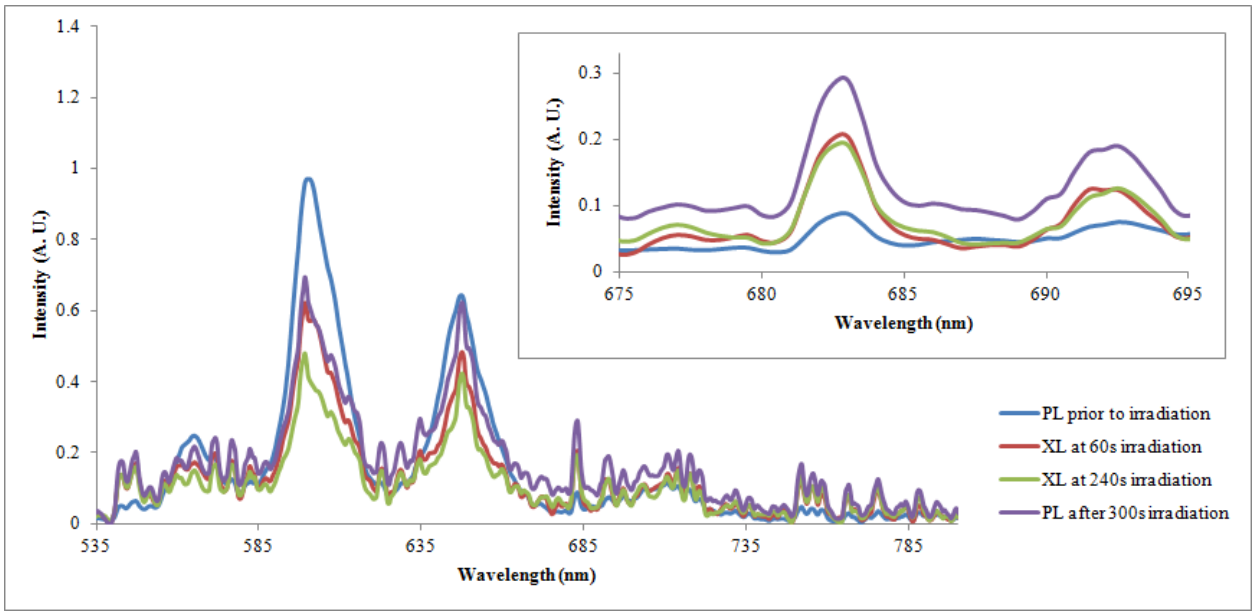

Figure 4.9 PL and XL spectra of BaF_2-B_2O_3-$Na_4P_2O_7$ doped with 0.33 wt% Sm_2O_3 material, quenched to room temperature.

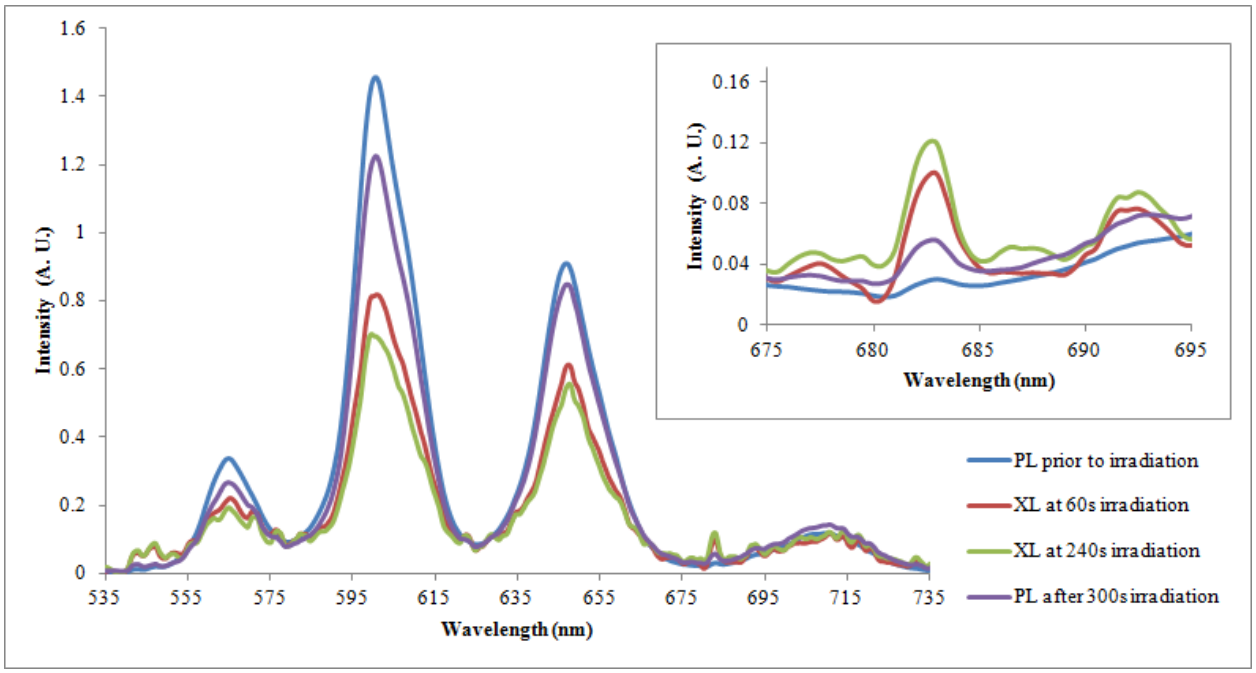

Figure 4.10 PL and XL spectra of BaF_2-B_2O_3-$Na_4P_2O_7$ doped with 0.33 wt% Sm_2O_3 material, quenched to 250 °C.

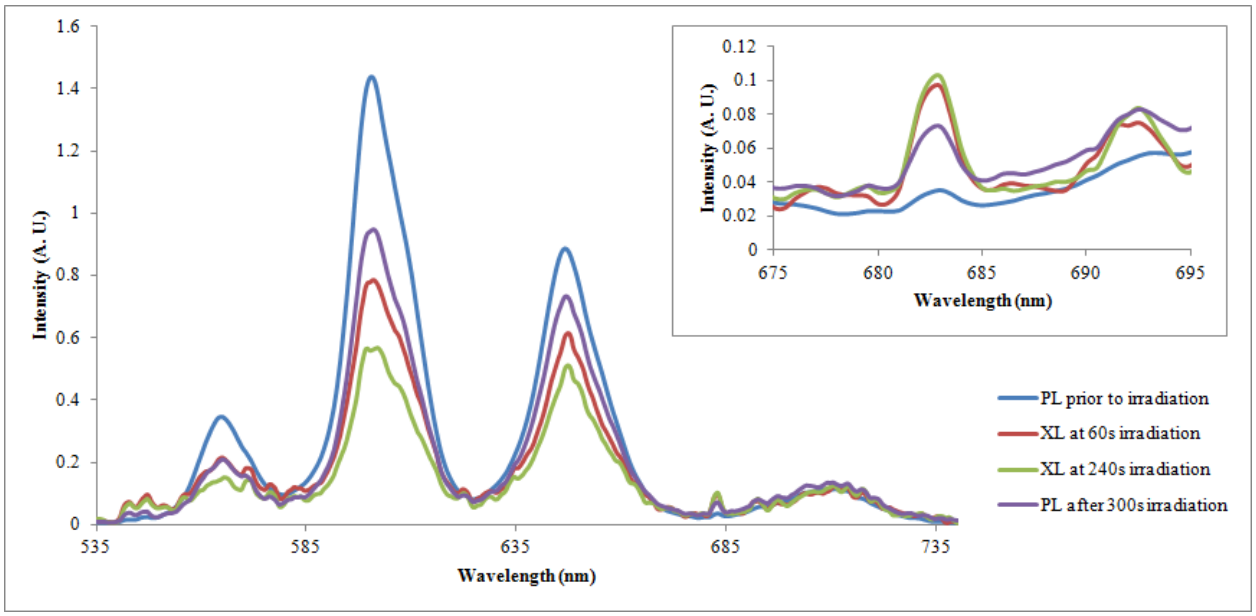

Figure 4.11 PL and XL spectra of BaF_2-B_2O_3-$Na_4P_2O_7$ doped with 0.33 wt% Sm_2O_3 material, annealed at 600 °C for 6 hours.

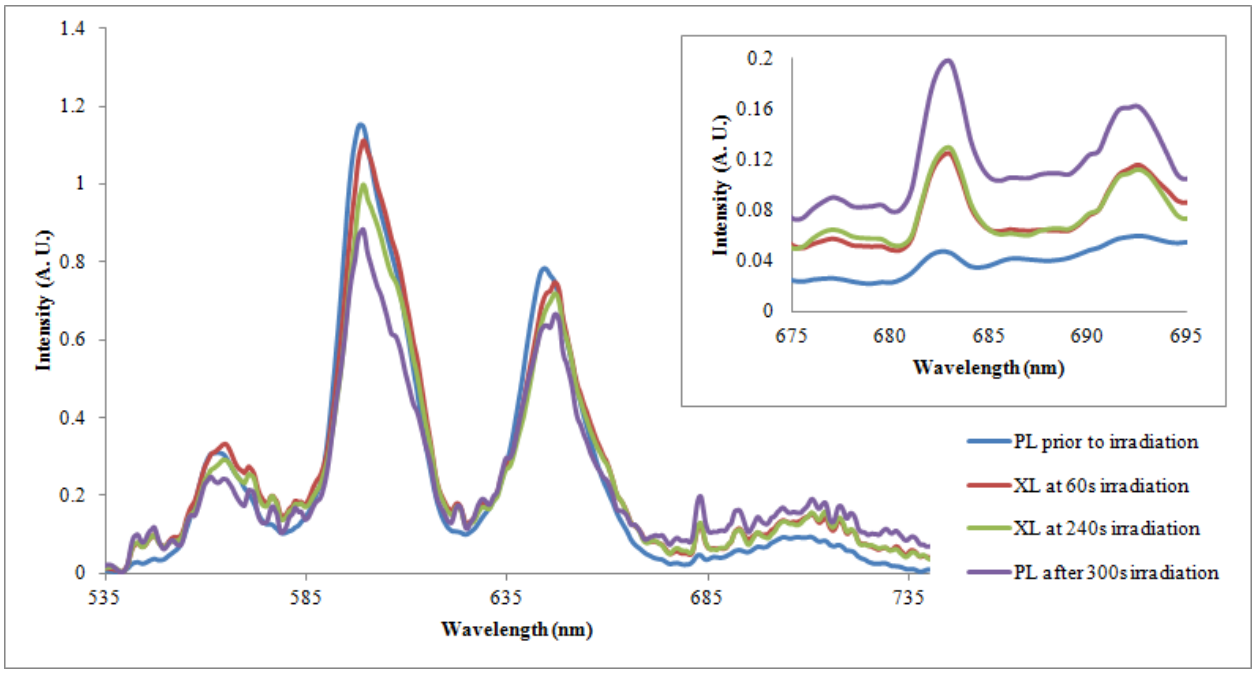

Figure 4.12 PL and XL spectra of BaF_2-B_2O_3-$Na_4P_2O_7$ doped with 0.33 wt% Sm_2O_3 material, annealed at 600 °C for 12 hours.

4.2 Absorption Spectra

In this subsection, the absorption spectrum of the BaF_2-B_2O_3-$Na_4P_2O_7$ doped with 0.33 wt% Sm_2O_3 material synthesized from the melt quenched to room temperature is presented in Figure 4.13. The absorption range from 180 nm to 300 nm is qualitatively changed with the extent of x-ray irradiation. The blue curve represents the sample before irradiation. The red curve represents the sample irradiated at low intensity and low x-ray energy. The x-ray energy and intensity were increased and caused a considerable change in transmission spectra as is seen represented by the green curve. High intensity and high energy x-rays would result in a greater dose in Grays. Then, the material shows an appreciable increase in colour centres only after high dose. This would mean that this material might be capable of registering high doses. Also, the effect of the x-ray induced colour centres on the absorption spectrum is present at room temperature; thus, this material satisfies the need for electronic defects to be capable of x-ray storage phosphor function. This is indeed confirmed by Figure 4.9 which demonstrates x-ray storage function via x-ray induced increase in absorption seen for the 683 nm peak. Furthermore, according to a study on a

Sm_2O_3 doped glass, x-ray irradiation was believed to have produced an absorption peak centred at 270 nm, indicating structural bond breakdown. Thus, Sm^{3+} could be possibly supplied with electrons by radicals resulting from bond breakdown to convert to Sm^{2+} valency [37]; hence, oxygen hole centres form.

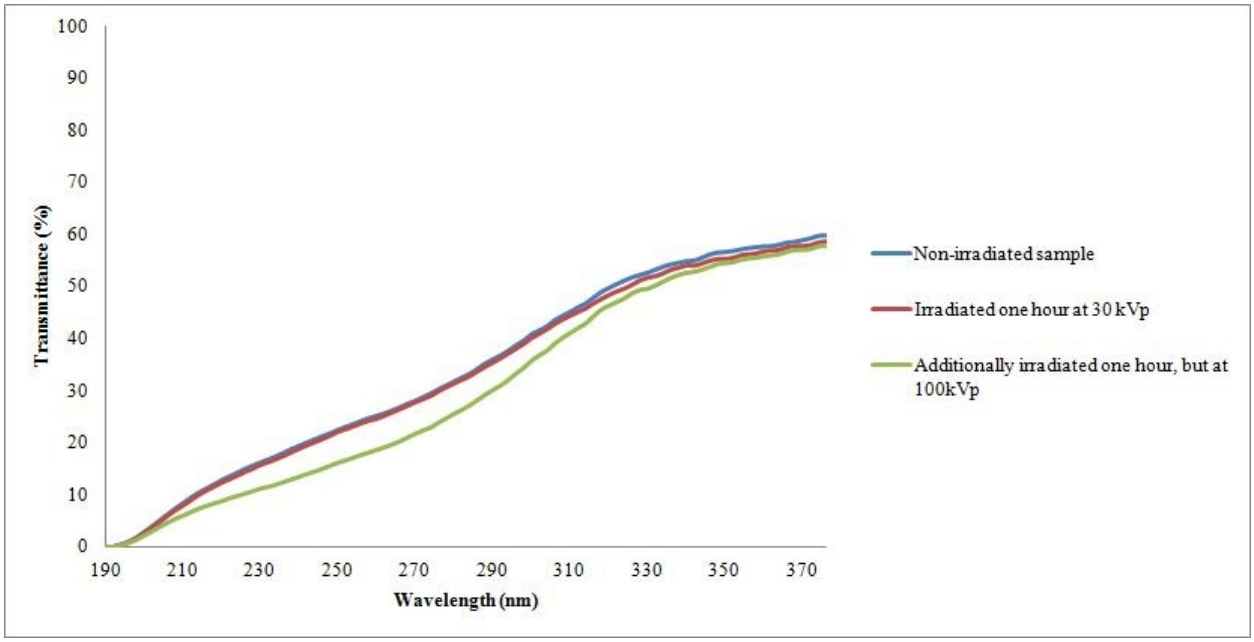

Figure 4.13 The transmittance of non-annealed BaF_2-B_2O_3-$Na_4P_2O_7$ doped with 0.33 wt% Sm_2O_3. The y-axis shows the transmittance and the x-axis shows the light wavelength in nanometres.

4.3 ESR Spectra

The ESR spectra for $BaBPO_5$ doped with 1 mol% Sm_2O_3 was absent for non-irradiated samples. For the irradiated $BaBPO_5$ doped with 1 mol% Sm_2O_3 sample, a first derivative ESR spectrum was visible and is shown in Figure 4.16. Thus, paramagnetic defects probably arose from x-ray irradiation. The bonding of the material prior to x-ray irradiation was likely to be nearly complete; no detectable amount of unpaired electrons remained in the materials after synthesis.

The first derivative ESR spectrum of the background includes the quartz tube sample holder and is in Figure 4.15. The quartz tube had little effect on the ESR spectra when numerically integrated. Its peak intensity was at less than 35000, in units of similar magnitude to those in

Figure 4.16. A subtraction of the quartz tube signal was not possible, even with account of the fluctuating microwave frequency by renormalization. This may be due to nonlinearity in the peak broadening since the quartz signal is likely composed of Lorentzian and Gaussian functions. Figure 4.16 has graphed both the numerically integrated data from Figure 4.14 and also the curve fit model. Table 4.1 has displayed the calculated g-values for the two visible peaks from Figure 4.16.

Table 4.1: Key Features of the $BaBPO_5$ doped with 1mol% Sm_2O_3 ESR spectrum.

	Peak 1	Peak 2
Peak intensity (A.U.)	480581	446281
Centre B Field (Gauss)	3417.655762	3445.164795
Peak g-value	2.018992867	2.002871565

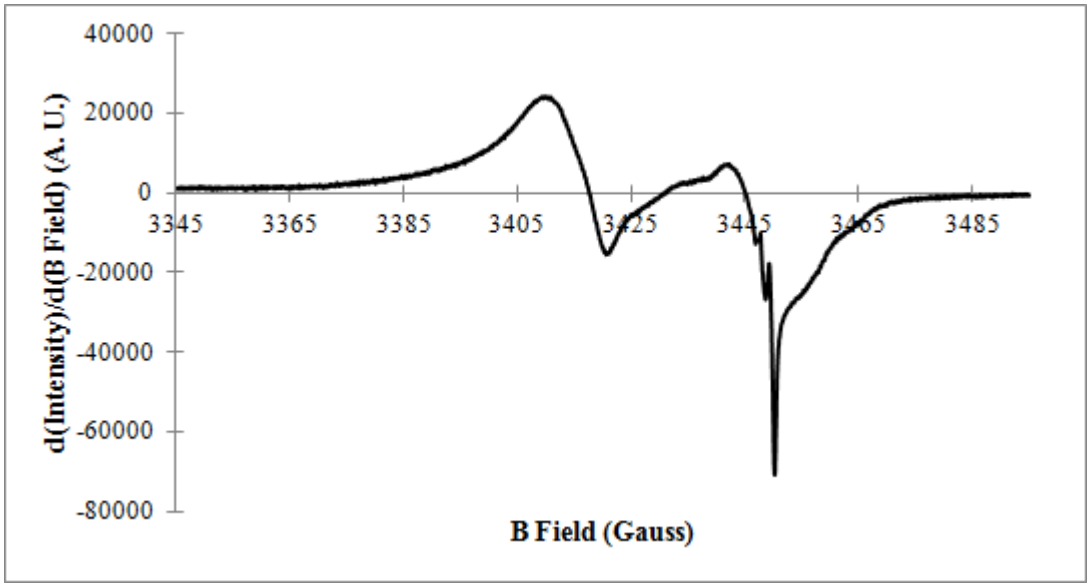

Figure 4.14 First derivative of the intensity w.r.t. B Field for $BaBPO_5$ doped with 1 mol% Sm_2O_3. The microwave frequency was at 9.657721 GHz.

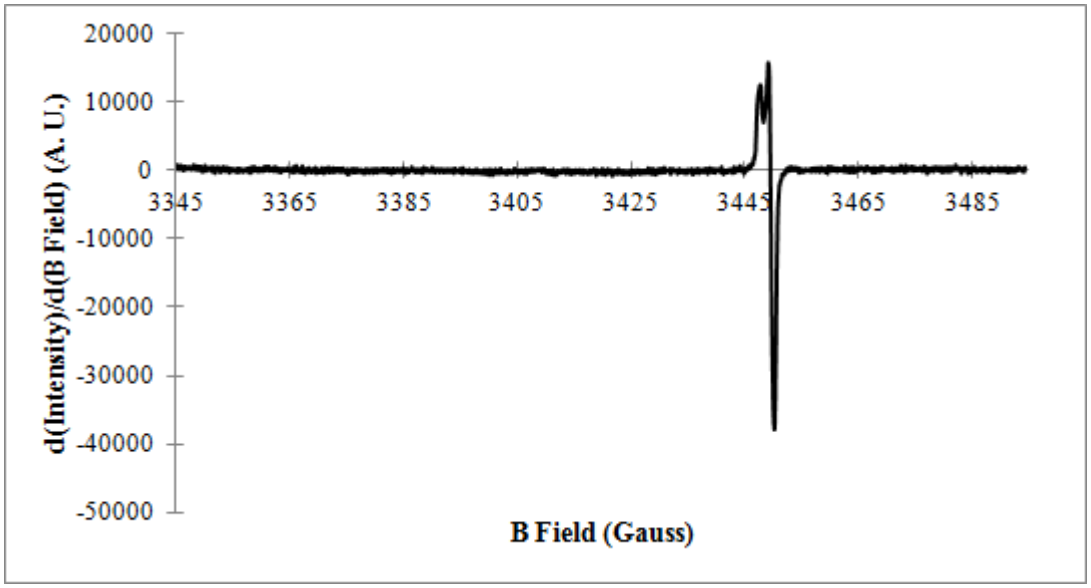

Figure 4.15 First derivative of the intensity w.r.t. B Field for the quartz tube sample holder. Assay at 9.660128 GHz microwave radiation frequency, but renormalized to 9.657721 GHz.

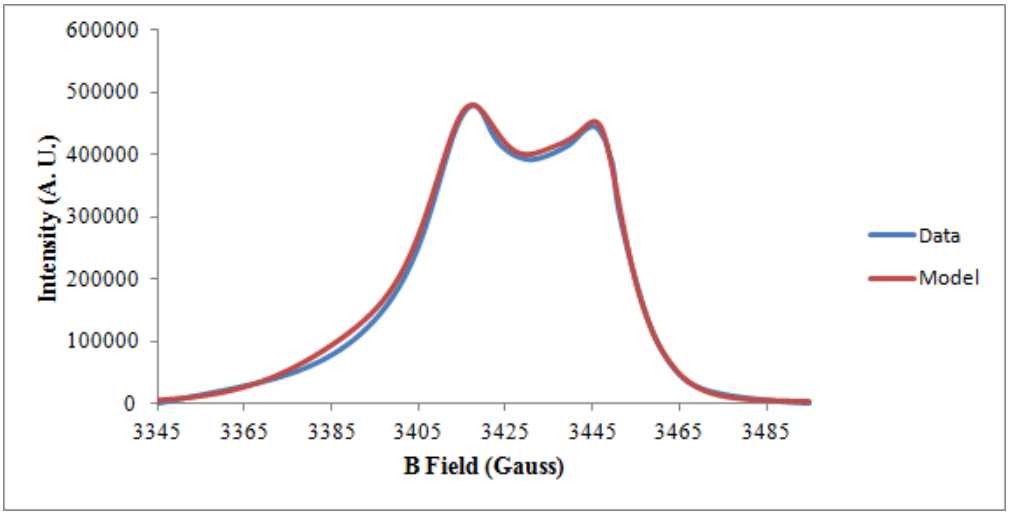

Figure 4.16 The intensity versus applied magnetic field ESR spectra of $BaBPO_5$ doped with 1 mol% Sm_2O_3, excited with 9.657721 GHz microwave radiation. Also shows curve fit model.

The model in Figure 4.16 is based on 4 Gaussian functions and 2 Lorentzian Functions. The Lorentzian functions were each centred with one Gaussian function. Table 4.2 contains an overview of the curves composing the model used in Figure 4.16. There are six curves that appeared to fit the numerically integrated data.

Table 4.2 Curve fit model as seen in Figure 4.16.

Curve	Type	FWHM, ΔB_{half} (Gauss)	Maximum Intensity, I_o (A.U.)	Centre Applied B Field, B_o (Gauss)
1	Gaussian	53.0697	130000	3408.53
2	Gaussian	20.3861	120426	3416.32
3	Lorentzian	20.3861	218368	3416.32
4	Gaussian	27.172	302902	3440.08
5	Gaussian	10.124	58139	3447.39
6	Lorentzian	10.124	83645	3447.39

The lifetime associated with Lorentzian curve #3 was 5.52e-9 seconds. For Lorentzian curve #6, the lifetime was 1.12e-8 seconds. These lifetimes were calculated using Equation (2.20) and the data from Table 4.2. Curve #3 corresponds to first peak and curve #6 corresponds with the second peak at higher frequency. These peaks are composed of both Gaussian and Lorentzian functions and are therefore inhomogeneously broadened; however, the Lorenzian functions themselves show homogeneous broadening with lifetimes associated to them.

The derivative spectrum in [38] has two nodes associated with its Sm doped material and hence two peaks (with g-values approximately 2). The g-values for the two nodes (peaks) are found in Table 4.1, which demonstrates analogous behaviour to [38]. These g-values are near the value for the free electron which is 2.00231930436153(53) using a high precision value from [35]. The first peak has a slightly lower g-value and the second peak has a slightly higher g-value. From [38], the ESR spectra are from another Sm doped material: sodium metaphosphate. This suggests that the two nodes (peaks) in Figure 4.14 correspond to polycrystalline and glass defects as in [38]. This result corroborates with the visual inspection of the sample. The $BaBPO_5$ material had a translucent and an opaque side, indicating glass and crystalline phases as predominant constituents, respectively. This result is similar in some respects to those in [37] for Sm^{3+} doped materials (but sol-gel derived). There was only one apparent ESR peak for the Sm doped sol-gel glass after x-ray irradiation in [37], but with a g-value greater than that of the free electron corresponding to oxygen hole centres. In this study, it could also be that oxygen hole centres contribute to the ESR signal as Sm^{2+} will not be detected via ESR [37]. Another study on

phosphate glass determined oxygen hole centres had a g-value of 2.014(1) for an oxygen and cation complex [39].

4.4 Raman Spectra

Raman spectral acquisitions for $BaBPO_5$ doped with 1 mol% Sm_2O_3 and for BaF_2-B_2O_3-$Na_4P_2O_7$ doped with 0.33 wt% Sm_2O_3 are presented in this subsection. Each spectral acquisition is presented with an optical microscope image.

4.4.1 $BaBPO_5$ doped with 1 mol% Sm_2O_3 Material

$BaBPO_5$ material, doped with Sm_2O_3 is presented herein. Figure 4.17 and Figure 4.18 display graphically the spectral data for non-irradiated crystalline and glass sides of the sample. Figure 4.19 and Figure 4.20 display the same, but after irradiation. The Raman Spectral of $BaBPO_5$ peaks were compared to corresponding peaks found in [40]. The peaks are compared in Table 4.3. As is shown in the table, there are peaks that are unlikely associated with $BaBPO_5$ and more likely associated with compounds $Ba_3BP_3O_{12}$, α- or δ-$Ba_2P_2O_5$. Of the three latter phases, the α- or δ-$Ba_2P_2O_5$ are less likely due to the 984 cm^{-1} peak appearing with higher intensity, which was thus more similar to the peak generated by $Ba_3BP_3O_{12}$ [40]. This can be explained by the possibility of borate groups evaporating during the high temperature synthesis of the material. This could mean that even more boric acid is needed to compensate for reagent vaporization during synthesis. There are still peaks associated with $BaBPO_5$ and hence there could be a considerable amount of $BaBPO_5$ remaining. These Raman active vibrations were attributed in [40] to borate and phosphate groups undergoing symmetric and asymmetric bends or stretches. These various Raman modes were labelled similarly as in [40]. Thus, the four frequencies ν_x (where x = 1, 2, 3, 4) are the $BaBPO_5$ irreducible representations A_1, E, F_2 and F_2, respectively. The ν_{as}, ν_s, and ν are frequencies associated with the representations of compounds formed with boron loss. The subscript "as" represents asymmetric stretches and "s" represents symmetric

stretches. Thus, from the mix of peaks found in the $BaBPO_5$ material, it is likely there is a mixture of phases. These phases include the stochiometric $BaBPO_5$, but also Ba_3BPO_{12}, BPO_4, and α- or δ-$Ba_2P_2O_5$ compounds with distinct Raman spectra. These extra compounds may have formed during the long synthesis process, which could have decomposed $BaBPO_5$ compound with the loss of BO_2 to the furnace atmosphere which was ventilated.

Table 4.3 Select non-irradiated Sm_2O_3 doped $BaBPO_5$ materials Raman spectral peaks, compared to [40].

Stokes's Shifts, in (cm^{-1})					Vibration mode from [40]
$BaBPO_5$: Sm_2O_3 crystalline	$BaBPO_5$: Sm_2O_3 glass	$BaBPO_5$ From [40]	$Ba_3BP_3O_{12}$, BPO_4 From [40]	α- or δ-$Ba_2P_2O_5$ From [40]	
	357	358, 360			$\nu_2(BO_4) + \nu_2(PO_4)$
	392	396			$\nu_2(BO_4) + \nu_2(PO_4)$
419	422	418	420		$\nu_2(BO_4) + \nu_2(PO_4)$
	434			428	$\delta(PO_4)$
	456	462			$\nu_2(BO_4) + \nu_2(PO_4)$
509		514	510		$\nu_4(PO_4)$
	550			552	$\nu_s(POP)$
562	568	570, 574			$\nu_4(BO_4)$
	633		636		$\nu_4(BO_4)$
	707			704	$\nu_s(POP)$
	938	934			$\nu_3(BO_4)$
	965	956			$\nu_3(BO_4)$
984	984		$\nu_1(PO_4) = 984$	$\nu_{as}(PO_3) = 984$	$\nu_1(PO_4)$, $\nu_{as}(PO_3)$
1023	1014		$\nu_3(PO_4) = 1024$	$\nu_s(PO_3) = 1018$	$\nu_3(PO_4)$, $\nu_s(PO_3)$
	1094	1098			$\nu_3(PO_4)$
1122			1122, 1124		$\nu(BPO_7)$
1138			1140		$\nu_3(PO_4)$

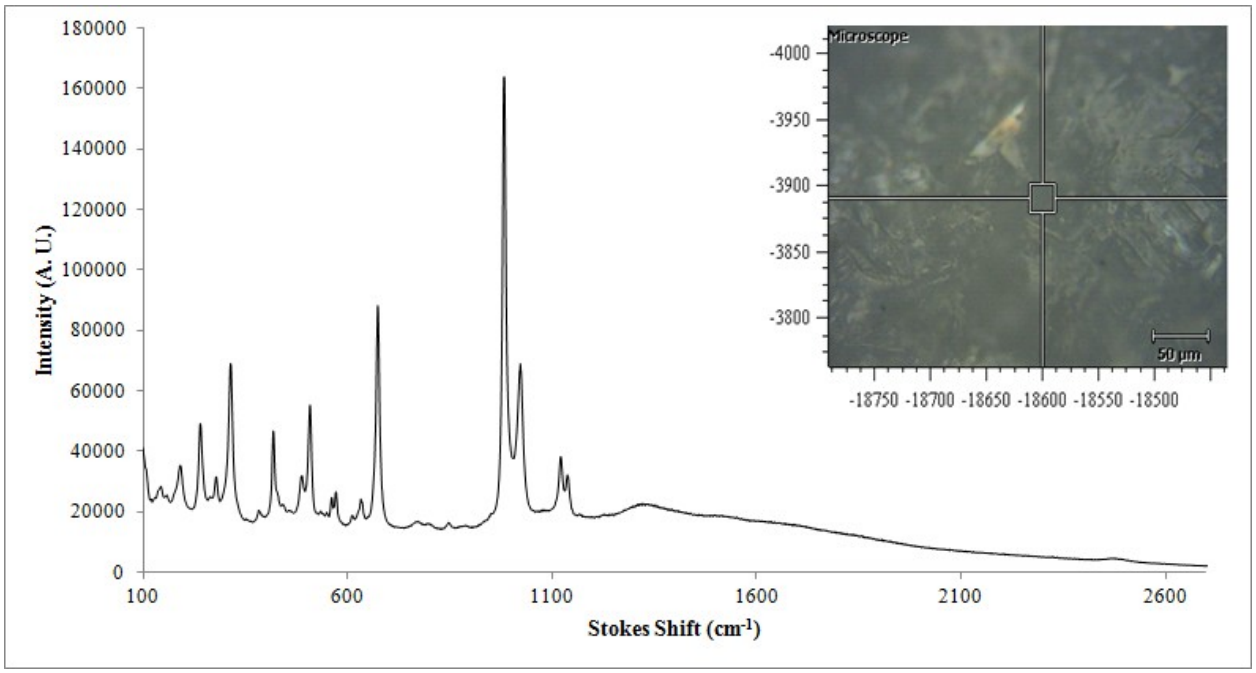

Figure 4.17 Raman Spectra for non-irradiated $BaBPO_5$ doped with 1 mol% Sm_2O_3 crystalline side. Inset is a photograph of the assayed sample surface.

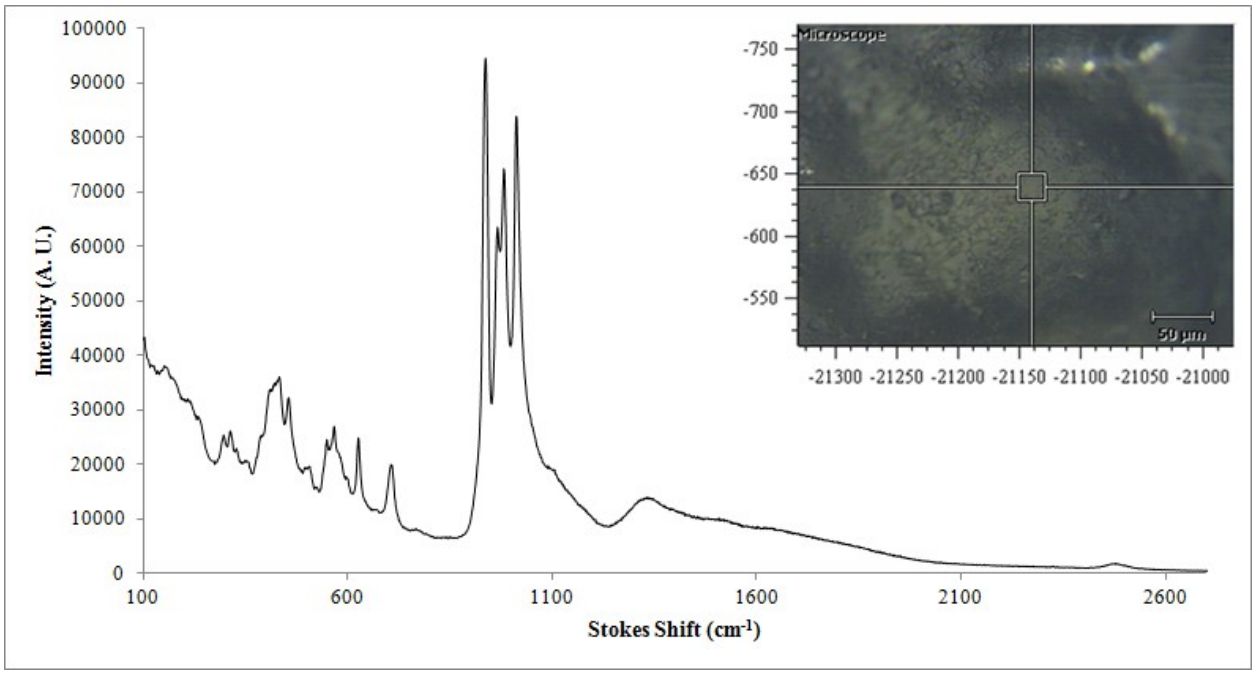

Figure 4.18 Raman Spectra for non-irradiated $BaBPO_5$ doped with 1 mol% Sm_2O_3 glass side. Inset is a photograph of the assayed sample surface.

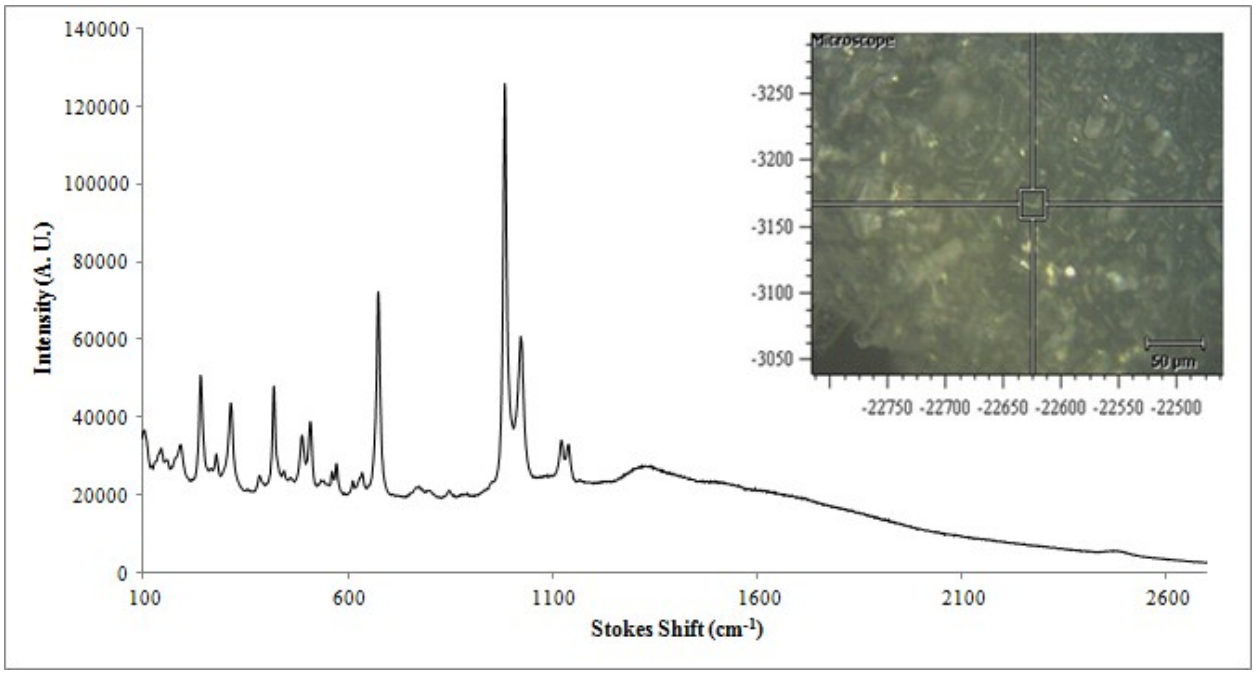

Figure 4.19 Raman Spectra for irradiated $BaBPO_5$ doped with 1 mol% Sm_2O_3 crystalline side. Inset is a photograph of the assayed sample surface.

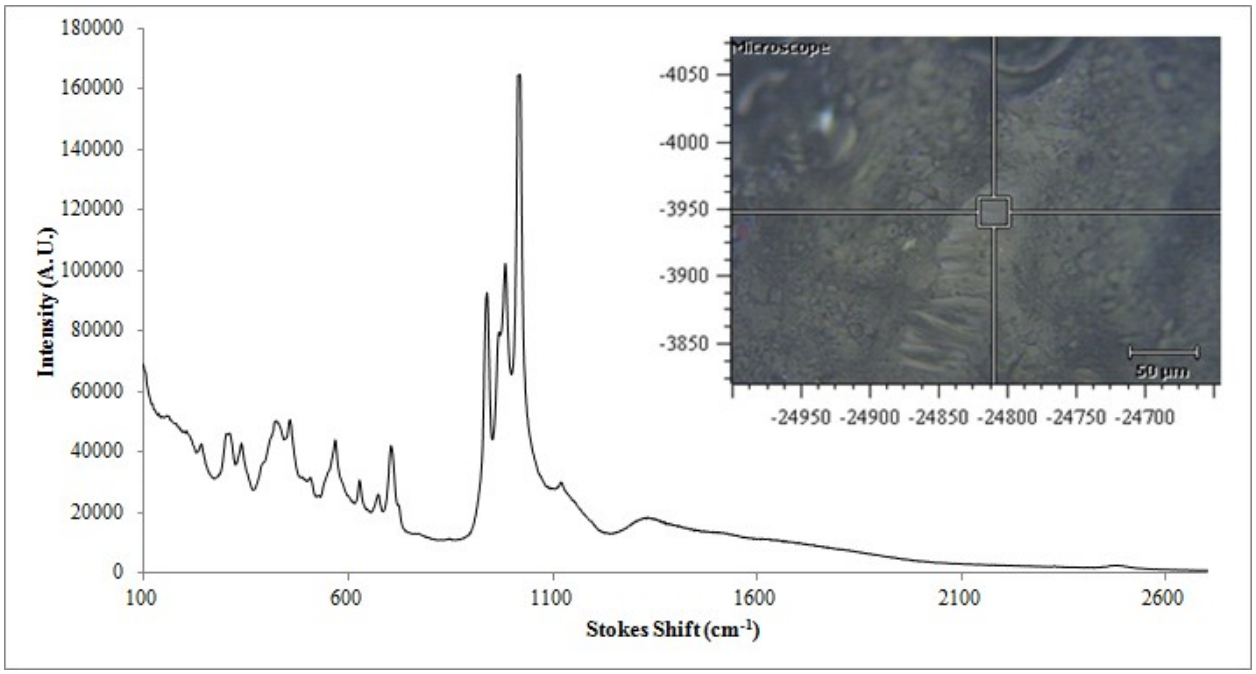

Figure 4.20 Raman Spectra for irradiated $BaBPO_5$ doped with 1 mol% Sm_2O_3 glass side. Inset is a photograph of the assayed sample surface.

4.4.2 BaF_2-B_2O_3-$Na_4P_2O_7$ doped with 0.33wt% Sm_2O_3 Material

The Raman spectra of the BaF_2-B_2O_3-$Na_4P_2O_7$ doped with 0.33 wt% Sm_2O_3 material is presented in Figures 4.21 to 4.28 below. Each graph is accompanied with a microscopic image of the surface that was excited. Figure 4.21 shows broad peaks grouped about 1000 cm^{-1} to 1700 cm^{-1}. These peaks are likely associated phosphorous-oxygen molecules. These peaks could possibly correspond to the peak arising from the symmetric stretching of PO_2 bonds in the material, according to the 1009 to 1275 cm^{-1} peaks in [30]. The broadness is an indicator that this sample is composed of glass phase. The effect of x-ray irradiation on this sample material is graphed in Figure 4.22 and differs from the sample before irradiation.

There are peaks below 1100 cm^{-1}, some of which arise after irradiation. Figure 4.23 is of the hot quenched sample prior to x-ray irradiation and Figure 4.24 after x-ray irradiation. The observances of peaks that manifest after irradiation for the non-annealed samples is contrasted to the phenomena exhibited by annealed samples. The six hour annealed sample is shown before and after x-ray irradiation in Figure 4.25 and Figure 4.26, respectively. The six hour annealed sample before and after irradiation appeared similar to the non-irradiated, non-annealed samples. Then, for the glass phase, irradiation produced an effect similar to annealing. The two peaks just below 700 cm^{-1} are likely symmetric stretching of P-O-P bonds, according to the 696 cm^{-1} peak in [30]. Broad peaks remain in the six hour annealed material and hence it is likely composed predominantly of glass phase. For the 12 hour annealed sample, its Raman spectra are seen in Figure 4.27 before irradiation and in Figure 4.28 after irradiation. This sample also was not highly affected by x-ray irradiation according to the spectra before and after irradiation. It also contains very sharp peaks. These sharp peaks would mean that the sample is highly crystalline. Since the sample became opaque after 12 hours of annealing, this result of sharp Raman spectral peaks is expected. The appearance of peaks below 1100 cm^{-1} are possibly also associated with oxygen hole centres that are formed by x-ray irradiation. PO_4 units at 1275 cm^{-1} spectral peak have only one non-bridging oxygen initially [30]. Then, an oxygen hole centre forming from a bridging oxygen would then cause the phosphate tetrahedra to be bonded to two bridging oxygen only. In turn, separate peaks would form.

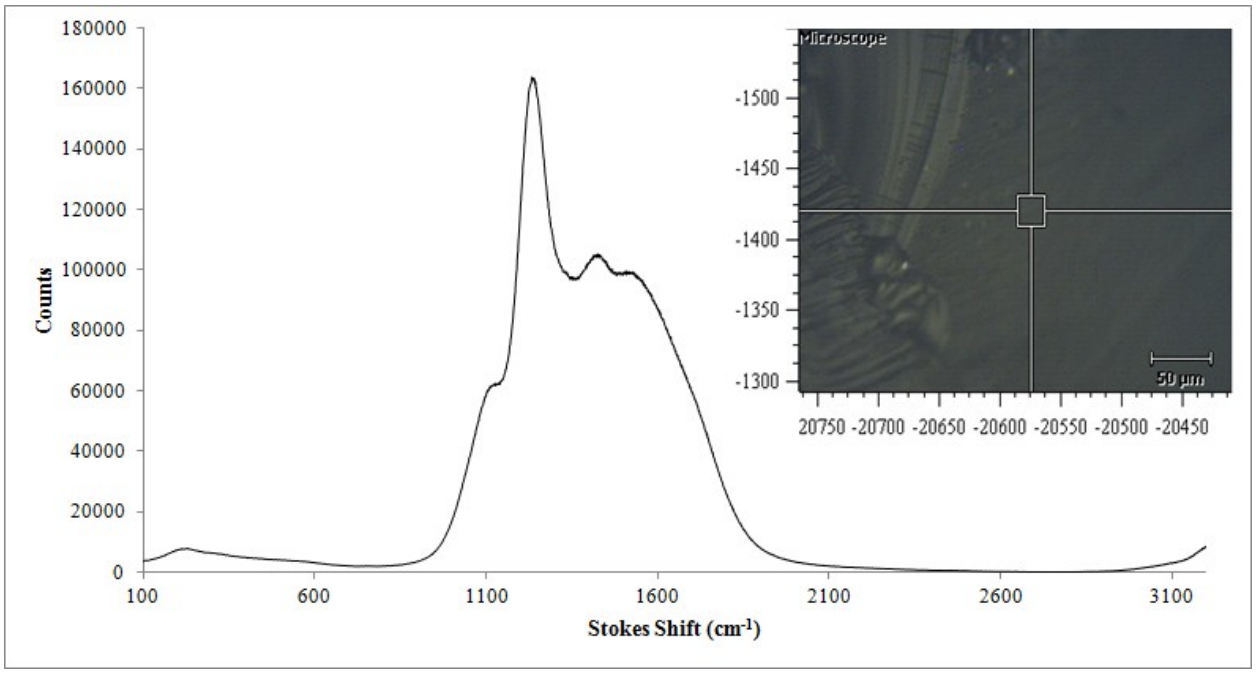

Figure 4.21 Raman spectrum of BaF_2-B_2O_3-$Na_4P_2O_7$ doped with 0.33 wt% Sm_2O_3 material quenched to Room Temperature. Inset is a photograph of the assayed sample surface.

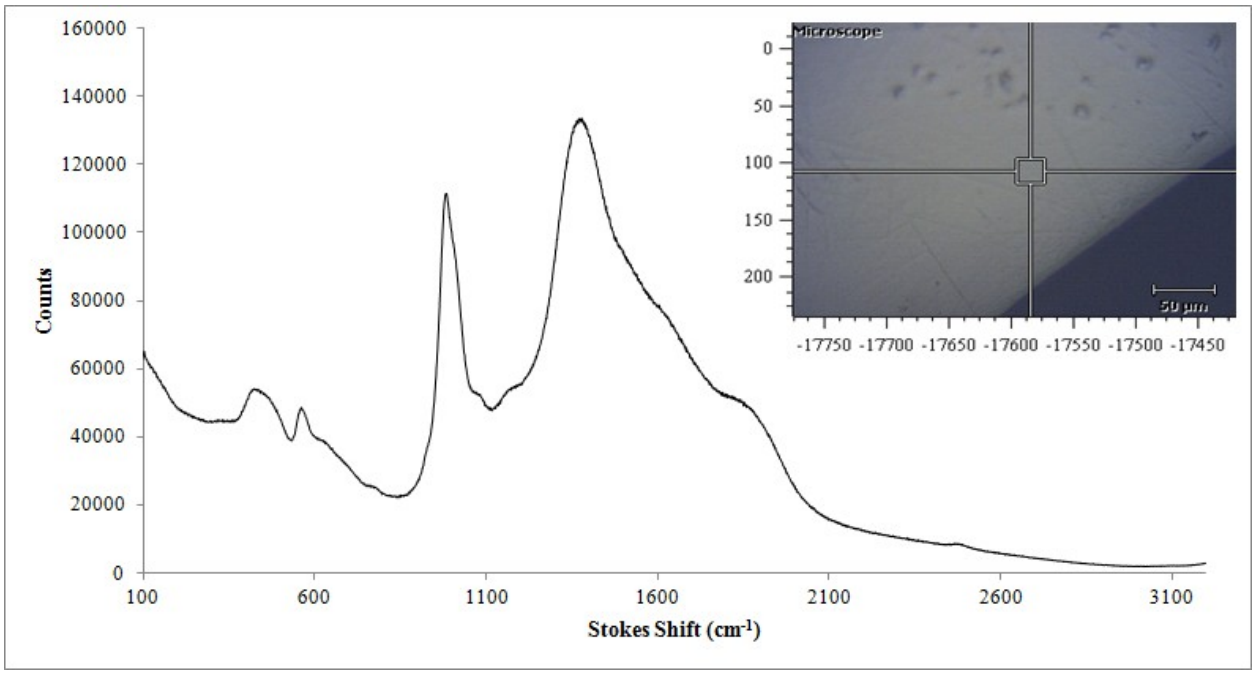

Figure 4.22 BaF_2-B_2O_3-$Na_4P_2O_7$ doped with 0.33 wt% Sm_2O_3 quenched to Room Temperature and irradiated with the x-ray cabinet. Inset is a photograph of the assayed sample surface.

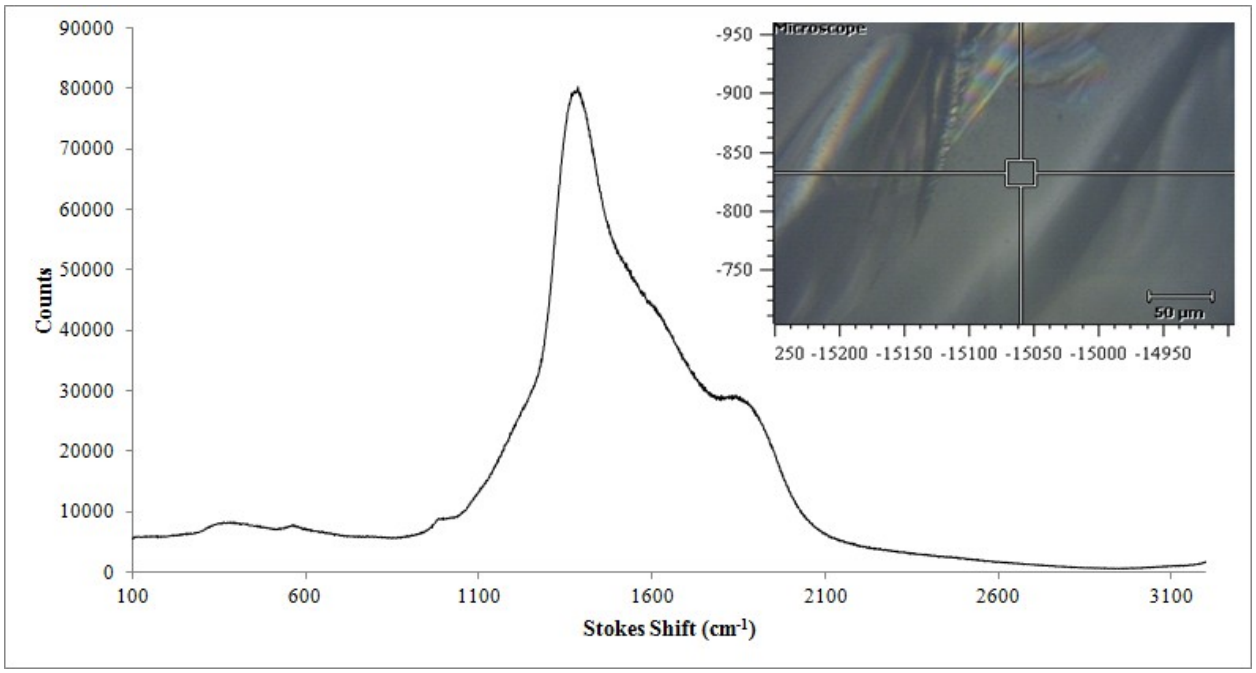

Figure 4.23 BaF_2-B_2O_3-$Na_4P_2O_7$ doped with 0.33 wt% Sm_2O_3 hot quenched, and non-annealed. Inset is a photograph of the assayed sample surface.

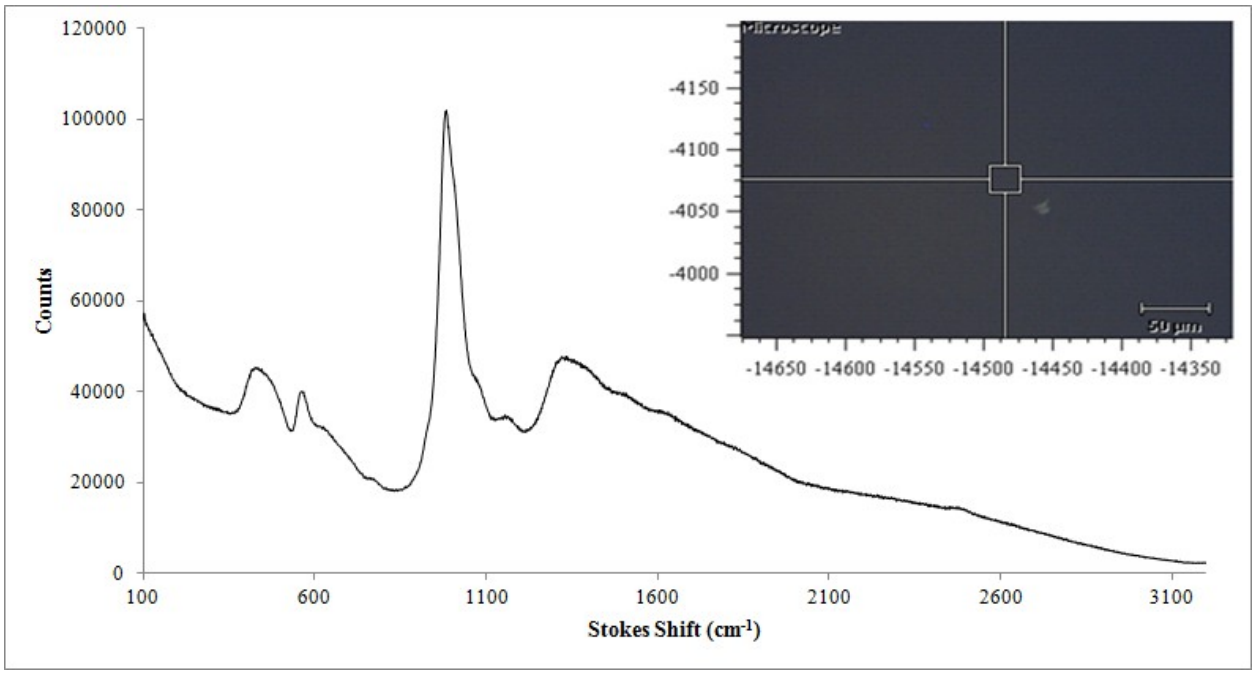

Figure 4.24 Irradiated BaF_2-B_2O_3-$Na_4P_2O_7$ doped with 0.33wt% Sm_2O_3 hot quenched, non-annealed. Inset is a photograph of the assayed sample surface.

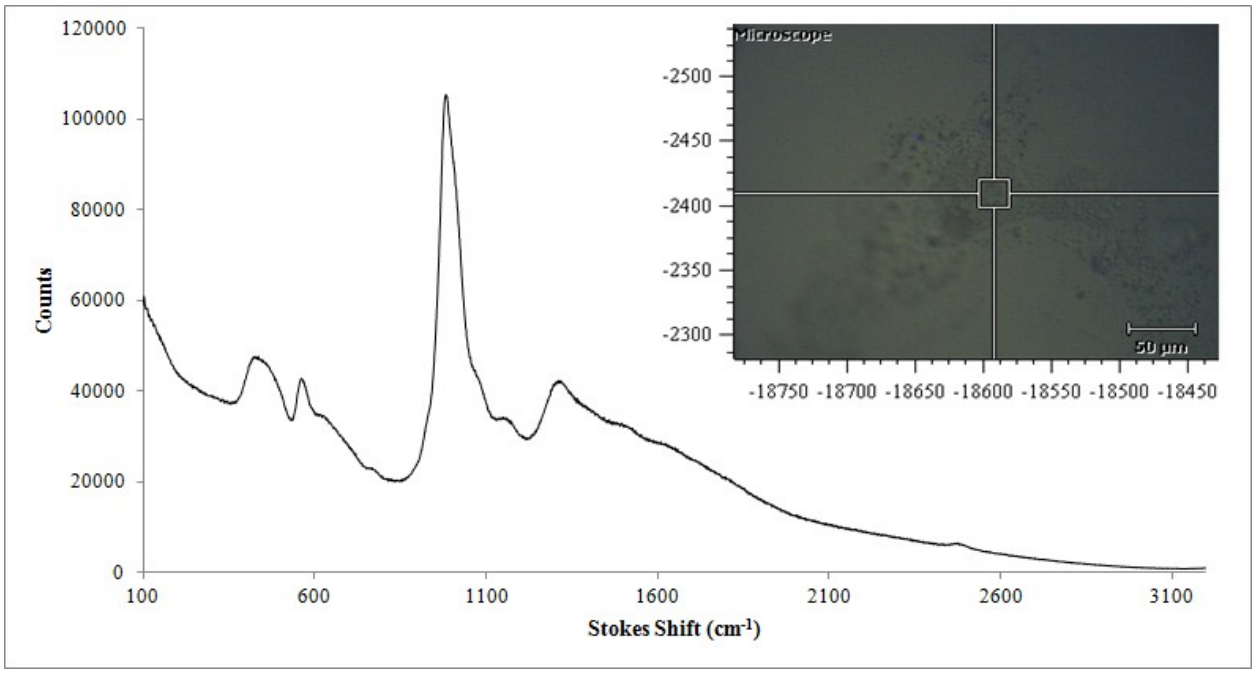

Figure 4.25 BaF_2-B_2O_3-$Na_4P_2O_7$ doped with 0.33 wt% Sm_2O_3 material annealed 6 hours at 600 °C and non-irradiated. Inset is a photograph of the assayed sample surface.

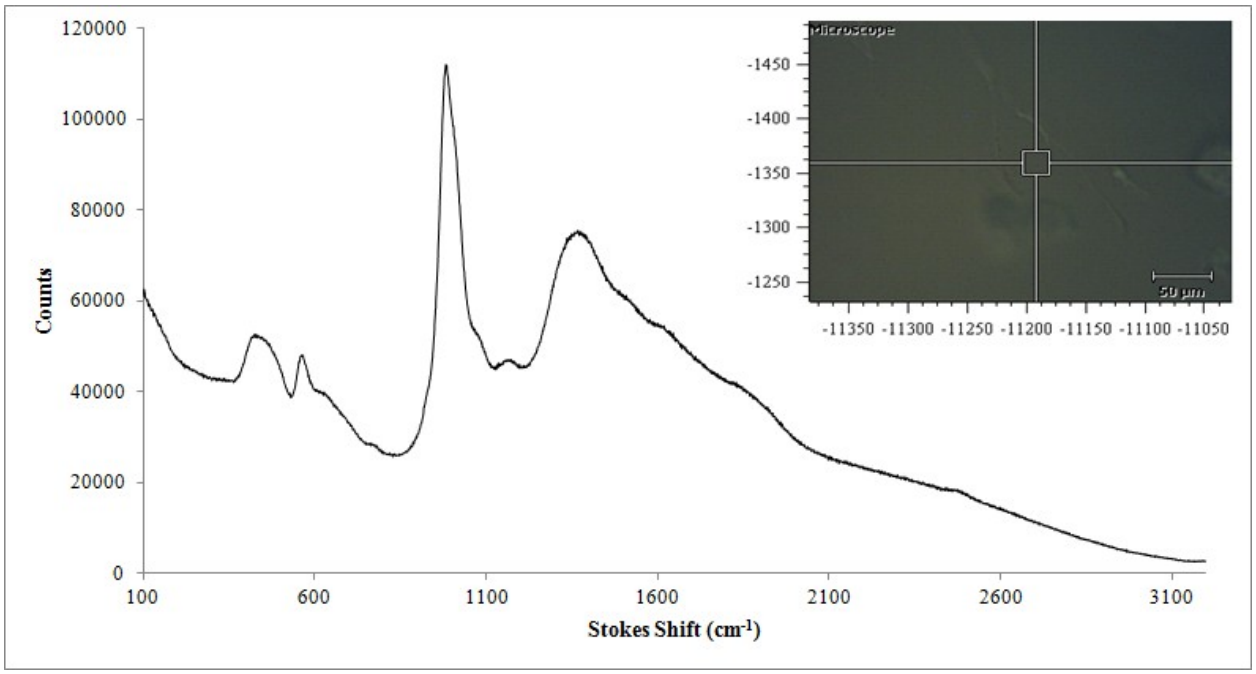

Figure 4.26 BaF_2-B_2O_3-$Na_4P_2O_7$ doped with 0.33 wt% Sm_2O_3 material annealed 6 hours at 600 °C and subsequently irradiated. Inset is a photograph of the assayed sample surface.

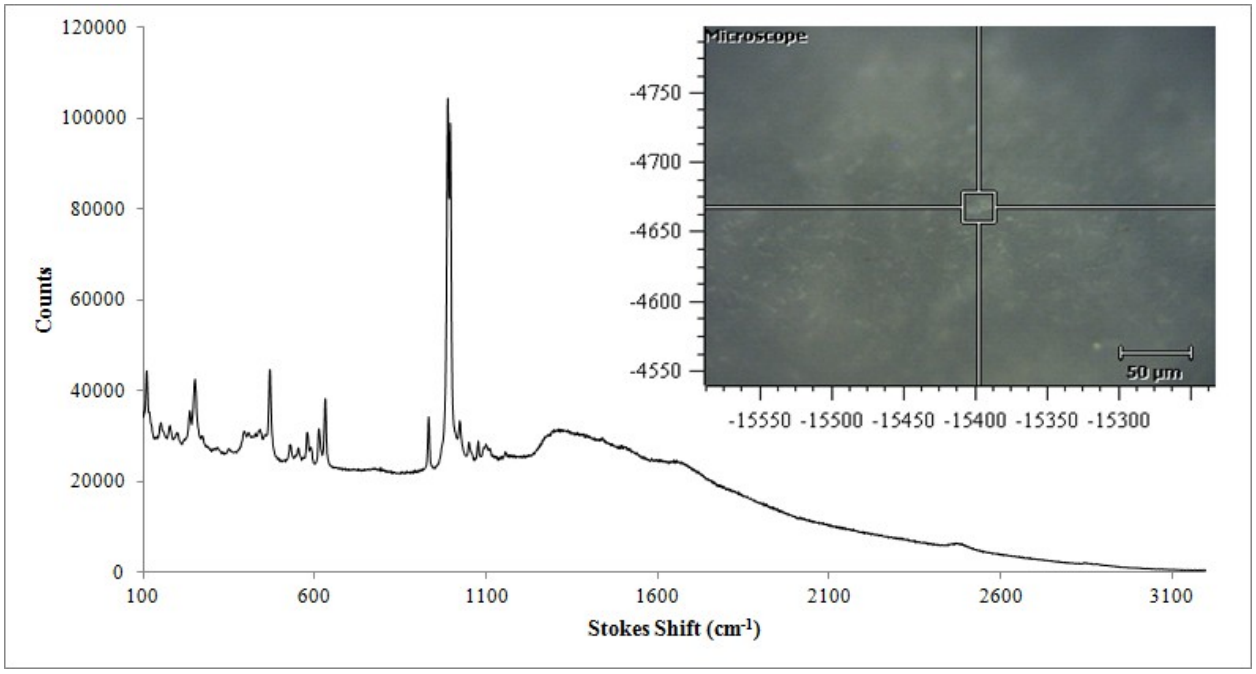

Figure 4.27 BaF_2-B_2O_3-$Na_4P_2O_7$ doped with 0.33 wt% Sm_2O_3 material annealed 12 hours at 600 °C and non-irradiated. Inset is a photograph of the assayed sample surface.

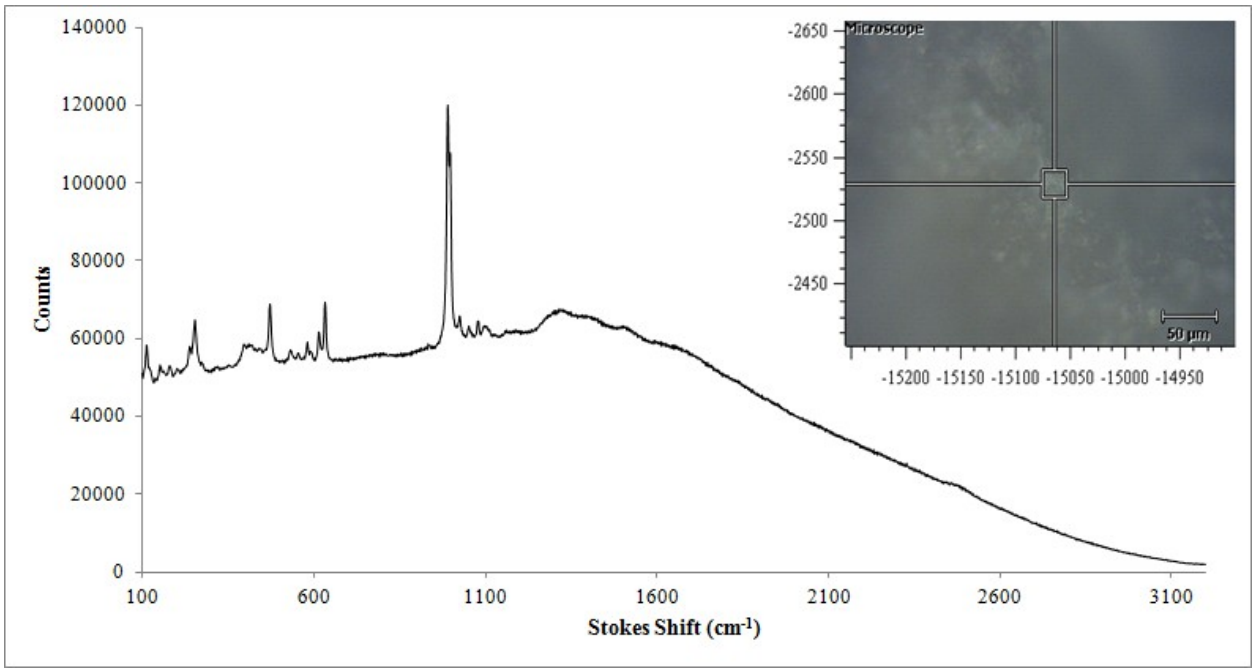

Figure 4.28 BaF_2-B_2O_3-$Na_4P_2O_7$ doped with 0.33 wt% Sm_2O_3 material annealed 12 hours at 600 °C and subsequently irradiated. Inset is a photograph of the assayed sample surface.

4.5 Powder XRD

In this subsection, the powder XRD results for $BaBPO_5$ materials are presented. Figure 4.29 is a plot of diffraction intensity versus double angle for $BaBPO_5$ powder diffraction. Using the Scherrer formula as shown in Equation (2.10) with the simplification in Equation (2.12) which assumes negligible width for large crystals, the grain size was determined to be 26 nm with 9 nm standard deviation. The grain size was determined using the five labelled peaks. Using the powder XRD data, the $BaBPO_5$ crystalline structure was confirmed and its unit cell is illustrated in Figure 4.30. In Figure 4.30, there are two tetrahedral groups present: PO_4 and BO_4 structural units. These two tetrahedral units with the pink Ba cations form a structural motif. The motif is composed of three PO_4 tetrahedra, three BO_4 tetrahedra and three Ba cations. The tetrahedral structural units in the motif are bonded by bridging oxygen.

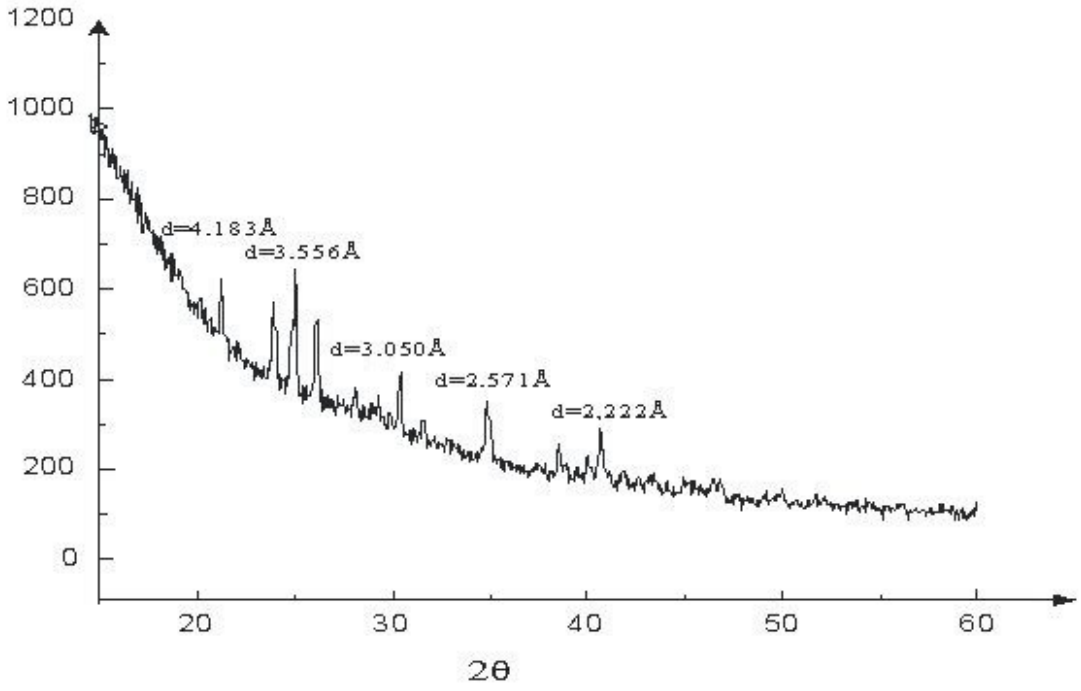

Figure 4.29 Powder XRD intensity, versus double angle plot for $BaBPO_5$ doped with 1 mol% Sm_2O_3. This figure is after D. Tonchev, E. Muzar, G. Okada, I. Kostova, Z. Stoeva, G. Patronov, B. Morrell and S.O. Kasap [36].

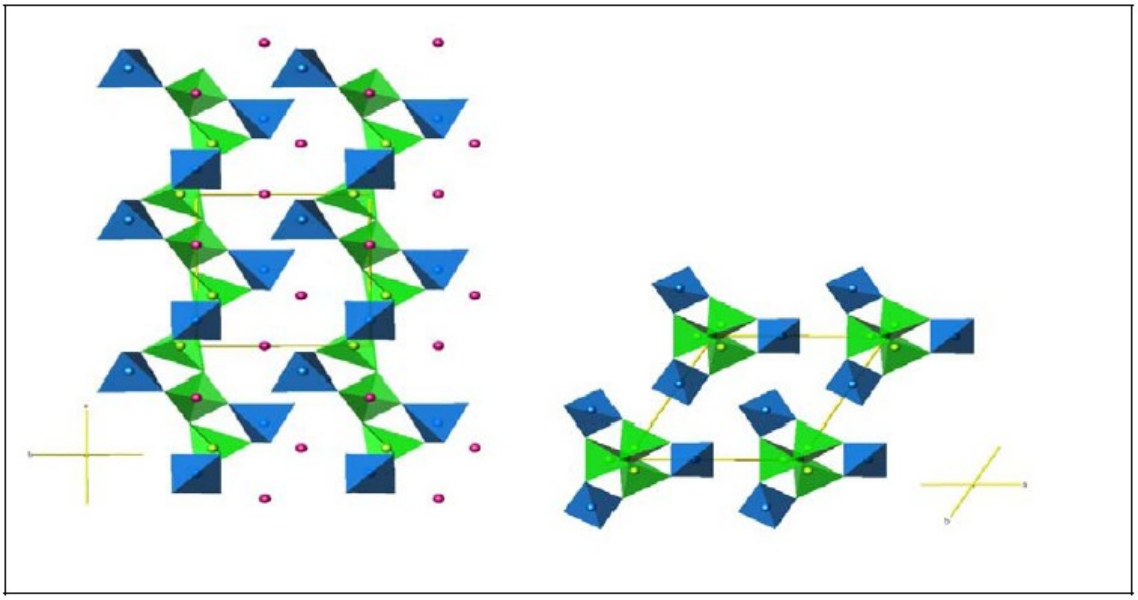

Figure 4.30 $BaBPO_5$ crystalline unit cell, determined via powder XRD. PO_4 tetrahedral units are green. Blue tetrahedral units represent BO_4 units. Ba cations are represented by pink particles. This figure is after D. Tonchev, E. Muzar, G. Okada, I. Kostova, Z. Stoeva, G. Patronov, B. Morrell and S.O. Kasap [36].

4.6 Thermal Analysis with DSC and MDSC

The thermal analysis results are presented below for select sample materials. The Q100 experimental setup allowed scanning up to 590 °C. $BaBPO_5$ (as well as the aluminosilicate material) did not exhibit any discernable thermodynamic transitions from room temperature to 590 °C. On the other hand, BaF_2-B_2O_3-$Na_4P_2O_7$ doped with 0.33 wt% Sm_2O_3 or 0.33 wt% SmF_3 materials were assayed and had thermodynamic transitions below the upper scanning limit of 590 °C. The BaF_2-B_2O_3-$Na_4P_2O_7$ material with either Sm dopant exhibited glass transition inflection points below 400 °C, depending on the sample dopant composition, thermal history and assay method (DSC or MDSC). These glass transition temperatures were similar to the T_g of the glass with composition of 30:30:40 from the B_2O_3-P_2O_5-Na_2O material system which was 431.19 °C according to [30]. Then, sodium modifier appears to have been a major cause of glass transition temperature lowering, relative to the $BaBPO_5$ compositions.

The Thermal Properties for Sm compound doped BaF_2-B_2O_3-$Na_4P_2O_7$ materials is displayed in Table 4.4. From this Table, the Hruby coefficient was calculated with Equation (2.56) using DSC data. The melting temperatures T_m were 950 °C or less since a melt was poured during the quenching process. Thus, 950 °C or less for melting temperatures was used to calculate the Hruby coefficient, which established an estimated lower limit for its value. The higher glass transition and crystallization onset temperatures are higher for the Sm_2O_3 doped material. This result would be expected considering the substantially higher melting point of the oxide and its more covalent behaviour. The higher melting point compound added as a dopant would more likely increase the melting temperature of the mixture. The much higher crystallization temperature for the Sm_2O_3 doped material resulted in a Hruby coefficient that was about twice that of the SmF_3 doped material. Both materials had a Hruby coefficient that was lower than 0.7, indicating that glass formation was not dominant, and that a mixture of glass and nucleated crystals was likely.

These transitions found in Table 4.4 are in a range that would be useful for manufacturing. The glass transition temperatures are close to an ideal 400 °C, which would allow BaF_2-B_2O_3-$Na_4P_2O_7$ materials to be commercially processed easily. The $BaBPO_5$ and silicate materials had a glass transition temperature beyond the ideal at 400 °C. Thus, according to this thermal analysis, the BaF_2-B_2O_3-$Na_4P_2O_7$ materials are favoured for future commercialization.

Table 4.4 Thermal Properties of SmF_3 or Sm_2O_3 doped BaF_2-B_2O_3-$Na_4P_2O_7$ materials.

Dopant	Annealing	T_g (°C)	T_x (°C)	T_m (°C)	Hruby coefficient, k
0.33 wt% SmF_3	None	396.97	485.07	≤950	≥0.1914
0.33 wt% SmF_3	24 hours on hot plate	396.67	481.61	≤950	≥0.1814
0.33 wt% Sm_2O_3	6 hours at 600 °C	397.16	546.32	≤950	≥0.3695
0.33 wt% Sm_2O_3	Only hot quenched	397.87	547.69	≤950	≥0.3724
0.33 wt% Sm_2O_3	Only cold quenched	399.61	548.08	≤950	≥0.3694

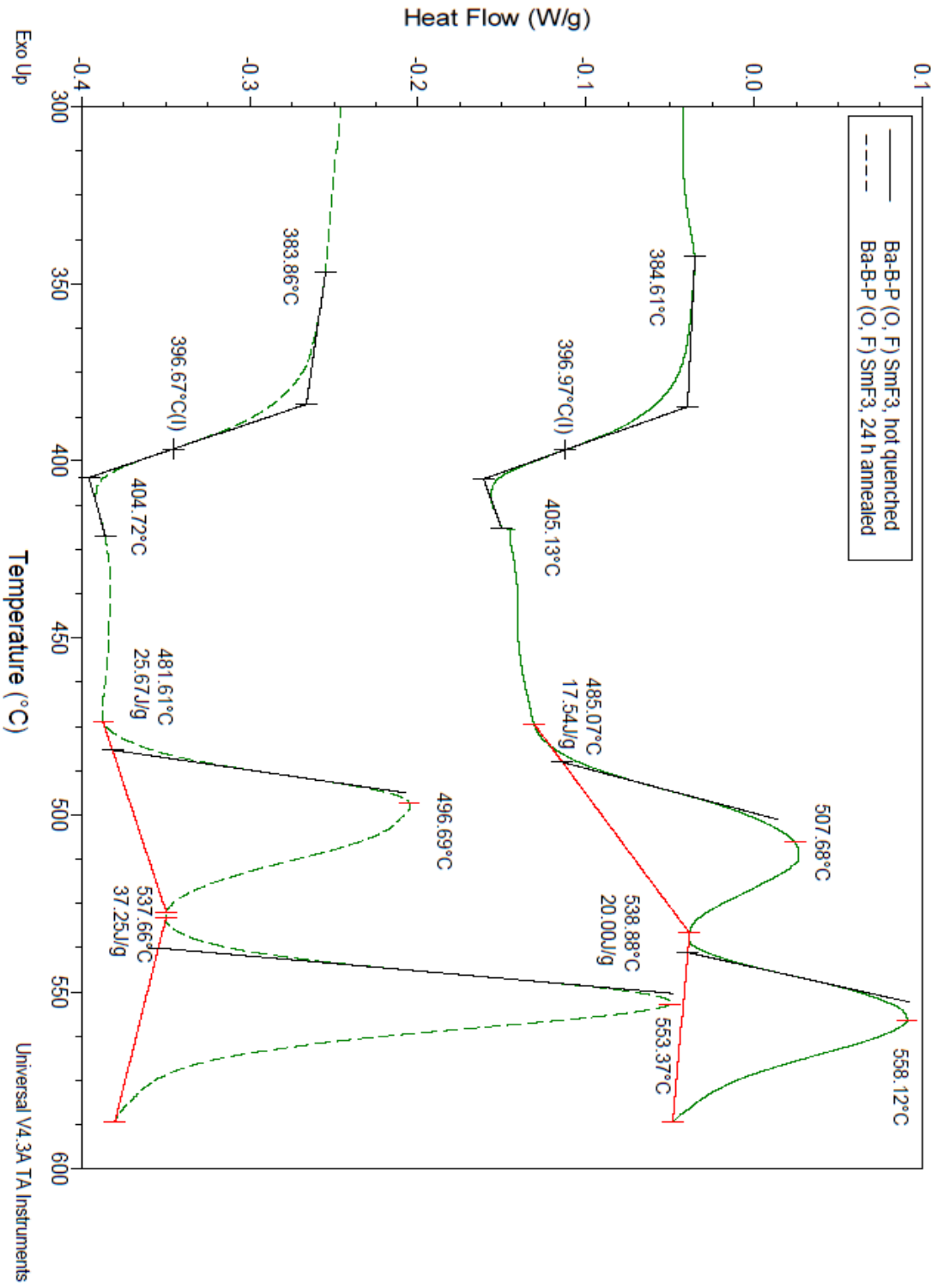

Figure 4.31 DSC thermograms of hot quenched BaF_2-B_2O_3-$Na_4P_2O_7$ doped with 0.33 wt% Sm_2O_3 materials. Solid line indicates hot quenched sample and dashed line indicates 24 h annealed at 250 °C sample.

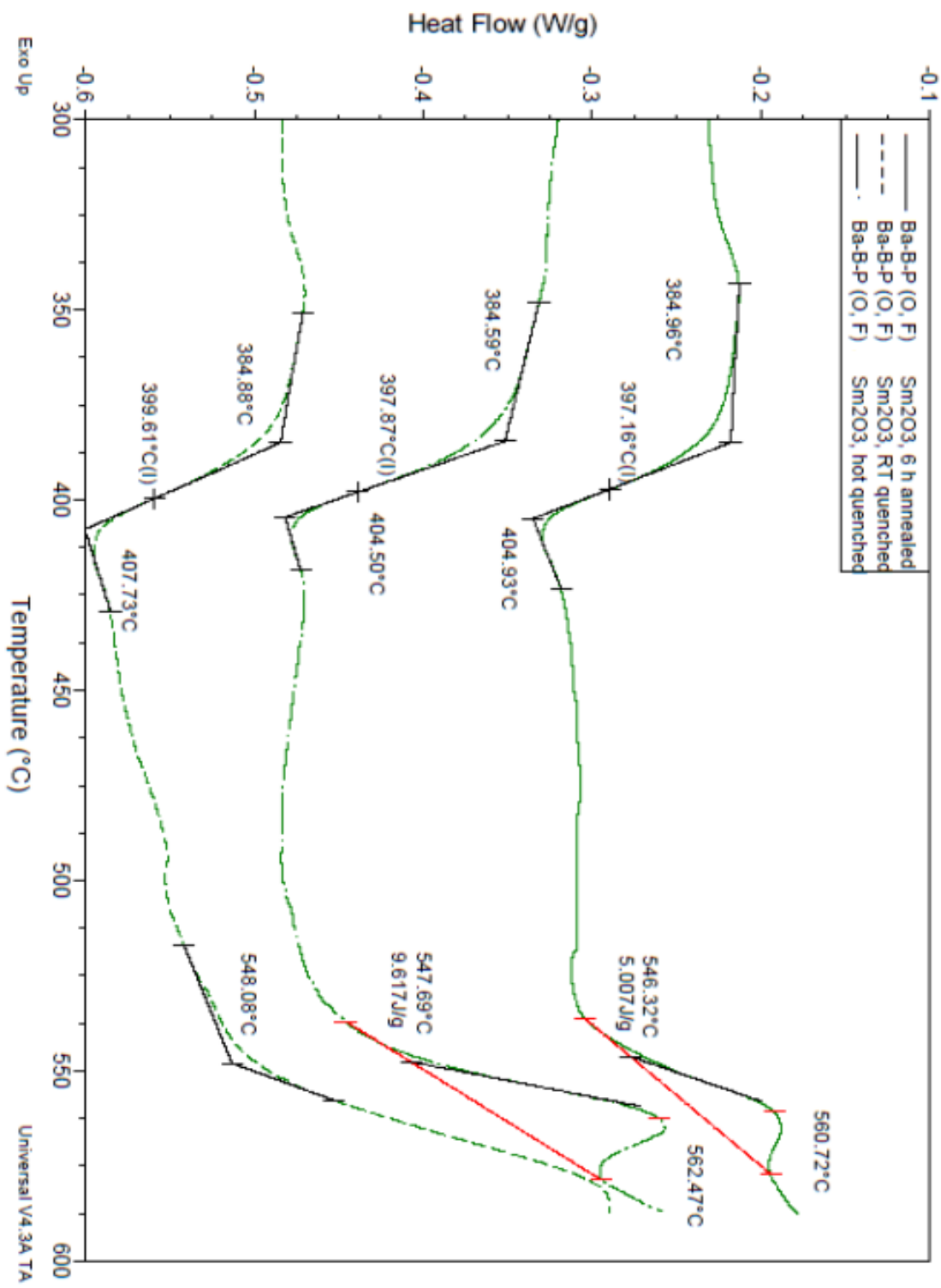

Figure 4.32 DSC thermograms of BaF_2-B_2O_3-$Na_4P_2O_7$ doped with 0.33 wt% Sm_2O_3 materials. Solid line, semi-dashed and dashed lines represent 6 hours annealed, room temperature quenched and hot quenched samples, respectively.

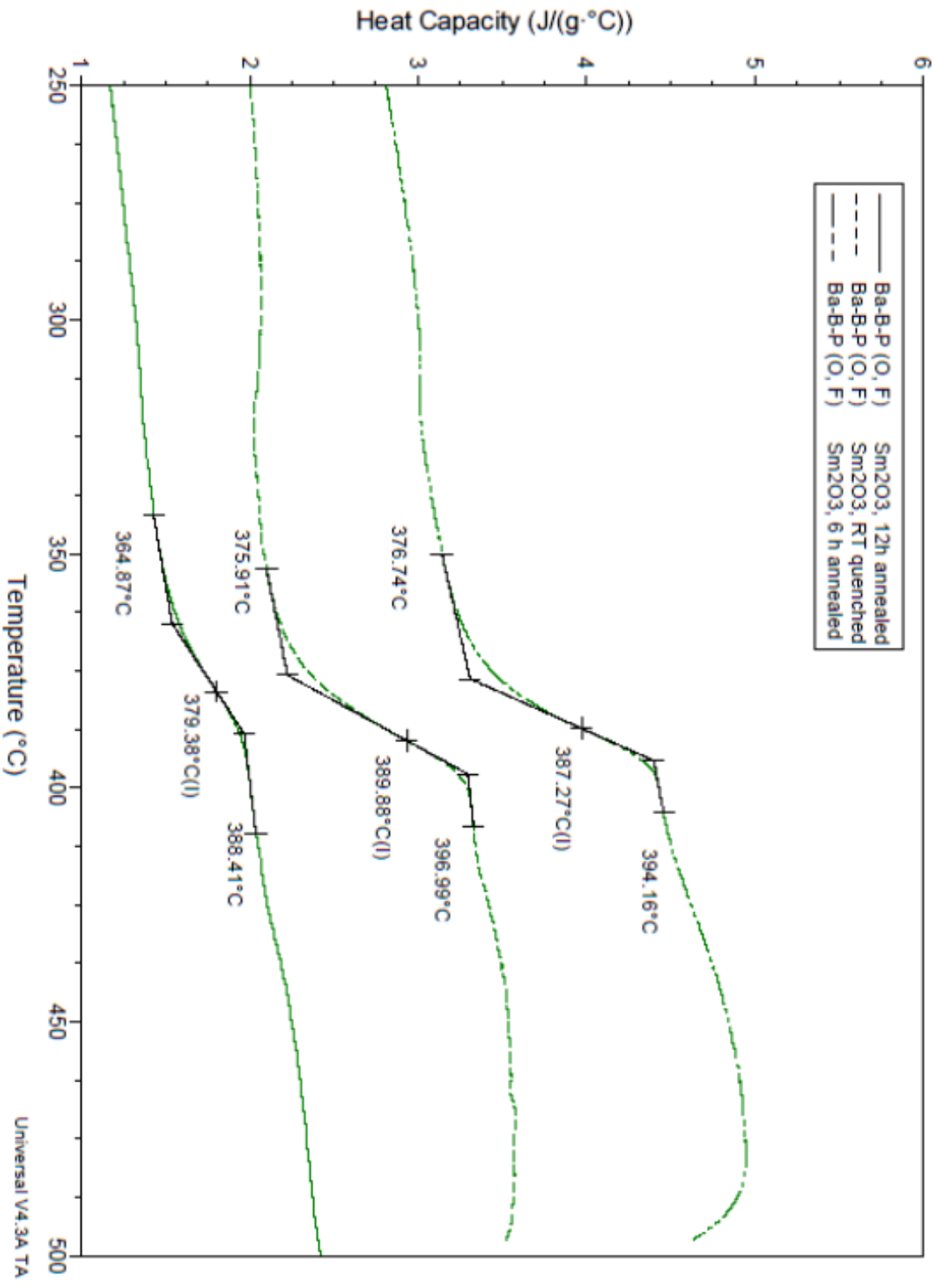

Figure 4.33 MDSC thermograms of BaF_2-B_2O_3-$Na_4P_2O_7$ doped with 0.33 wt% Sm_2O_3 materials. The solid, semi-solid, and dashed lines represent 12 h annealed, 6 h annealed and room temperature quenched samples, respectively.

5 SUMMARY AND CONCLUSIONS

The $BaBPO_5$, BaF_2-B_2O_3-$Na_4P_2O_7$, and SiO_2-Al_2O_3-B_2O_3-Na_2O-SnO_2 material systems were studied as suitable rare earth doped host materials for use in dosimetry of MRT. The rare earth compounds Sm_2O_3 and SmF_3 were used as dopants and $ErCl_3$ as a codopant for $BaBPO_5$. The rare earth ion Sm^{3+} was contributed to the host materials by dopant compounds. Select material samples were characterized with ESR, absorbance spectroscopy, Raman spectroscopy, XRD, DSC and MDSC. XL was observed for all samples, which means that these materials can function as scintillators. The presence of PL spectra depended on host material; only some material systems were capable of x-ray storage phosphor function. Below, the findings for each material system are described briefly. Concluding remarks and recommendations on future studies are made following the summary of findings.

5.1 $BaBPO_5$ Materials

The $BaBPO_5$ materials convert, as is evident from the Sm^{2+} peak increase during irradiation for XL and after irradiation for PL. PL intensity increases for the peak at 683 nm, indicating that the Sm^{2+} formed during x-ray irradiation (as is seen from the XL spectra) is at least metastable. $ErCl_3$ codoping improved modestly PL and XL intensities for irradiated samples. Codoping with erbium chloride also appeared to minimize the Sm^{2+} PL prior to irradiation, which may improve the dose sensitivity of the x-ray storage phosphor. With ESR, the paramagnetic defect structure of $BaBPO_5$ was shown to contain oxygen hole centres in the glass and crystalline phases. Raman spectroscopy determined tetrahedral borates and phosphates from $BaBPO_5$, but also extra peaks from possible thermal decomposition due to boron evaporative loss during synthesis. XRD analysis determined the unit cell and grain size of another $BaBPO_5$ sample. DSC studies showed $BaBPO_5$ materials contained thermodynamic transitions beyond 590 ºC. Glass transition temperatures at temperature greater than 590 ºC may be difficult to manufacture.

5.2 BaF_2-B_2O_3-$Na_4P_2O_7$ Materials

Sm_2O_3 doped BaF_2-B_2O_3-$Na_4P_2O_7$ materials exhibited optimal PL intensity at 683 nm either with room temperature quenching or by annealing a hot quenched sample for 12 hours at 600 ºC. SmF_3 doped BaF_2-B_2O_3-$Na_4P_2O_7$ materials had optimal PL for non-annealed samples and optimal XL for non-annealed glass samples. Absorbance spectroscopy of a BaF_2-B_2O_3-$Na_4P_2O_7$ material indicated colour centre absorbance as an absorbance peak developed with x-ray irradiation. These colour centres are likely oxygen hole centres. Raman Spectroscopy showed that peaks formed in the non-annealed samples after irradiation. Thus, there is a change in structure associated with x-ray irradiation. This change in structure is similar to the effects of annealing. Annealing the samples produced similar peaks to that of the irradiated non-annealed samples. Annealing for long periods of time (12 hours) at 600 ºC produces crystallinity as is evident from the sharp Raman spectral peaks. The irradiation effect may be causing a breaking of bonds between bridging oxygen, which produces non-bridging oxygen and altered molecular vibrations.

BaF_2-B_2O_3-$Na_4P_2O_7$ materials were assayed for glass transitions and crystallization onset temperatures. The stability of the BaF_2-B_2O_3-$Na_4P_2O_7$ materials was quantified with the Hruby coefficient. It was partially stable to form glass and samarium (III) oxide dopant improved this stability. The observation of some crystallinity on the samples corroborates with this level of glass forming stability. The glass transitions were near 400 ºC which would allow commercial processing and forming of BaF_2-B_2O_3-$Na_4P_2O_7$ materials.

5.3 SiO_2-Al_2O_3-B_2O_3-Na_2O-SnO_2 Materials

The SiO_2-Al_2O_3-B_2O_3-Na_2O-SnO_2 material was capable of XL according to the Sm^{2+} peak but did not show appreciable PL intensity. This silicate material would not likely be useful as an x-ray storage phosphor due to lack of change in PL intensity at 683 nm emission. The PL intensity remains almost the same, and the reduction of Sm ions from 3+ to 2+ did not persist for a sufficiently long duration for that ion state to be observed in larger intensities. XL spectra showed appreciable intensity at 683 nm emission, indicating that Sm^{2+} ions were temporary and

not stable. Thermal properties were beyond the limits of the 590 ºC temperature for aluminium and were not assayed.

5.4 Conclusion

Overall, the BaF_2-B_2O_3-$Na_4P_2O_7$ materials doped with Sm_2O_3 or SmF_3 appear to be the best candidate material for further research. $BaBPO_5$ host materials can also be useful; however, the sodium modifier in the BaF_2-B_2O_3-$Na_4P_2O_7$ materials improves thermal properties considerably. Both can be useful scintillators and x-ray storage phosphors. The silicate host material proved to only be suitable for scintillation, but it possesses very high temperature thermal properties which may preclude its adoption in a manufacturing process. Erbium chloride codoping slightly improved $BaBPO_5$ host material luminescence properties and it may be of use in other host materials too for improving samarium luminescence and therefore conversion read-out.

Dynamic range curves for XL and PL intensities would be an important next step in establishing BaF_2-B_2O_3-$Na_4P_2O_7$ materials for scintillation or x-ray storage phosphor functionality. Also, determining spatial resolution and spatial modulation transfer function would be of importance. The host material chemical structure favours more glass formation with samarium oxide dopant and is thus advisable to use it to dope. Sodium pyrophosphate could also be partially substituted with phosphate compound containing glass formers to improve glass stability during quenching. Also, substituting barium fluoride for barium oxide could improve the covalent glass network for further improvement of glass stability during quenching.

6 REFERENCES

[1] D. N. Slatkin, P. Spanne, F. A. Dilmanian and M. Sandborg, "Microbeam radiation therapy," *Med. Phys.,* vol. 19, no. 6, pp. 1395-1400, Nov/Dec 1992.

[2] H. Blattmann, J.-O. Gebbers, E. Brauer-Krisch, A. Bravin, G. Le Duc, W. Burkard, M. Di Michiel, V. Djonov, D. N. Slatkin, J. Stepanek and J. A. Laissue, "Applications of synchrotron X-rays to radiotherapy," *Nuclear Instruments and Methods in Physics Research A,* vol. 548, pp. 17-22, 2005.

[3] M. L. F. Lerch, M. Petasecca, A. Cullen, A. Hamad, H. Requardt, E. Brauer-Krisch, A. Bravin, V. L. Perevertaylo and A. B. Rosenfeld, "Dosimetry of intensive synchrotron microbeams," *Radiation Measurements,* vol. 46, pp. 1560-1565, 2011.

[4] E. A. Siegbahn, E. Brauer-Krisch, J. Stepanek, H. Blattmann, J. A. Laissue and A. Bravin, "Dosimetric studies of microbeam radiation therapy (MRT) with Monte Carlo simulations," *Nuclear Instruments and Methods in Physics Research A,* vol. 548, pp. 54-58, 2005.

[5] K. Richardson, D. Krol and K. Hirao, "Glasses for Photonic Applications," *International Journal of Applied Glass Science,* vol. 1, no. 1, pp. 74-86, 2010.

[6] A. C. Thompson, "X-ray Detectors," in *X-RAY DATA BOOKLET*, Berkeley, Lawrence Berkeley National Laboratory, 2009, pp. 4-32 to 4-39.

[7] R. M. Kadam, T. K. Seshagiri, V. Natarajan and S. V. Godbole, "Radiation induced defects in BaBPO5:Ce and their role in thermally stimulated luminescence reactions: EPR and TSL investigations," *Nuclear Instruments and Methods in Physics Research B,* vol. 266, pp. 5137-5143, 2008.

[8] M. Jensen, L. Zhang, R. Keding and Y. Yue, "Homogeneity of Inorganic Glasses: Quantification and Ranking," *International Journal of Applied Glass Science,* vol. 2, no. 2, pp. 137-143, 2011.

[9] M. F. Brown, Introduction to Thermal Analysis, Dordrecht: Kluwer Academic Publishers, 2001.

[10] A. S. Krasnikov and A. I. Berezhnoi, "Radiation-Excited Color Centers in Glass-Ceramic Materials," *Glass and Ceramics, translation from "Steklo i Keramica",* vol. 54, no. 9-10, pp. 330-331, 1997.

[11] W. G. Richards and P. R. Scott, Structure and Spectra of Atoms, London: John Wiley & Sons, Ltd., 1976.

[12] S. Kasap, C. Koughia, J. Singh, H. Ruda and S. K. O'Leary, "Optical Properties of Electronic Materials: Fundamentals and Characterization," in *Springer Handbook of Electronic and Photonic Materials*, New York, Springer Science+Business Media, Inc., 2006, pp. 47-78.

[13] D. C. Harris and M. D. Bertolucci, Symmetry and Spectroscopy: An Introduction to Vibrational and Electronic Spectroscopy, Mineola: Dover Publications, Inc., 1989.

[14] E. B. Wilson Jr, J. C. Decius and P. C. Cross, Molecular Vibrations: The Theory of Infrared and Raman Vibrational Spectra, Mineola: Dover Publications, Inc., 1980.

[15] A. Feltz, Amorphous Inorganic Materials and Glasses, Weinheim: VCH, 1993.

[16] E. M. Gullikson, "Mass Absorption Coefficients," in *X-Ray Data Booklet*, Berkeley, Lawrence Berkeley National Laboratory, 2009, pp. I-38 to I-43.

[17] L. D. Azaroff and J. J. Brophy, Electronic Processes in Materials, New York: McGraw-Hill Book Company, Inc., 1963.

[18] A. Guinier, X-Ray Diffraction in Crystals, Imperfect Crystals, and Amorphous Bodies, Mineola: Dover Publications, Inc., 1994.

[19] H. M. Rosenberg, The Solid State: an introduction to the physics of crystals for students of physics, materials science, and engineering, second edition, Oxford: Clarendon Press, 1978.

[20] J. W. Orton, Electron Paramagnetic Resonance: An Introduction to Transition Group Ions In Crystals, New York: Gordon and Breach, 1969.

[21] G. E. Pake, Paramagnetic Resonance: An Introductory Monograph, New York: W. A. Benjamin, Inc., 1962.

[22] A. A. Lacey, D. M. Price and M. Reading, "Theory and Practice of Modulated Temperature Differential Scanning Calorimetry," in *Modulated Temperature Differential Scanning Calorimetry: Theory and Practical Applications in Polymer Characterisation*, Dordrecht, Springer, 2006.

[23] S. O. Kasap and D. Tonchev, "Glass transformation in vitreous As2Se3 studied by conventional and temperature-modulated differential scanning calorimetry," *J. Mater. Res.,* vol. 16, no. 8, pp. 2399-2407, 2001.

[24] B. Wunderlich, Thermal Analysis, London: Academic Press, 1990.

[25] TA Instruments - Waters LLC, *DSC Getting Started Guide,* New Castle: TA Instruments - Waters LLC, 2001.

[26] D. Tonchev and S. O. Kasap, "Thermal Properties and Thermal Analysis: Fundamentals, Experimental Techniques and Applications," in *Springer Handbook of Electronic and Photonic Materials*, New York, Springer Science+Business Media, Inc., 2006, pp. 385-408.

[27] A. K. Varshneya, Fundamentals of Inorganic Glasses, Second Edition, Sheffield: The Society of Glass Technology, 2006.

[28] Z. U. Borisova, Glassy Semiconductors, New York: Plenum Press, 1981.

[29] Y. Huang, W. Zhao, L. Shi and J. H. Seo, "Structural defects and luminescence properties of Sm2+ ions doped in BaBPO5 phosphor by X-ray irradiation," *Journal of Alloys and Compounds,* vol. 477, pp. 936-940, 2009.

[30] N.-J. Kim, S.-H. Im, D.-H. Kim, D.-K. Yoon and B.-K. Ryu, "Structure and Properties of

Borophosphate Glasses," *Electronic Materials Letters,* vol. 6, no. 3, pp. 103-106, 2010.

[31] G. H. Dieke, "Energy Levels of and Energy Transfer in Rare Earth Salts," in *Paramagnetic Resonance: Proceedings of the First International Conference held in Jerusalem, July 16-20, 1962, Volume I*, New York, Academic Press Inc., 1963, pp. 237-252.

[32] H. Liang, Y. Tao, W. Chen, X. Ju, S. Wang and S. Qiang, "The luminescent properties of lanthanide ions activated BaBPO5 in VUV-Vis range," *Journal of Physics and Chemistry of Solids,* vol. 65, pp. 1071-1076, 2004.

[33] H. B. Liang, Q. Su, S. Lu, Y. Tao, T. D. Hu and T. Liu, "UV-VUV excited luminescence of SrBPO5:Sm phosphor prepared in air," *Materials Research Bulletin,* vol. 37, pp. 1981-1989, 2002.

[34] E. Malchukova, B. Boizot, D. Ghaleb and G. Petite, "Optical Properties of pristine and γ-irradiated Sm doped borosilicate glasses," *Nuclear Instruments and Methods in Physics Research A,* vol. 537, pp. 411-414, 2005.

[35] Physical Measurement Laboratory, "Fundamental Physical Constants --- Complete Listing," NIST, 2010. [Online]. Available: http://physics.nist.gov/cuu/Constants/Table/allascii.txt. [Accessed 26 May 2012].

[36] D. Tonchev, E. Muzar, G. Okada, I. Kostova, Z. Stoeva, G. Patronov, B. Morrell and S. O. Kasap, "Synthesis, Structure and Luminescent Properties of Samarium-Doped Borophosphates," *Journal of Chemical Technology and Metallurgy,* (submitted July 1, 2012 and accepted for publication).

[37] M. Nogami and K. Suzuki, "Formation of Sm2+ Ions and Spectral Hole Burning in X-ray Irradiated Glasses," *Journal of Physical Chemistry B,* vol. 106, pp. 5395-5399, 2002.

[38] I. I. Ezhik, S. I. Berul' and N. M. Kotelevskii, "Investigation of Luminescence and ESR spectra of Samarium and Neodymium in Sodium Metaphosphate," *English translation from Izvestiya Vysshikh Uchebykh Zavedenii, Fizika,* no. 12, pp. 125-127, 1970.

[39] P. Ebeling, D. Ehrt and M. Friedrich, "X-ray induced effects in phosphate glasses," *Optical Materials,* vol. 20, pp. 101-111, 2002.

[40] Y. Shi, J. Liang, H. Zhang, Q. Liu, X. Chen, J. Yang, W. Zhuang and G. Rao, "Crystal Structure and Thermal Decomposition Studies of Barium Borophosphate, BaBPO5," *Journal of Solid State Chemistry,* vol. 135, pp. 43-51, 1998.